Coupled Air-Sea-Land Interactions: Understanding the MJO Eastward Propagation and Maritime Continent Barrier Effect

Ajda Savarin

A dissertation
submitted in partial fulfillment of the
requirements for the degree of

Doctor of Philosophy

University of Washington

2022

Reading Committee:
Shuyi S. Chen, Chair
Dennis Hartmann
Daehyun Kim
Chidong Zhang

Program Authorized to Offer Degree:
Atmospheric Sciences

University of Washington

Abstract

Coupled Air-Sea-Land Interactions: Understanding the MJO Eastward Propagation and Maritime Continent Barrier Effect

Ajda Savarin

Chair of the Supervisory Committee:
Professor Shuyi S. Chen
Atmospheric Sciences

The Madden-Julian oscillation (MJO) is the leading mode of tropical intraseasonal variability affecting the global weather and climate. The MJO is characterized by large-scale organized convection and its associated circulation that develops over the tropical Indian Ocean (IO) and propagates into the West Pacific Ocean (WP) across the Maritime Continent (MC). The MJO has direct impacts on extreme rainfall and flooding over the MC, Southeast Asia and north Australia and tropical cyclones over the IO. The MJO's downstream influences include tropical cyclones, atmospheric rivers, heat waves, and episodes of drought and flooding. Though the MJO has been the subject of many observational and modeling studies, it remains a challenging phenomenon for both theoretical understanding and accurate prediction in global weather and climate models.

The overarching goal of this dissertation is to better understand the physical processes affecting the eastward propagation of the MJO from the IO to the WP and improve MJO modeling and prediction. In contrast to many existing MJO studies, we use a novel approach of identifying and tracking MJO events through their large-scale precipitation. Identifying individual MJO events as a physical phenomenon enables us to study the MJO and its interaction with the atmosphere, ocean, and land in its environment. We begin by using high-resolution coupled atmosphere-ocean model simulations and satellite- and field campaign

observations to study the physical processes that impact the MJO's eastward propagation over the IO (Chapters 2 and 3). We follow up by conducting coupled model sensitivity experiments to better understand the MC barrier effects on the MJO (Chapter 4). Finally, we use 20 years of satellite-derived precipitation observations to investigate the seasonal and interannual variability of the MJO eastward propagation and its zonal and meridional variability (Chapter 5). Our findings confirm that the eastward propagation of MJO convection/precipitation is affected by how it interacts with its local ocean and land environments, and is modulated by seasonal and interannual variability.

We identify some critical pathways that can help improve MJO modeling and prediction through a better representation of:

Chapter 2: The multi-scale convective structure of the MJO.

Chapter 3: Air-sea interaction of the MJO and its effect on the upper ocean.

Chapter 4: Air-sea-land interactions over the MC.

We find that:

- Cloud-permitting resolution is better able to represent the various scales on which precipitation occurs within the MJO (convective, mesoscale, and large-scale organization), and how convection interacts with the marine boundary layer.

- Strong surface winds and intense precipitation associated with the MJO induce sea surface temperature and upper ocean cooling. Reduced air-sea fluxes create an environment unfavorable for sustaining intense precipitation, contributing to the MJO's eastward propagation.

- Mesoscale convective systems (MCSs) forming over islands suppress convection over surrounding waters, over which the MJO prefers to propagate through the region. The

land-based MCSs grow larger and more intense when MC topography is flattened, which enhances the MC barrier effect.

We also show that on a broader scale, MJO convection/precipitation and eastward propagation are modulated by modes of seasonal and interannual variability (Chapter 5). The seasonal cycle significantly affects both the zonal and meridional structure of the MJO, including its initiation, termination, and eastward propagation. On longer time scales, climate variability associated with sea surface temperature patterns over the Indian and Pacific oceans (ENSO, Indian ocean dipole) can shift low-level zonal wind convergence regions toward or away from the MC. Low-level zonal wind convergence can provide background ascent that amplifies MJO activity, and can strongly affect the zonal variability of the MJO. Unlike the direct link between SST variability and the MJO, upper-tropospheric zonal wind variability associated with the QBO shows a strong seasonal dependence and generally much weaker control over MJO propagation. The strength of the MC barrier on MJO propagation also shows seasonal and interannual variability and is linked to a combination of the background state and the location of MJO convection. The MC barrier effect is weakest during the peak monsoon seasons (Dec-Mar and June-Aug) and during La Niña months, and it is strongest during the monsoon transition seasons (Apr-Jun and Sep-Nov) and ENSO-neutral conditions.

TABLE OF CONTENTS

LIST OF FIGURES

LIST OF TABLES

ACKNOWLEDGMENTS

First and foremost, I would like to thank my advisor, Shuyi Chen, for her support, guidance, and friendship throughout my graduate school journey and helping me become the scientist I am today. I would like to thank my committee members, Dennis Hartmann, Daehyun Kim, Mike McPhaden, Janet Sprintall, Mike Wallace, and Chidong Zhang for their thoughtful suggestions that improved the quality of my work. The work presented in this dissertation was directly supported by the NASA NESSF fellowship and funding from NOAA.

I would like to acknowledge past and present members of my research group at University of Miami and University of Washington. Discussions related to our research projects expanded my horizons and helped me grow and develop communication skills that I greatly cherish. Specifically, I would like to thank Milan Curcic for teaching me about coupled modeling, Brandon Kerns for allowing me to bounce off research ideas, and Yakelyn Jauregui, Edoardo Mazza, and Benjamin Barr for creating the best research family one could find. The hours we spent in weekly research group meetings were long, but the friendships we built along the way will last forever.

I would like to thank Greg Hakim and Cliff Mass, for whom I served as a co-instructor for undergraduate classes, for helping me learn how to teach. Additionally, I would like to thank the support staff in the UW Department of Atmospheric Sciences department, Erica Coleman, Jennifer Siembor, David Warren, and Hettie Scofield for making everything run smoothly.

I would like to thank my family for their encouragement to pursue my education, even though it took me far from home and I'm pretty sure they have no idea what it is that I do. And finally, I would like to thank my fiancé, Philippe Papin, for cheering me up when I was feeling down, providing support and company during COVID, and patiently walking beside me on my journey.

Chapter 1
INTRODUCTION

The Madden-Julian Oscillation (MJO) consists of eastward-propagating large-scale precipitation and associated atmospheric circulation that forms over the warm waters of the tropical Indian Ocean (IO) and western Pacific. It was first described as a vertically coherent tropospheric oscillation in pressure, temperature, and zonal wind in the central tropical Pacific Ocean (Madden and Julian, 1971), and it was speculated that the observed variability is associated with a large circulation cell oriented in a zonal plane near the equator. By the following year, Madden and Julian (1972) expanded their analysis to include observing stations over the global tropics, deduced that the phenomenon occurs on a global scale with a period of 40-50 days, and they described the oscillation. The MJO pattern consists of convection initiating and growing over the tropical IO, propagating eastward across the Indonesian Maritime Continent (MC) and dissipating over the central Pacific. The large-scale convection, which can measure thousands of kilometers across, is accompanied by low-level zonal wind convergence, upper-level divergence, and a widespread reduction in surface pressure (Fig. 16 of Madden and Julian, 1972).

Many observational studies using satellite and field campaign data have shown that the MJO has an average zonal phase speed of 5 m s^{-1}, with an area deduced from cloud cover anomalies of 12000-20000 km and varies on an intraseasonal time scale from 30 to 90 days (Zhang, 2005). MJO-associated convection is a multi-scale phenomenon (Chen et al., 1996; Nakazawa, 1988). The large-scale convective envelope consists of a multitude of westward propagating smaller- and meso-scale convective systems, that tend to develop to the east of the previous ones, resulting in an overall eastward propagation of the MJO (Hendon and Liebmann, 1994). While the precipitation associated with the MJO tends to be tied to

the warm waters of the tropical IO and western Pacific, its upper-level wind signature can circumnavigate the globe.

The essential MJO characteristics identified by Madden and Julian (1972) include the MJO's eastward propagation, its planetary spatial scale, and its intraseasonal time scale. In a recent review article, Zhang et al. (2020) present a list of additional characteristics and observed features that are important for the further understanding of the MJO. They listed six factors including the MJO's three-dimensional structure, seasonal cycle, irregularity, multi-scale structure, modulation by lower-frequency phenomena, and its interaction with the underlying ocean.

Identifying the MJO as a physical entity of large-scale precipitation and associated circulation has been difficult. Most techniques for MJO identification depend on global anomaly fields (e.g., the Real-time Multivariate MJO index, RMM; Wheeler and Hendon, 2004), or intraseasonal filtering (Wheeler and Kiladis, 1999; Zhang and Ling, 2017, e.g., lag-regression, wavenumber-frequency filtering, convection-center tracing). The development of such indices has allowed for identification of the MJO's influences and teleconnections, which extend through the tropics and into the midlatitudes, as hypothesized by Madden and Julian (1972).

In addition to local precipitation over the tropical warm pool and flooding events over the MC, traditional MJO indices have been used to document the effects of the MJO on tropical weather and climate phenomena like the south-east Asian monsoon (Taraphdar et al., 2018), tropical cyclones (Maloney and Hartmann, 2000a,b; Zhao and Li, 2018), and even El Niño-Southern Oscillation (ENSO; McPhaden et al., 2006). Outside of the tropics, the MJO has shown strong connections with atmospheric rivers (Zhou et al., 2021b), surface air temperatures (Vecchi and Bond, 2004), fires, flooding, tornadoes, and extreme precipitation events (Zhang, 2013).

The MJO's global impacts derive from the heating associated with the propagating large-scale precipitation. But the exact location and structure of the heating might not be best defined using traditional MJO indices such as the RMM, because those indices represent

the MJO in terms of statistical patterns and anomalies which are not directly related to precipitation. To overcome the limitations of traditional MJO indices, this study uses a large-scale precipitation tracking algorithm (LPT; Kerns and Chen, 2016, 2020) to identify MJO events based on tracking of large areas of eastward propagating precipitation features. It tracks three-day accumulated precipitation without using intraseasonal filtering or departures from long-term mean climate conditions and can be used on any regional or global datasets that have sufficient spatial coverage. The tracking algorithm delimits the boundaries of MJO-associated precipitation from its environment at any given time and provides information on the spatial and temporal evolution of each individual MJO event, as well as the variability from one MJO event to another.

Though the MJO is associated with wide-ranging impacts on global weather and climate, modeling individual events or statistical quantities associated with the MJO remains a challenge. In large climate model intercomparison projects (CMIP), the MJO prediction skill has been increasing from one generation to the next. In CMIP5, one third of the models produce a peak of MJO precipitation between 30 and 70 days, but the propagation is too slow, and MJO cycles persist for too long compared to observations - and only one model out of 20 produces a realistic eastward propagation (Hung et al., 2013). In CMIP6, the eastward propagation of the MJO is more realistic (Le et al., 2021; Li et al., 2022), but the magnitude of the MJO is still underestimated, and it represents a smaller portion of intraseasonal variability than observed. In addition to improvements in general representation of MJO propagation, CMIP6 models also show improvements in the propagation across the MC, with 59% of models showing values close to observations (Ahn et al., 2020).

MJO prediction skill in climate models is sensitive to multiple factors, such as atmosphere-ocean coupling (Zhang et al., 2006; DeMott et al., 2015), the representation of the background state (Waliser et al., 2003; Ahn et al., 2020), and the model physics - especially the convective parameterization (Hung et al., 2013; Zhu et al., 2020). But even with these improvements, most CMIP6 models still underestimate the frequency of MJO initiation over the IO and its amplitude, as well as as the barrier effect of the MC on MJO propagation (Chen et al., 2022).

Though advances in understanding the MJO have led to improvements in its prediction, there seems to be a disconnect between the MJO as an observed physical phenomenon and studies that focus on identifying the MJO through the anomalies it produces.

This study aims to improve our understanding of the physical processes that affect the eastward propagation of the MJO from the Indian Ocean to the Pacific across the Maritime Continent. Rather than treating the MJO as a statistical anomaly (e.g., as when identified using the RMM index), we study the MJO as a physical phenomenon through its precipitation and associated circulation as described by Madden and Julian (1972). We use a combination of satellite and field campaign observations as well as a regional high-resolution atmosphere-ocean model.

Science Questions and Hypotheses

This research is motivated by a series of questions:

Q1. How are MJO's initiation and eastward propagation affected by the representation of multi-scale convective systems?

Q2. How is MJO's eastward propagation affected by atmosphere-ocean coupling?

Q3. How is MJO's eastward propagation affected by the islands of the MC?

Q4. What are the modes of variability of the MJO's eastward propagation across the MC?

We hypothesize that atmosphere-ocean-land interactions play an important role in the prediction of MJO precipitation and its eastward propagation.

Chapter 2 addresses Q1 by analyzing observations and model simulations of the MJO performed at a grid spacing of 12 km (with a convective parameterization) versus a grid spacing of 4 km (without a convective parameterization). In addition to comparing models with different resolution, the performance of two different convective parameterizations is evaluated. We find that a higher resolution model can better represent the multi-scale

convective systems associated with the MJO, and that shallow cumulus mixing across the top of the boundary layer is important for the MJO's eastward propagation.

Chapter 3 addresses Q2 by analyzing observations and model simulations of the MJO performed at a grid spacing of 4 km and with different degrees of atmosphere-ocean coupling. We compare an atmosphere-only simulation with constant sea-surface temperatures versus atmosphere-ocean coupled simulations with slight differences in air-sea flux parameterizations. We find that the strong winds associated with the MJO cool the upper ocean, which reduces the evaporation and creates an environment unfavorable for continued convection, so the MJO propagates eastward. When the upper-ocean cooling is not represented, strong winds blowing over constantly warm waters provide a continuous moisture source and the MJO does not propagate away from the IO.

Chapter 4 addresses Q3 and the role that land plays in the MJO's eastward propagation. Atmosphere-ocean coupled model simulations of the MJO at a grid spacing of 4 km with a variety of terrain configurations over the MC are compared: real topography (with mountains and land-sea contrast) versus flattened terrain (with land-sea contrast but no mountains) versus removed islands (no mountains or land-sea contrast). We find that in the absence of land, the MJO propagates across the MC smoothly and without weakening, but when land is present (with or without mountains), its propagation is disrupted. When topography is flattened, diurnal convective systems over land can merge and grow into longer-lasting mesoscale convective systems that develop their own circulations and compete with the MJO.

Chapter 5 contains our current ongoing work, in which we address Q4 by analyzing 20 years of MJO events tracked in satellite-derived precipitation observations using the large-scale precipitation tracking algorithm. We describe patterns of seasonal and interannual variability of MJO propagation across the MC, and the variability in the MC barrier effect.

Chapter 2

EFFECTS OF MODEL RESOLUTION AND MOIST PHYSICS ON ATMOSPHERIC BOUNDARY LAYER AND MJO PRECIPITATION

Savarin, A., & Chen, S. S. (2022). Pathways Pathways to Better Prediction of the MJO: 1. Effects of Model Resolution and Moist Physics on Atmospheric Boundary Layer and Precipitation. Journal of Advances in Modeling Earth Systems, 14, e2021MS002928. https://doi.org/10.1029/2021MS002928.

2.1 Abstract

Despite recent advancements in numerical models, prediction of the Madden-Julian Oscillation (MJO) remains a major challenge in numerical weather prediction and climate modeling. This study explores pathways for improving MJO prediction through systematic investigation of the effects of model resolution and moist physics on simulations of the MJO in Part I, followed by effects of atmosphere-ocean coupling in Part II. The Unified Wave Interface – Coupled Model (UWIN-CM) experiments with different cumulus parameterizations (CP) and explicit microphysics with convection-permitting resolution are used to study the MJO convective initiation and eastward propagation. Observations of the atmosphere and ocean from the Dynamics of the MJO (DYNAMO) field campaign in 2011 are used to evaluate coupled model simulations. At lower resolution (12 km), the simulation with the Tiedtke CP produced an eastward propagating MJO event, while the simulation with the Kain-Fritsch CP did not. The main difference between the two low-resolution simulations is in the vertical structure of the atmospheric boundary layer which impacts the large-scale MJO circulation and precipitation. The Kain-Fritsch CP produced a persistent cloudy boundary layer that decoupled the tropospheric circulation from the surface and failed to produce the MJO. At higher resolution (4 km), convection-permitting simulations are robust in capturing the observed eastward propagation of MJO precipitation and surface westerly winds. Increasing resolution improves the boundary layer structure and convective systems, which results in more realistic vertical structure of wind and moisture throughout the troposphere, as well as an improved eastward propagation of the MJO.

2.2 Introduction

The Madden-Julian Oscillation (MJO) is the leading source of tropical intraseasonal variability with a wide range of impacts on global weather and climate (Zhang, 2013). The MJO is characterized by an alternating large-scale pattern of active and suppressed precipitation with corresponding enhanced westerly and easterly zonal winds (Madden and Julian, 1971, 1972). Active convection associated with the MJO typically initiates over the Indian Ocean (IO), propagates eastward over the Maritime Continent (MC) and into the western Pacific before decaying. Within the large-scale MJO convective envelope, deep convection is predominately organized in mesoscale convective systems or cloud clusters (Chen et al., 1996; Takayabu, 1994; Zhang, 2005). The mesoscale convective systems can enhance surface westerly winds through the downward transport of momentum into the atmospheric boundary layer (ABL; Robert A. Houze et al., 2000; Mechem et al., 2006). The surface westerly winds associated with the MJO affect air-sea fluxes of heat, moisture, and momentum, sea-surface temperature, and upper-ocean mixing, which can feed back to affect the atmospheric circulation and precipitation of the MJO (e.g., de Szoeke et al., 2015; DeMott et al., 2015).

The MJO convective initiation and eastward propagation over the IO remain a challenge for numerical weather prediction (NWP) and climate models. Many studies have assessed the skill of global climate models (GCMs) in producing coherent MJO events, with most agreeing that the amplitude of tropical intraseasonal variability is lower than observed. The majority of GCMs depict a stationary intraseasonal variability pattern concentrated over the IO, while only a few GCMs are capable of producing realistic MJO eastward propagation (Hung et al., 2013; Lin et al., 2006; Slingo et al., 1996). This results in a struggle to represent the MJO's downstream influences, which become stronger after the MJO has propagated over the MC (Adames and Wallace, 2014). At climate-model resolutions, the simulation of the MJO is strongly dependent on the choice of cumulus parameterization (CP), which attempts to represent the statistical effects of cumulus convection (e.g., Hung et al., 2013; Pilon et al., 2016) and atmosphere-ocean coupling (Zhang et al., 2006). Increasing the horizontal resolution in

GCMs does not greatly alter the representation of the MJO (Holloway et al., 2013; Jia et al., 2008; Pilon et al., 2016), unless it is also accompanied by a transition from parameterized to explicitly resolved convection (e.g., Benedict and Randall, 2009; Holloway et al., 2012, 2013; Zhu et al., 2009).

The MJO forecast predictive skills in current NWP models vary with lead time (Kerns and Chen, 2014; Nasuno, 2013), model physics and resolution, atmosphere-ocean coupling, and other factors (e.g., Barton et al., 2021; Shinoda et al., 2021). Model forecast of the MJO is sensitive to various CP schemes used in models (e.g., Jia et al., 2010), while studies using convection-permitting global models have shown that simulations with explicit moist physics can capture the eastward propagation of the MJO (e.g., Miura et al., 2007). An important mechanism associated with the MJO's eastward propagation is the convergence in the ABL ahead (to the east) of MJO precipitation (e.g., Hendon and Salby, 1994; Madden and Julian, 1972; Maloney and Hartmann, 1998). The convergence ahead of MJO precipitation moistens the atmosphere ahead of the MJO through shallow convection, creating an environment favorable for large-scale convection (Maloney and Hartmann, 1998). The successful simulation of the MJO in global models often depends on the representation of heating and moistening released into the free troposphere through shallow mixing (Pilon et al., 2016; Yang and Wang, 2019). The physical processes associated with air-sea interaction, the atmospheric boundary layer, and moist physics have not been thoroughly evaluated in models until recently due to the lack of coupled atmosphere-ocean observations of the MJO.

In this study, we investigate the effects of varying model resolution and moist physics on simulations of the MJO using a convection-permitting, coupled atmosphere-ocean model. The modeled MJO is the best-observed MJO event to date – the November-December 2011 case that occurred during the Dynamics of the MJO (DYNAMO) field campaign (Chen et al., 2016; Yoneyama et al., 2013). Coupled model experiments are systematically evaluated against satellite, airborne, and surface-based observations from DYNAMO. Extensive comparisons with in-situ observations provide insights on the importance of the interactions between convective parameterization, shallow convection, and the atmospheric boundary

layer for improving the representation of the MJO in models. In Section 2.3, we describe the coupled model used in this study, the coupled model experiments, the MJO tracking algorithm, and the observations used for model evaluations. The sensitivity of the MJO in model simulations to model resolution and moist physics is shown in Section 2.4, and is discussed in terms of large-scale convective organization, circulation, and eastward propagation. Section 2.5 focuses on key physical processes of atmospheric convection and boundary layer structure that affect the model's ability to produce surface westerly winds and large-scale circulation associated with the MJO. Summary and conclusions are presented in Section 2.6.

2.3 Methodology

2.3.1 Coupled Atmosphere-Ocean Model

The numerical model used in this study is the Unified Wave Interface–Coupled Model (UWIN-CM; Chen et al., 2013; Chen and Curcic, 2016), which allows for interactive coupling between atmosphere and ocean circulation models. The surface wave model in UWIN-CM is not used in this study.

The atmosphere component of UWIN-CM is the Weather Research and Forecasting (WRF) model v3.6.1 with the Advanced Research WRF (ARW) dynamical core (Skamarock et al., 2008). WRF is a non-hydrostatic atmospheric model that we configure with 44 terrain-following levels in the vertical, and three nested model grids shown Fig. 2.1. The outermost domain (D01) ranges from 15.4 to 174.6°E in longitude, and from 32.0°S to 32.0°N in latitude, with a grid spacing of 36 km. Two inner nests are centered on the equator, covering the areas from 36.0 to 165.2°E and 15.3°S to 15.3°N at a grid spacing of 12 km (D02), and from 54.0 to 154.6°E and 10.6°S to 10.6°N at a grid spacing of 4 km (D03). The highest-resolution domain is convection permitting, with explicit moist physics and no CP, while D01 and D02 use CP. The surface layer parameterization is based on the Monin-Obukhov similarity theory. The atmospheric boundary layer parameterization is the Yonsei University scheme (YSU; Hong et al., 2006). The cloud microphysics parameterization used in

all three domains is the single-moment five-species scheme in WRF (WSM5; Hong et al., 2004). Initial and boundary conditions of UWIN-CM come from the European Centre for Medium-Range Weather Forecast (ECMWF) operational forecast fields (from CR37R2) as described in Kerns and Chen (2014), with boundary conditions updated every 12 hours.

The ocean component of UWIN-CM is the HYbrid Coordinate Ocean Model (HYCOM) v2.2.99 (Metzger et al., 2014). HYCOM is a hydrostatic ocean circulation model with a vertical coordinate system that transitions between layers of constant density in deep water, layers of constant thickness (z-levels) in shallow water and near the ocean surface, and terrain-following layers in intermediate waters. HYCOM is configured with a single domain with uniform grid spacing of 0.08°, ranging from 9.8 km at the equator to 7.7 km at the domain's northern and southern boundaries, and spans from 30.0 to 172.0°E and from 33.0°S to 33.0°N. Out of 41 vertical layers, 14 are z-layers, 5 of which are located within 15 m of the surface (centered at depths of 0.5, 1.88, 4.33, 8.16, and 12.79 m). Initial and boundary conditions come from daily mean fields of the global HYCOM analysis (Cummings, 2005; Cummings and Smedstad, 2013).

2.3.2 Coupled Model Simulations

Four simulations were designed to address the effects of model resolution and atmospheric moist physics on the simulation of the second MJO event during the DYNAMO field campaign. All simulations include interactive atmosphere-ocean coupling (atmosphere-ocean simulations, abbreviated as AO in experiment names). As part of the naming convention, the number following AO in the experiment name refers to the grid spacing of the highest-resolution domain used in the experiment. CP is always used for the two lower-resolution domains (D01 and D02, 36- and 12-km grid spacing), with simulations varying between two options – Kain-Fritsch (KF; Kain and Fritsch, 1990; Kain, 2004), and Tiedtke (TK; Tiedtke, 1989; Zhang et al., 2011). In high-resolution experiments, we include D03 with convection-permitting grid spacing of 4 km, where CP is turned off, and precipitation is generated solely by the microphysical parameterization (WSM5). The main features of the simulations are

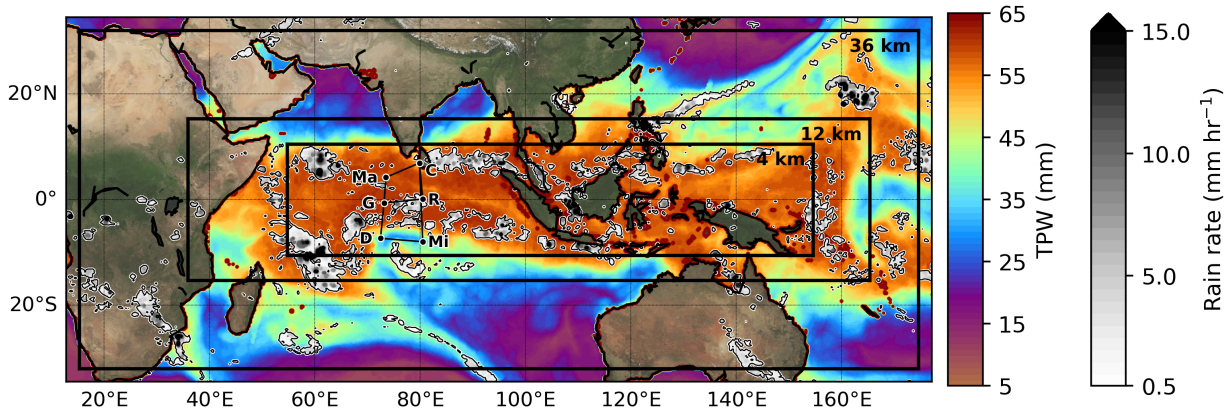

Figure 2.1: UWIN-CM configuration of HYCOM and WRF nested domains at 36-, 12-, and 4-km grid spacing. Color shading shows the total precipitable water (TPW, mm), grey shading indicates TRMM precipitation (mm hr^{-1}) at model initialization time, 22 November 2011 at 00 UTC. Circle markers show locations of the DYNAMO sounding sites in the central IO.

summarized in Table 2.1. All simulations are initialized at 00 UTC on 22 November 2011, which coincides with a time when convection associated with the MJO event was beginning to organize over the equatorial IO (Fig. 2.1). The simulations are integrated in time for 15 days (360 hours), at the end of which the observed MJO convection is in the eastern MC and is being steered northward, away from the equator.

Both KF and TK CPs are mass-flux type parameterizations and have been formulated to represent effects of deep and shallow convection but rely on different trigger and closure criteria. Some main differences include 1) the representation of convective momentum transport that is treated explicitly in TK, not in KF, 2) mixing by shallow convection, i.e., TK includes stronger entrainment for shallow convection than for deep convection, 3) type of convective closure that is based on convective available potential energy – CAPE in KF, whereas TK is based on moisture convergence, and 4) convective triggering functions. More detail on the differences between convective parameterizations is summarized in Suhas and Zhang (2014), and the details of each scheme are described in their respective publications

UWIN-CM Simulations

Simulation	Grid spacing in nested domains	Moist Physics
AO12-KF	36-, 12-km	Kain-Fritsch CP
AO12-TK	36-, 12-km	Tiedtke CP
AO4-kf	36-, 12-, 4-km	Kain-Fritsch CP*, WSM5 only
AO4-tk	36-, 12-, 4-km	Tiedtke CP*, WSM5 only

Table 2.1: Cumulus parameterization is always applied in the outer (36- and 12-km resolution) domains. In AO4 simulations, the inner (4-km resolution) domain uses the explicit WSM5 microphysics without CP.

(Kain and Fritsch, 1990; Kain, 2004; Tiedtke, 1989; Zhang et al., 2011).

2.3.3 MJO Tracking

Traditional MJO indices, such as the Real-time Multivariate MJO index (RMM; Wheeler and Hendon, 2004), require global coverage and long records in time to separate MJO variability from the base state. They cannot easily be used in regional models which are run at high resolution and over short periods of time, which is the case for our simulations. Instead, the Large-scale Precipitation Tracking (LPT) algorithm is used to track the precipitation envelope associated with the MJO (Kerns and Chen, 2016, 2020). The algorithm tracks a spatially smoothed 3-day rainfall accumulation that exceeds a chosen threshold over an area larger than 3x105 km^2. In Kerns and Chen (2016), the rainfall accumulation threshold of 12 mm day^{-1} was found to accurately capture MJO events during DYNAMO. In this study, a threshold of 15 mm day^{-1} is used instead, as model simulations tend to over-produce precipitation when compared to satellite-derived precipitation products. After precipitation is tracked, additional constraints are introduced to separate MJO precipitation from other systems. These constraints ensure that the LPT-tracked feature persists for at least seven days and exhibits consistent eastward propagation. Using LPT to track MJO precipitation provides a major advantage over traditional MJO indices – in addition to its applicability to

limited-domain, short-term model simulations, it also allows us to visualize the spatial and temporal evolution of MJO precipitation.

2.3.4 Observational Data

The simulated MJO event occurred during the intense observing period of DYNAMO, while many observational platforms were operating simultaneously. The high-frequency and resolution of observations collected during DYNAMO provide us with a unique opportunity to evaluate the model from different perspectives – including soundings, aircraft-released dropsondes, as well satellite data to provide large-scale context.

The data used in this study include:

- In-situ observations:
  - GPS dropsondes from the NOAA P3 aircraft (Chen et al., 2016);
  - Surface-based radiosonde soundings (3-hourly, 22 November – 7 December at Gan and 22 November – 1 December at R/V Revelle) (Ciesielski et al., 2014).
- Satellite-derived products:
  - precipitation - Tropical Rainfall Measuring Mission (TRMM) 3B42 v7, available 3-hourly at 0.25° resolution (Huffman et al., 2007) and the Global Precipitation Measurement (GPM) Integrated Multi-satellitE Retrievals for GPM (IMERG) v6B, available half-hourly at 0.1° resolution (Huffman et al., 2019);
  - surface winds - Cross-Calibrated Multi-Platform (CCMP) wind vector analysis v2, available 6-hourly at 0.25° resolution (Atlas et al., 2011);
  - total precipitable water - Morphed Integrated Microwave Imagery at CIMSS – Total Precipitable Water (MIMIC-TPW), available hourly at 0.25° resolution (Wimmers and Velden, 2011).
- Model initial and boundary conditions:

- ECMWF operational analysis for the atmosphere (0.25° resolution, updated 12-hourly);
- daily mean HYCOM global analysis (0.08° resolution, updated daily)

2.4 MJO Precipitation and Surface Winds

2.4.1 Large-Scale Structure and Eastward Propagation

The large-scale characteristics of the MJO convection and circulation in the model simulations and observation are first examined in the traditional time-longitude diagrams. Fig. 2.2 shows Hovmöller diagrams of rainfall rate (left) and surface zonal wind (right), averaged between 5°S and 5°N. TRMM 3B42 (from here on TRMM) precipitation and CCMP surface zonal winds are shown in the top row. The maximum terrain elevation inside the averaging region is shown on the bottom panels. The transition between the IO and MC occurs near 97°E and is marked with a black vertical line in all panels. The eastward propagation of MJO precipitation occurs in two distinct bursts associated with two convectively coupled Kelvin waves - they are part of the same MJO convective envelope but are separated by local suppression near the equator. The leading edge of precipitation is accompanied by zonal surface wind convergence to its east, with westerly winds extending across the IO to the west, and easterly winds to the east. Westerly winds over the equatorial IO persist after the active MJO convection has propagated over the MC, while precipitation over the IO is strongly suppressed.

The observed precipitation and surface-zonal-wind pattern is reproduced in three out of four UWIN-CM simulations (AO12-TK, AO4-kf and AO4-tk), while AO12-KF shows marked differences. In AO12-KF, there is no coherent eastward propagation of precipitation; instead, several westward-propagating tropical cyclones are formed over the IO (precipitation maxima over the IO in Fig. 2.2c). In contrast, a coherent eastward-propagating signal can be seen in both precipitation and surface westerly winds in AO12-TK. With increased resolution in AO4 simulations, the MJO pattern is robust regardless of the CP imposed outside

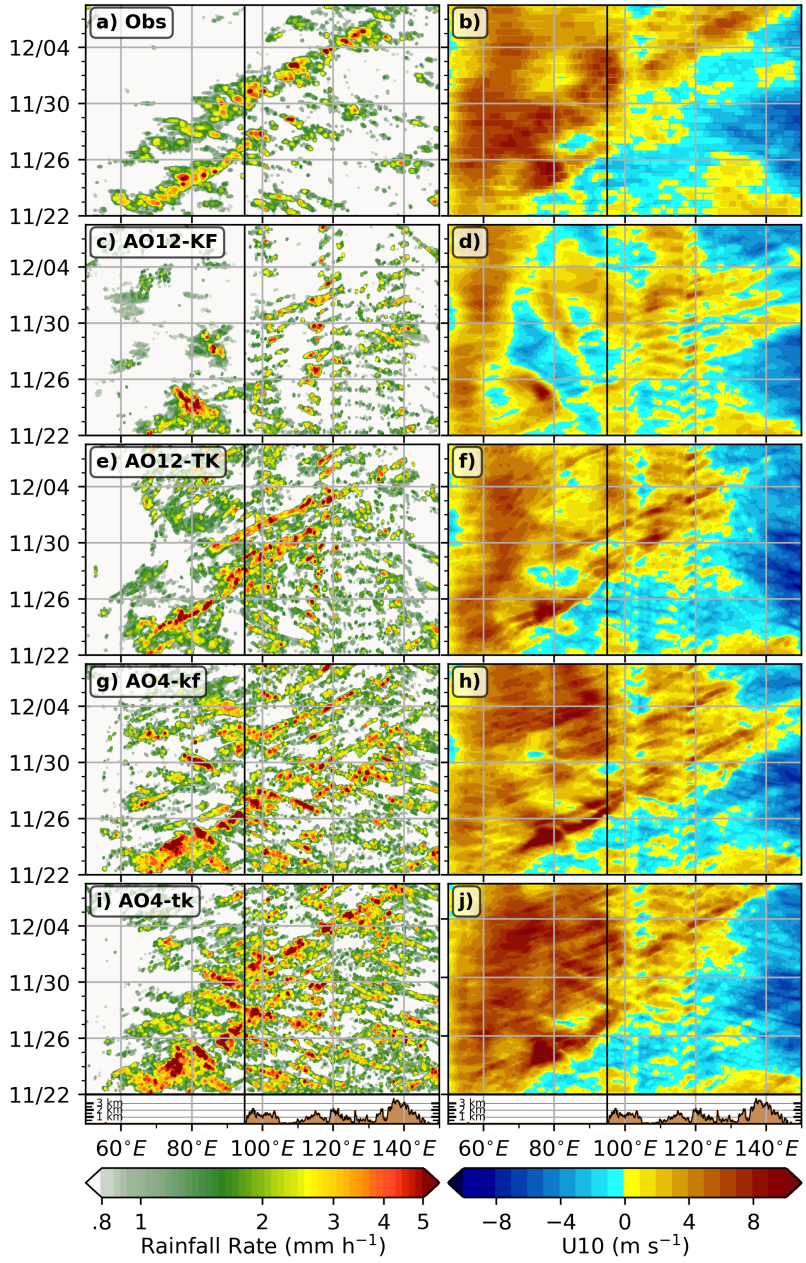

Figure 2.2: Hovmöller diagrams of 5°S-5°N averaged rainfall rate (left) and surface zonal winds (right) in observations (a, b) and model simulations as follows: AO12-KF (c, d), AO12-TK (e, f), AO4-kf (g, h), and AO4-tk (i, j). Brown shading on bottom panels shows the height of maximum topography in the averaging region, separating the longitudes of the IO from those of the MC (black vertical line at 97°E).

the high-resolution domain, and the amount of precipitation is increased. The consistency of AO4 simulations indicates that at convection-permitting resolution, the information coming through the boundaries (which is different due to different CPs in the lower resolution domains) has little effect on the large-scale MJO appearance, when compared to differences between AO12 simulations. Of the three model simulations that reproduce the MJO pattern, AO4-tk best matches the observed patterns and produces the strongest westerly winds and the greatest amount of precipitation.

The MJO in simulations using the Tiedtke CP (AO12-TK, AO4-tk) most closely match the eastward propagation of the observed MJO, while AO4-kf MJO propagates far ahead of the observed event. AO12-KF does not produce an MJO event, as the LPT envelope propagates westward (following a tropical cyclone) and is not sustained for seven days, violating both MJO criteria imposed on the tracking algorithm. This can be seen in Figs. 2.3 and 2.4, which show the evolution of large-scale precipitation in time and LPT tracking statistics, respectively. In Fig. 2.3, contours outline the LPT area, with color representing time. LPT tracking is available for model simulations after 25 November (a three-day accumulation is required), and the grey contours in Fig. 2.3 show the observed LPT before that time. The black rectangle in Fig. 2.3 spans the area from 55-90°E and 10°S-10°N and outlines the IO-averaging region that is used for further analysis of precipitation.

While MJO characteristics in AO12-TK closely match those of the observed event in terms of position, propagation speed, and precipitation amounts, the simulated MJO dissipates over the western MC two days before the end of the simulation (Fig. 2.4). AO4-simulated MJOs persist longer and propagate farther east, but accumulate larger errors in MJO position, area, and accumulated precipitation. AO4-tk track is close to the observed event but includes some large jumps in longitude over the MC (Fig. 2.4a, c). This simulation is also concurrent with the largest biases in MJO area and accumulated precipitation (Fig. 2.4b). The area and precipitation biases are smaller in AO4-kf, but the MJO location is misrepresented, and the eastward propagation after 28 November is too rapid and becomes decoupled from surface westerly winds (Fig. 2.6).

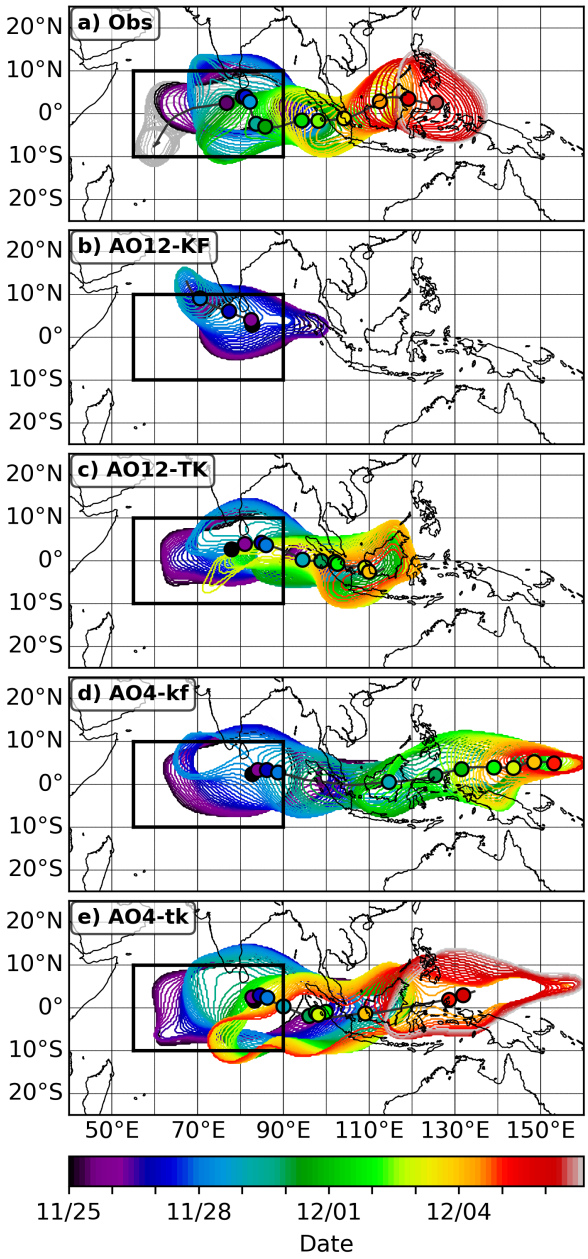

r

Figure 2.3: LPT evolution of precipitation in a) TRMM observations; b) AO12-KF; c) AO12-TK; d) AO4-kf; e) AO4-tk. Contours outline the area over which the mean 3-day precipitation exceeds 15 mm day^{-1}, with color corresponding to time. Colored circles indicate the LPT centroid in 24-hour intervals. The black square outlines the equatorial IO region (55-90°E, 10°S-10°N).

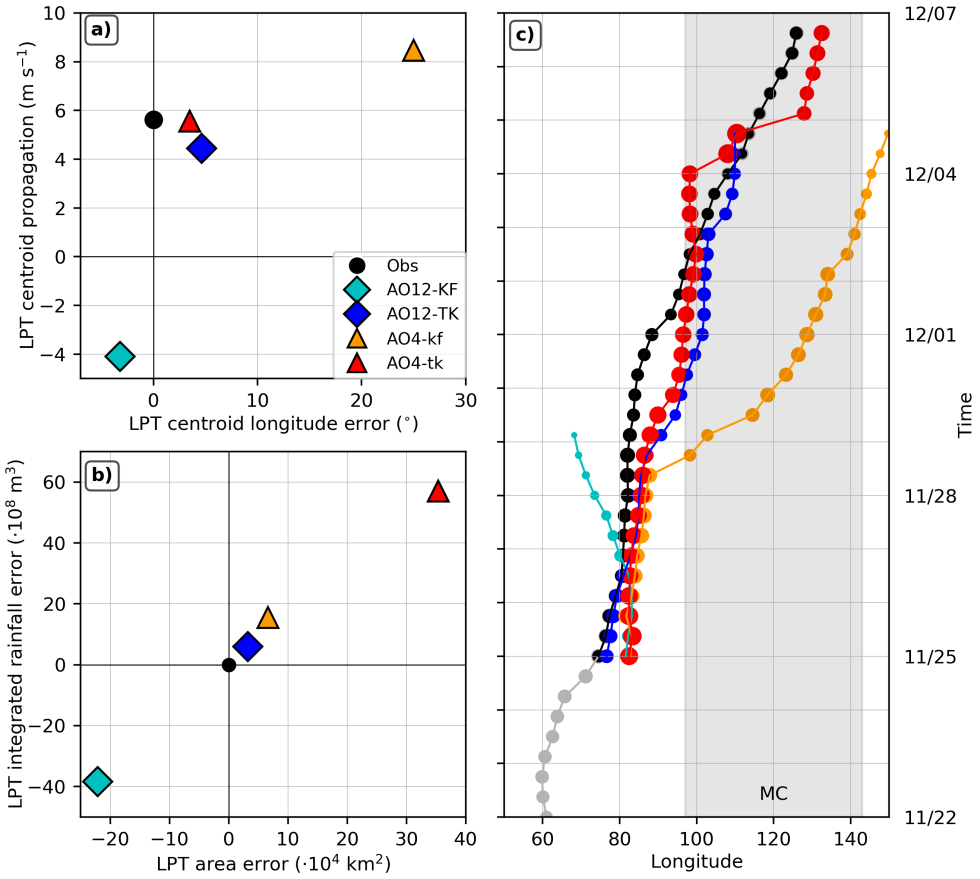

Figure 2.4: LPT characteristics: a) LPT centroid propagation speed (m s^{-1}) vs the error in its longitudinal position (°); b) errors in total rainfall within the LPT (m^3) and its area (km^2); c) the longitudinal position of the LPT centroid in time. The area of circle markers in c) is proportional to LPT area at a given time.

2.4.2 Precipitation

In this section, the characteristics of MJO precipitation in model simulations are quantitatively compared with observations. Time series of precipitation averaged over the equatorial IO are shown in Fig. 2.5 and the differences between model simulations and observations highlight the precipitation biases in the model. The area over which the precipitation is averaged at each time is highlighted in red on the inset on the bottom left of Fig. 2.5. 3-hourly

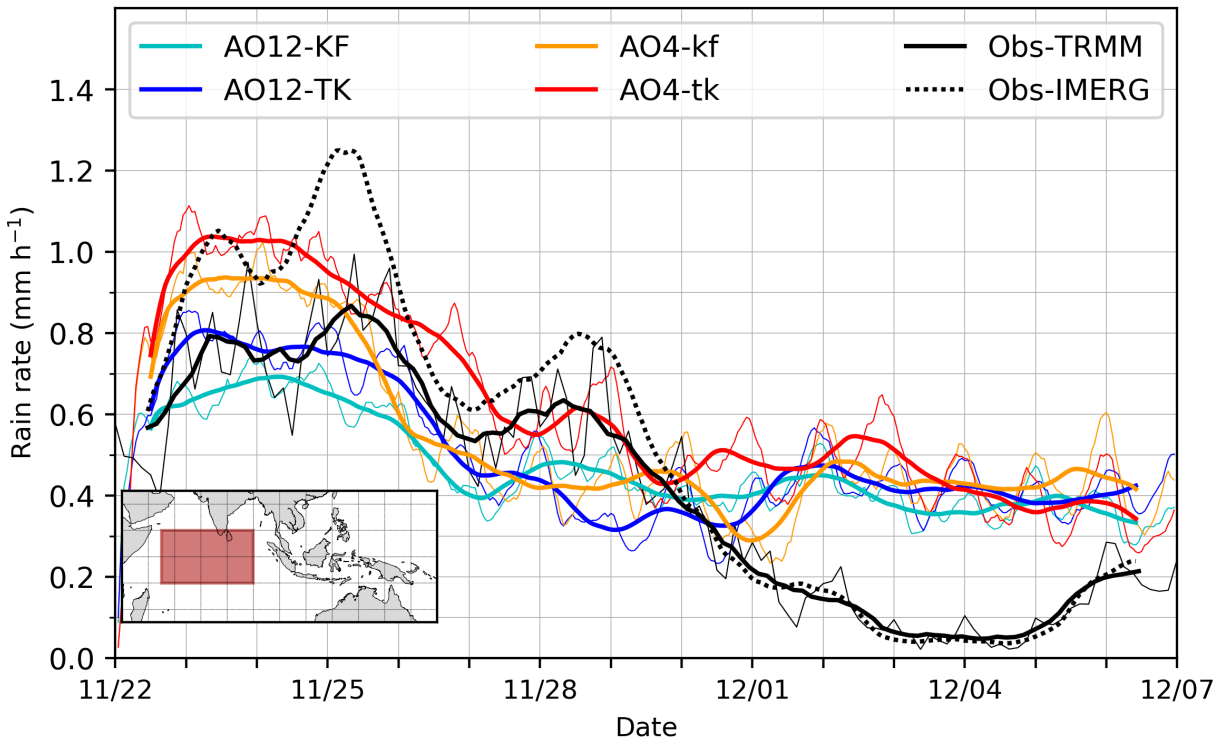

Figure 2.5: Time series of 3-hourly (thin lines) and 24-hour mean rain rate (thick lines, mm h^{-1}) over the equatorial IO region, highlighted in red on the map inset, bottom left (55-90°E, 10°S-10°N).

time series are shown in thin solid lines, and they show the diurnal variability of precipitation. Thick solid lines show the same timeseries smoothed using a 24-hour running mean which removes high-frequency variability. Observations are shown in black, with the solid lines showing the lower-resolution TRMM, and the dashed lines showing the higher-resolution GPM-IMERG data (only the smoothed time series is shown for IMERG).

The active and suppressed MJO signals are clearly visible over the IO in both observational datasets. TRMM and IMERG show nearly identical rain rates in the convectively suppressed period (after 1 December), but there is a large discrepancy between them during the active MJO (before 1 December), where TRMM produces rain rates that are consistently lower than those of IMERG, by as much as 30%. The difference between the observed

datasets presents a measure of observational uncertainty.

In model simulations, IO-averaged precipitation is reduced as the MJO propagates out of the IO, but the suppression of precipitation is never as strong as observed. To remove the precipitation bias produced by individual model simulations, we define a post-MJO suppression strength metric as the ratio between the mean precipitation during active and suppressed time periods. The transition between the active and suppressed periods is determined from LPT tracking as the first time the entire MJO convective envelope is located to the east of 90°E, i.e., when there is no MJO-associated precipitation over the IO. The time of the transition, along with the strength of the post-MJO suppression and averages for the entire period are recorded in Table 2.2. AO12-KF results are not separated into active and suppressed phases as that simulation did not produce an MJO.

Simulation	Transition Time	Total Mean (mm h^{-1})	Active MJO (mm h^{-1})	Suppressed MJO (mm h^{-1})	Active / Suppressed
AO12-KF	-	0.468	-	-	-
AO12-TK	3 Dec, 08Z	0.500	0.529	0.404	1.3
AO4-kf	29 Nov, 06Z	0.539	0.667	0.418	1.6
AO4-tk	5 Dec, 03Z	0.613	0.650	0.348	1.9
TRMM	3 Dec, 03Z	0.416	0.520	0.114	4.6
IMERG	3 Dec, 03Z	0.505	0.643	0.109	5.9

Table 2.2: Mean precipitation rates (mm hr^{-1}) over the IO (55-90°E, 10°S-10°S) during MJO active and suppressed periods, and suppression strength (the ratio of active to suppressed rainfall). The transition time is the first time the entirety of the MJO passes east of 90°E.

Post-MJO suppression is strongest in AO4-tk, and there is a positive relationship between the precipitation bias (or total mean precipitation) and the strength of the post-MJO suppression. AO4-tk, with its strong post-MJO suppression, is also the simulation with the highest precipitation bias compared to both TRMM and GPM-IMERG observations. AO12-

TK has the lowest mean precipitation and bias compared to observations, but also shows the weakest post-MJO suppression of precipitation. This indicates that the high-resolution simulations (with more intense precipitation) are better able to represent the wide-ranging suppression following MJO passage – likely due to a better dynamical representation of mesoscale convective systems that comprise the large-scale MJO.

2.4.3 Surface Westerly Winds

In this section, we investigate the differences in MJO dynamics among the simulations – specifically, we focus on the representation of large-scale surface westerly winds associated with the MJO. For observations, we use the CCMP surface wind analysis product, which has been systematically evaluated with DYNAMO observations by Kerns and Chen (2018). Maps of surface zonal winds at two contrasting times, 12 UTC on 24 November and 12 UTC on 5 December, are shown in Fig. 2.6. Zonal wind magnitude is shaded in color (westerlies in yellow/brown), and wind direction is indicated with grey arrows. The black contour represents the tracked MJO at the listed time, showing the location of MJO precipitation. On 24 November, the observed MJO is located between 60 and 80°E, and a broad region of surface westerly winds extends from 50-90°E along the equator and south of it (Fig. 2.6a). At that time, all model simulations show broad surface westerlies starting ∼50°E but with strong winds extending farther east compared to observations; the LPT centroid is also located to the east of the observed MJO (Fig. 2.4c). In AO12-KF, convection is organizing around a tropical cyclone (tight wind circulation in Fig. 2.6c), while MJO convection spans a broader area in other simulations.

Eleven days later, at 12 UTC on 5 December, MJO-producing simulations (AO12-TK, AO4-kf, AO4-tk) and observations all show the IO and MC covered by a broad region of surface westerly winds. The main difference among MJO-producing simulations over the IO is in the meridional extent of the westerly winds; AO12-TK has westerlies confined to the equator, while they extend farther poleward in AO4 simulations and observations. At this time, the observed MJO is located between 110 and 130°E (Fig. 2.6b). The MJO

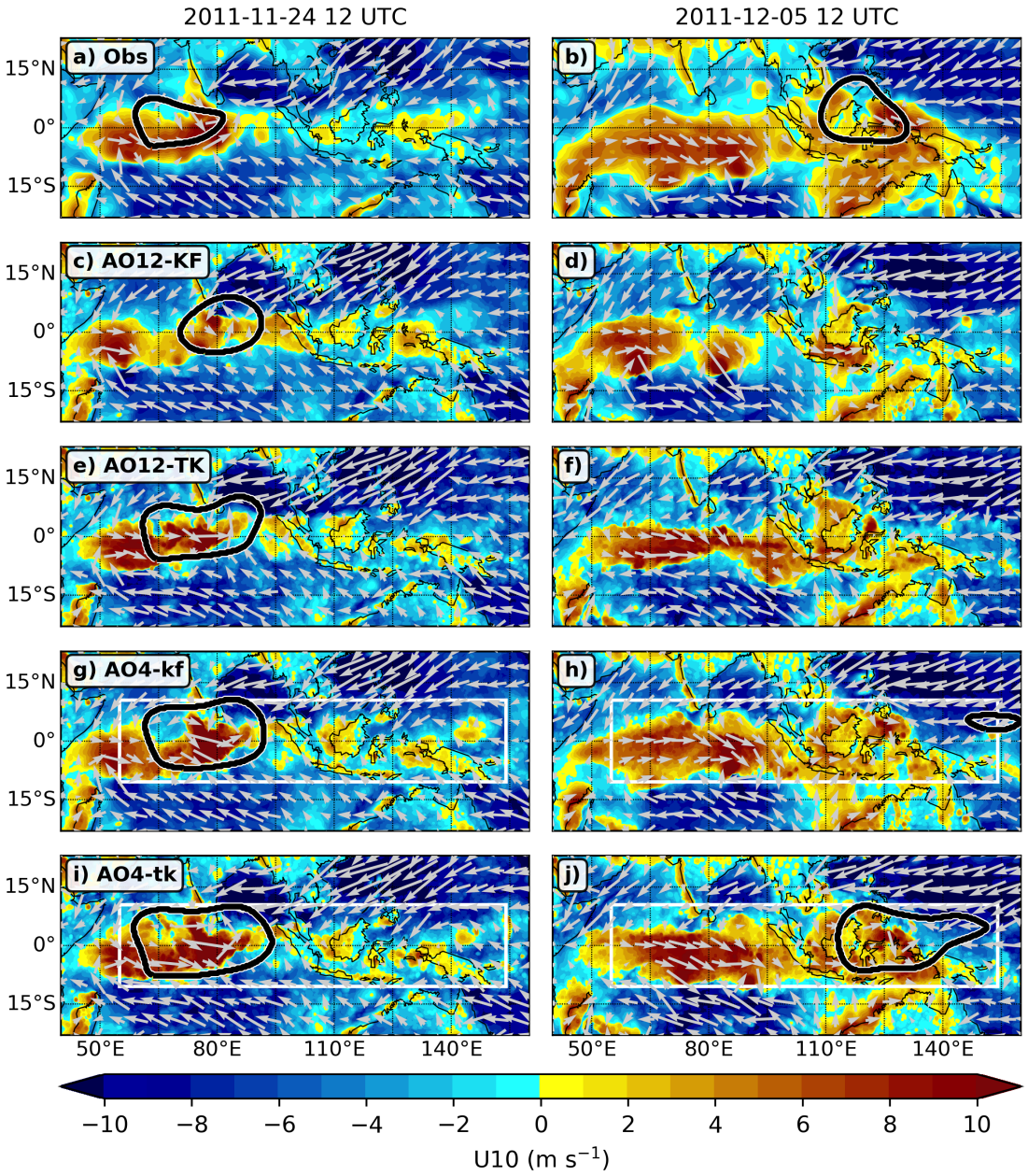

Figure 2.6: Surface zonal winds (magnitude and direction) and LPT envelope (black contour) at 12 UTC on 24 November (left) and 5 December (right) from CCMP (a, b) and model simulations as follows: AO12-KF (c, d), AO12-TK (e, f), AO4-kf (g, h), and AO4-tk (i, j). White lines show the boundaries of the high-resolution domain (D03) in AO4 simulations.

in AO12-TK has dissipated, and the MJO in AO4-kf has become decoupled from surface westerlies and is located east of 145°E (Fig. 2.6h). The MJO precipitation in AO4-tk is just to the east of the observed MJO and covers a larger area but remains associated with the surface westerly winds over the MC. AO12-KF shows no continuous surface westerlies, but has developed two tropical cyclones in the southern IO (Fig. 2.6d).

2.5 Atmospheric Boundary Layer Structure

Surface westerly wind bursts associated with the MJO are related to formation of deep convection at or near the equator Seiki and Takayabu (e.g. 2007). Robert A. Houze et al. (2000) have shown that strong surface westerly winds are enhanced by downward westerly momentum transport associated with large convective systems within the MJO. The vertical structure of the large-scale descending jet was first observed during DYNAMO using aircraft observations with the GPS dropsondes and described by Chen et al. (2016). An example of one such system occurred on 24 November 2011. The model simulations and their comparison with observation are shown in Fig. 2.7. The top row shows the system as was observed – using satellite observations and vertical cross-sections along the equator created by using observations from aircraft-released dropsondes. Fig. 2.7a shows a map view of the large convective system – TRMM rain rate in grey gives an indication of the scale of the system (on the order of 1000 km across). CCMP surface wind vectors show strong surface westerly winds throughout the system and to its west. The leading edge of the convective system is located near 85°E and bowing westward away from the equator. The black line shows the NOAA WP-3D aircraft track, and the large magenta circles show the dropsondes released as the plane was flying along the equator from east to west – those are the dropsondes used to create the equatorial cross-sections shown in the middle and right columns (winds – Fig. 2.7f, and relative humidity – Fig. 2.7k). The vertical cross-sections show that behind the leading edge of convection, a strong westerly jet descends from an altitude of 3-4 km all the way to the surface. The RH cross-section shows high moisture in the areas of the jet and near the surface. The star-shaped markers indicate the height of the ABL, which is defined

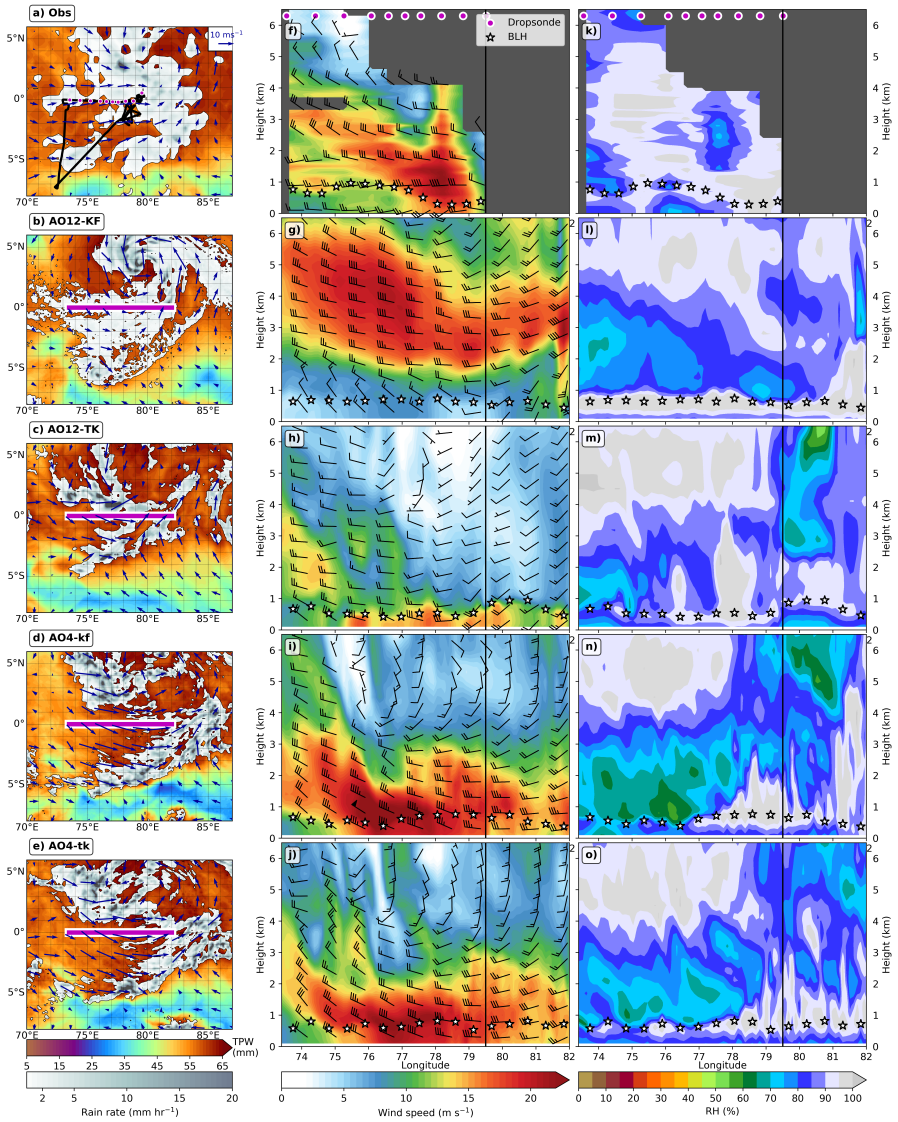

Figure 2.7: A large MJO equatorial convective event observed on 24 November 2011 (after Chen et al. (2016), their Fig. 6). Observations are shown in the top row (a, f, k), with model experiments below as follows: AO12-KF (b, g, l), AO12-TK (c, h, m), AO4-kf (d, I, n), and AO4-tk (e, j, o). The left row shows total precipitable water (mm, color), TRMM rain rate (mm hr^{-1}, greyscale) and CCMP surface winds (arrows) at 12 UTC, along with the WP-3D aircraft flight track (black line) and released dropsondes along the equator (magenta circles). Dropsonde data is used to construct vertical cross-sections of wind speed and direction (middle), and RH (right). Stars on vertical cross-sections indicate the atmospheric boundary layer height (BLH).

as the height at which the difference between virtual potential temperature and its surface value first exceeds 0.5K.

All simulations show a large convective feature located in the region, with stark differences among AO12-KF, AO12-TK, and AO4 simulations in terms of the vertical structure of winds and RH. As the leading edge of convection in model simulations is located to the east of the observed system, the vertical cross-sections span a wider range of longitudes (thick magenta line). In AO12-KF, we see a closed center of rotation associated with a developing tropical cyclone, and a broad region of trailing precipitation south of the equator (Fig. 2.7b). The vertical cross-sections show a strong elevated westerly jet above 2 km; however, surface winds are very weak and only slightly westerly, with more cross-equatorial flow associated with rotation than along-equatorial flow associated with the MJO (Fig. 2.7g). High RH values along the cross-section show a broad region of clouds above 4 km, and a narrow saturation band near the surface. The situation can be contrasted with AO12-TK, where the precipitation associated with the convective system is less coherent (Fig. 2.7c), and strong winds are mostly confined to the ABL (Fig. 2.7h). However, there is a small region of stronger winds aloft, associated with high RH values at the trailing edge of the broad stratiform region (Fig. 2.7m).

With increased resolution, the representation of the convective system is improved in terms of precipitation and surface winds – regardless of the CP imposed on the outer two domains. The leading edge of the convective system is better defined to the east of the observed one. Both AO4 simulations show high RH values above 4 km, which can indicate the presence of stratiform clouds, and both show a strong jet of westerly winds descending from the bottom of the saturated area to the surface (Fig. 2.7i, j, n, o). The main difference between AO4 simulations is the presence of drier air above the ABL in AO4-kf in the western half of the cross-section.

A notable difference among simulations is related to the height of the ABL and its relation to lower-tropospheric moisture and saturation, most obviously seen in the RH cross-sections (Fig. 2.7, right). In AO12-KF, a strong RH maximum is collocated with the top of the ABL

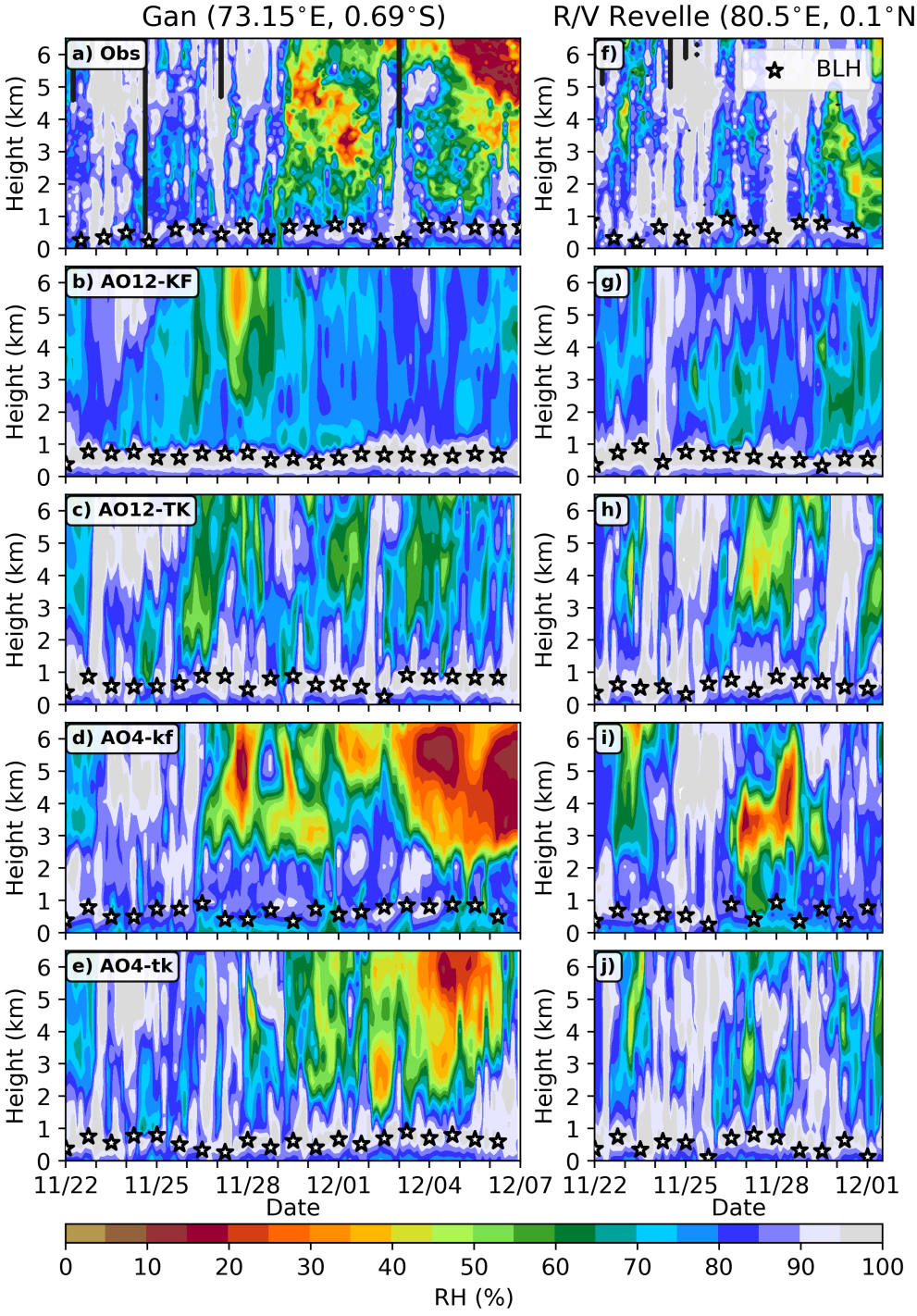

Figure 2.8: Time evolution of RH profiles at Gan (left) and R/V Revelle (right) from top to bottom: sounding observations (a, f), AO12-KF (b, g), AO12-TK (c, h), AO4-kf (d, i), AO4-tk (e, j). Stars mark the atmospheric boundary layer height.

indicating there is a lack of mixing between the ABL and the free troposphere above it. This does occur in MJO-producing simulations, but not nearly as frequently. This characteristic top-of-the-ABL saturation followed by a sharp decrease in RH right above the ABL is not only a feature of this cross-section but can be seen over the IO throughout the 15-day simulation. Fig. 2.8 shows time series of vertical profiles of RH at two sounding sites during DYNAMO – a land site at Gan Island, and a ship site on R/V Revelle (marked as G and R on Fig. 2.1, respectively) – created from soundings and model simulations. The Gan soundings span the entire modeled period, while the R/V Revelle soundings are only shown until 1 December, after which the ship moved away from its equatorial location. Stars mark the height of the atmospheric ABL. Both sites show a moist environment with some drying of the lower- and mid- troposphere - after 29 November at Gan, a day later at R/V Revelle, indicating that the active phase of the MJO has propagated to the east.

The sharp and prominent RH maximum near the top of the ABL is nearly always present in AO12-KF, with little variability in the ABL height (BLH) (Fig. 2.8b, g). In addition, AO12-KF is missing the strong low- and mid-level drying in the second half of the simulation. Other simulations show more varied BLHs, as well a broader vertical range of high RH values. The low-mid-level drying is best represented in AO4 simulations, with the onset of drying occurring earlier in AO4-kf than in AO4-tk.

This peculiarity with the saturated ABL top in AO12-KF, and the stark difference to its state in AO12-TK, illustrates an important point: different CPs can strongly affect the processes in the ABL through shallow convection mixing at the top of the boundary layer – even though everything else in the simulations is identical. This is evident in Fig. 2.9, which shows the vertical distributions of RH (top) and zonal winds (bottom) from the Gan and R/V Revelle soundings shown in Fig. 2.8, and their model counterparts. The vertical coordinate has been changed to a linear pressure scale to better emphasize the differences near the surface, and the horizontal black lines indicate BLHs. The observed profiles are shown on the left, with a relatively moist structure near the surface, followed by a wider range of RH values aloft consistent with tropospheric drying in the second half of the modeled period.

There is a slight RH maximum near the top of the ABL, but there is very little drying above it, which indicates there is mixing occurring. BLHs vary between 1000 and 900 hPa. This coincides with surface westerly winds (peak is near 5 m s^{-1}), amplifying with height to ∼800 hPa, then weakening and slowly transitioning to easterly winds in the upper troposphere. The peak winds between 850 and 700 hPa are associated with the midlevel jets such as the one shown in Fig. 2.7.

In AO12-KF, the RH profiles are largely uniform – with a pronounced RH peak at the top of the ABL, which is generally invariant and confined between 900 and 950 hPa. The surface winds are weak (frequency peak is below 5 m s^{-1}), with a larger portion of surface winds being easterly. Zonal winds aloft can get very strong, suggesting that the scenario described in Fig. 2.7 is not a singular occurrence - a westerly wind jet in the free troposphere that does not penetrate to the surface. This implies that the saturated layer of air at the top of the boundary layer can act as a thermodynamic barrier to the mixing of momentum from the free troposphere into the ABL, and that shallow convection is not very active in the simulation. The strong westerly wind jets above the ABL do not contribute much to the reinforcement of surface westerlies, which leads to the failure of AO12-KF in simulating an MJO event, both in terms of surface westerlies, and in terms of its eastward propagation. Without strong winds near the surface, there is not enough moisture to sustain large-scale precipitation on the MJO scale.

Vertical profiles of RH and winds from AO12-TK vertical profiles show a sharp contrast to those in AO12-KF. RH is relatively uniform up to 800 hPa with stronger westerly winds near the surface, suggesting strong mixing across the top of the ABL. In this case, the moderately-strong westerly winds in the free troposphere are very efficiently mixed to the surface, amplifying the surface westerly winds, creating conditions favorable for the eastward propagation of large-scale precipitation. The variability of ABL height is greater than in AO12-KF, and the mid- and upper-level drying is improved compared to AO12-KF. So even though the parameterization of the ABL processes is identical in both AO12 simulations, the difference CPs result in very different conditions within the ABL. This shows that mixing

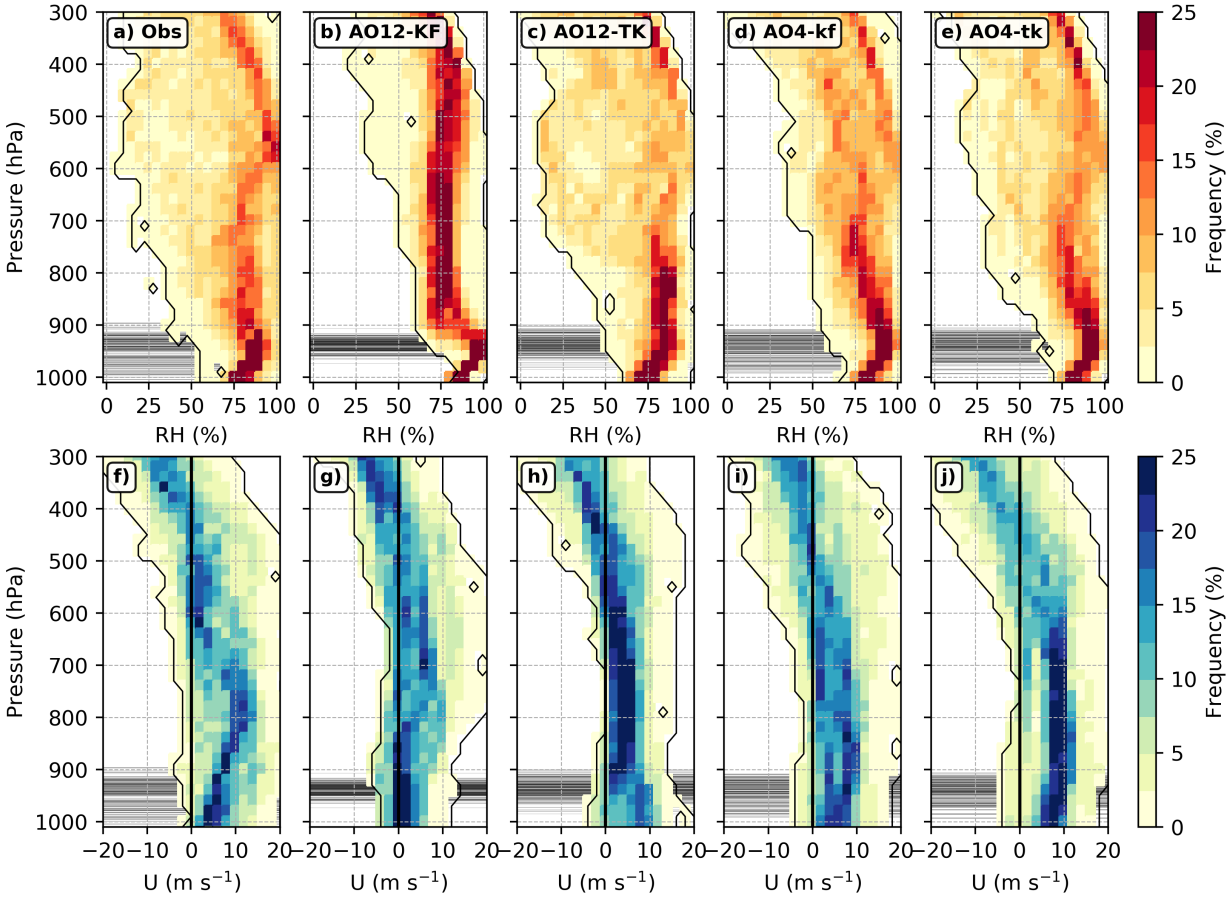

Figure 2.9: Vertical distributions of RH (%, top) and zonal wind (m s^{-1}, bottom) from locations of Gan and R/V Revelle. Observations are shown on the left (a, f), followed by model simulations as follows: AO12-KF (b, g), AO12-TK (c, h), AO4-kf (d, i), and AO4-tk (e, j). Black outlines indicate the total range of the distributions, while the horizontal black lines show the range of BLH.

across the top of the ABL can strongly affect the dynamics of the entire MJO. Between the two extremes, overmixing in AO12-TK has a favorable effect on the simulation of the MJO, while undermixing in AO12-KF is detrimental. Increasing the resolution to convection-permitting scales (bypassing the CP), as is the case in AO4 simulations improves the vertical structure of the ABL and free troposphere above it, both in terms of RH and westerly winds.

These profiles agree well with DYNAMO sounding observations described by Johnson and Ciesielski (2017). The mid-level drying is improved from AO12-KF to AO4-kf, though it is still better represented in AO4-tk.

2.6 Summary and Conclusions

High-resolution, fully coupled atmosphere-ocean model (UWIN-CM) and observations from the DYNAMO field campaign are used to investigate physical processes affecting MJO precipitation and eastward propagation. UWIN-CM experiments with varying model resolution and moist physics provided new insights to how processes that seem critical for a successful simulation of the MJO are represented in numerical models. The main results can be summarized as follows:

- At low (12 km) grid resolution, the choice of CP is the determining factor for the simulation of MJO precipitation and eastward propagation. The Tiedtke CP produced an eastward propagating MJO while the Kain-Fritsch CP did not (Figs. 2.3b, c).

- Using different CP in low-resolution simulations results in a vastly different atmospheric ABL structure that has a major impact on MJO dynamics (Figs. 2.7, 2.8, 2.9). Kain-Fritsch CP produced an overly saturated, cloudy boundary layer that is decoupled from the free troposphere, which is prohibitive to large-scale westerly winds from descending to the surface and the maintenance of large-scale convection (Figs 2.7g, l).

- With convection-permitting (4 km) resolution, explicit moist physics and no CP, model simulations improve the structure of convective systems and the structure of the ABL (Figs. 2.7i, j). This results in a more realistic vertical structure of winds and moisture in the troposphere (Fig. 2.9), as well as improved MJO precipitation, eastward propagation, and post-MJO suppression.

These results are consistent with previous studies on the topic, though few have been performed at such high resolution (e.g., Holloway et al., 2013; Jia et al., 2010; Pilon et al.,

2016). The simulations with different CPs at low resolution start diverging early on, especially in terms of large-scale precipitation organization and surface westerly winds (Figs. 2.2, 2.3, 2.6). AO12-TK produces smooth-propagating large-scale convection that dissipates over the MC, while AO12-KF is over-aggressive at producing rotation near the equator. The transition from parameterized to explicit moist physics improves the simulation of the MJO in most aspects examined in this study. The eastward propagation of precipitation is clear in both high-resolution convection-permitting simulations, though the large-scale precipitation in AO4-kf rapidly propagates eastward and becomes decoupled from the surface westerly winds (Figs. 2.4c, 2.6h). AO4-tk maintains a slower and more consistent eastward propagation (Figs. 2.2, 2.3, 2.4). AO4 simulations show a high precipitation bias, mostly in the suppressed regime after the MJO has passed out of the IO (Fig. 2.5). The positive precipitation bias is a result of a high bias in air-sea latent heat flux, which is addressed in a companion paper by Savarin and Chen (2022b). None of the model simulations can reproduce the suppressed phase of the MJO to the extent that we see in observations (Fig. 2.5).

Both the Kain-Fritsch and Tiedtke CPs include representation of deep and shallow convective processes, but use different convective triggers; an inaccurate representation of shallow convection would result in an inaccurate representation of mixing between the ABL and the free troposphere. Torn and Davis (2012) found that shallow convection in the KF CP is triggered in conditions that are not frequently observed over ocean, and its tunable parameters were adjusted to reduce errors over land, not over ocean. The TK CP implements higher rates of entrainment for shallow convection than it does for deep convection, increasing mixing across the ABL top by an order of magnitude, and improving the representation of boundary layer clouds Zhang et al. (2011). The results of our study agree with previous work in that a lack of mixing in AO12-KF could be due to insufficient triggering of shallow convection over ocean; in AO12-TK, shallow convection is triggered more often, and higher entrainment results in overmixing (Fig. 2.9). Additionally, the TK CP accounts for effects of convective momentum transport, while the KF CP does not, which explains why we see

strong surface westerlies in AO12-TK and not in AO12-KF. Previous studies (e.g., Mallard et al., 2013) show that lack of convective momentum transport can lead to overproduction of tropical cyclones, which is also evident in our AO12-KF simulation – we see multiple tropical cyclones and weak surface westerly winds under strong mid-level jets (Figs. 2.6, 2.7, 2.9). It is also important to note that the CP behavior can be dependent on the model resolution, and that the convection triggering behavior might be different if our 12-km resolution simulations (AO12-KF, AO12-TK) were run at even lower resolutions – a study by Song and Zhang (2018) found that convection frequency by CPs decreased when resolution was increased.

The large-scale descending westerly jet associated with mesoscale convective systems is an important feature of the MJO, as described in observational studies by Robert A. Houze et al. (2000) and Chen et al. (2016). An idealized modeling study by Mechem et al. (2006) showed that westerly jets in stratiform regions of MCSs help bring westerly momentum all the way to the surface, contributing to the establishment and maintenance of surface westerlies in the MJO. The cloud permitting AO4 simulations can reproduce this observed feature very well, whereas the low resolution AO12 simulations cannot, which results in large differences in ABL structure between AO12 and AO4 simulations. The saturated top of the boundary layer in AO12-KF effectively decouples the free-tropospheric winds from the surface, resulting in strong westerly jets aloft, but only a weak response at the surface – and no MJO. On the opposite end of the spectrum, AO12-TK produces strong mixing into the boundary layer, efficiently distributing westerly winds and moisture through the lowest 3 km and producing a strong eastward propagating MJO event. The improvement of the representation of surface westerly wind bursts and MJO propagation in convection-permitting simulations provides further evidence that the extreme mixing profiles in AO12-KF and AO12-TK come as an undesirable consequence of the interaction between the convective and boundary layer parameterizations.

In conclusion, the coupled atmosphere-ocean model with convection-permitting resolution (4 km) can better represent not only the moist convective processes, but also the ABL struc-

ture and the large-scale circulation associated with the MJO. The interplay between various moist physics parameterizations and their interaction with the ABL can have a profound influence on the MJO simulations of precipitation and surface wind. The atmosphere-ocean coupling also plays a critical role in model simulations of the MJO as will be shown in Part 2 of this study (Savarin and Chen, 2022b).

While the results presented here are based on a case study of the November-December 2011 MJO event, many other modeling studies have touched on some aspects of the physical processes discussed here and shown results consistent with what we have presented here. First, all studies using convection-permitting resolutions or cloud-resolving models without CPs show improved MJO representation (e.g., Holloway et al., 2013; Miyakawa et al., 2014; Stan et al., 2010), while studies performed at lower resolutions find that choosing a CP can make or break an MJO simulation (Boyle et al., 2015; Chang et al., 2019). Generally, CPs with moisture-convergence type triggers, of which the TK CP is an example, have a better track record with MJO simulations than other types of CPs (e.g., Hung et al., 2013). Multiple studies have noted the importance of shallow convection, with experiments showing that when shallow convection is weakened or not present (or, in the case of AO12-KF, not being triggered), the simulated MJOs become weaker Cai et al. (2013); Pilon et al. (2016). There is also general consensus that higher entrainment rates, and the accompanying stronger mixing by shallow convection improve MJO representation (Hannah and Maloney, 2011; Hirons et al., 2013), all of which agree with the results of this study. There is some disagreement on the role of convective momentum transport in MJO simulations, with some studies showing improved MJOs when convective momentum transport was removed from the CP (Klingaman. and Woolnough, 2014), while other studies note an improvement when it is added (Zhou et al., 2012). Based on our results, the relative roles of convective momentum transport and shallow convection cannot be evaluated, since we do not know whether the failure of the AO12-KF to produce an MJO was due to the lack of triggering of shallow convection, or the missing component of convective momentum transport, which are both present in AO12-TK. However, they should be further evaluated in future studies.

Chapter 3

IMPACTS OF ATMOSPHERE-OCEAN COUPLING ON THE UPPER OCEAN AND MJO PROPAGATION

Savarin, A., & Chen, S. S. (2022). Pathways Pathways to Better Prediction of the MJO: 2. Impacts of atmosphere-ocean coupling on the upper ocean and MJO propagation. Journal of Advances in Modeling Earth Systems, 14, e2021MS002929 https://doi.org/10.1029/2021MS002929.

3.1 Abstract

This study investigates effects of atmosphere-ocean coupling on MJO precipitation and eastward propagation, and upper ocean conditions during and after MJO passage. To explore pathways for improving MJO prediction, three model experiments are conducted using the Unified Wave Interface-Coupled Model (UWIN-CM) at convection-permitting (4 km) resolution: 1) uncoupled atmosphere-only, 2) coupled atmosphere-ocean, and 2) coupled atmosphere-ocean with improved air-sea flux algorithm simulations. The model simulations are compared with observations from the DYNAMO field campaign in 2011. Both coupled atmosphere-ocean simulations produced eastward propagation of the MJO where the uncoupled, atmosphere-only simulation did not. The uncoupled model overestimates both precipitation and surface winds associated with the MJO, while coupled model simulations substantially reduce model bias. Improved air-sea fluxes lead to systematic improvements in precipitation, winds, sea surface temperature, and the ocean mixed layer when compared to the original coupled simulation. This leads to further improvement of the MJO's eastward propagation speed compared with observations. Despite these improvements, the regional coupled simulations still have difficulty representing the extent of convectively suppressed conditions in the Indian Ocean after MJO passage, which indicates the importance of the large-scale environment from lateral boundary conditions. Coupled model simulations also reveal some issues in the representation of upper ocean stratification in the ocean model, especially errors in salinity, which result in overestimation of the mixed layer depth after MJO passage.

3.2 Introduction

The Madden-Julian Oscillation (MJO) is an atmosphere-ocean coupled phenomenon characterized by an alternating pattern of enhanced and suppressed precipitation initiating in the Indian Ocean (IO) and propagating eastward across the Maritime Continent (MC) and western Pacific (Madden and Julian, 1971, 1972; Zhang, 2005). The precipitation pattern is accompanied by changes in surface winds and upper ocean temperature. Although it is the leading source of tropical intraseasonal variability, its prediction remains a major challenge in numerical weather prediction (Hung et al., 2013; Ling et al., 2014; Zhang, 2005, 2013). Some studies show that the inclusion of atmosphere-ocean interaction improves the prediction of the MJO, especially its eastward propagation (DeMott et al., 2015; Klingaman. and Woolnough, 2014; Wang et al., 2015; Zhang et al., 2006).

Observational studies of the MJO using satellite data and observations from two major field campaigns, the Tropical Ocean-Global Atmosphere - Coupled Ocean-Atmosphere Response Experiment (TOGA COARE) in 1992-1993 (Webster and Lukas, 1992) and the Dynamics of the MJO in 2011-2012 (Yoneyama et al., 2013), have led to better understanding of the MJO. They have shown that the MJO convection and atmospheric boundary layer have multiscale variability (e.g., Chen et al., 1996; Johnson and Ciesielski, 2017) and air-sea interaction occurs from the diurnal to intraseasonal time scales (Chen and Jr, 1997; Chen et al., 2016; de Szoeke et al., 2015; Fairall et al., 2003; Feng et al., 1998; Shinoda and Hendon, 1998; Weller and Anderson, 1996). During the convectively suppressed periods of the MJO, increased insolation and weak winds lead to a warm and stably stratified ocean mixed layer (Anderson et al., 1996). During the convectively active periods of the MJO, intense convection, precipitation and strong winds develop, deepening the oceanic mixed layer and cooling the upper ocean (de Szoeke et al., 2015; Moum et al., 2014) while providing moisture to sustain atmospheric precipitation.

Numerical modeling studies have revealed various aspects of the MJO convection and air-sea interaction and their impacts on the MJO. Models representing convection using

super-parameterization in global models (Benedict and Randall, 2009) or explicitly using cloud-permitting resolution (e.g., Savarin and Chen, 2022a) can improve model simulations of the MJO. So does incorporating prescribed varying SST (Miura et al., 2009; Wang et al., 2015), a simple mixed-layer ocean model (Benedict and Randall, 2011), or a fully coupled dynamic ocean model (DeMott et al., 2014; Shinoda et al., 2013). Some early studies used a fixed-depth mixed layer model to incorporate intraseasonal SST anomalies on top of a seasonal cycle and found that even intraseasonal temperature changes of 0.1-0.15°C improved MJO variability and propagation (Waliser et al., 1999). In simple mixed-layer models, the SST cooling is mostly determined by the thickness of the slab ocean, with shallower mixed layers producing more SST variability, and thicker mixed layers producing less (Marshall et al., 2008). Observed SST variations induced by the MJO can exceed 1°C (Lau and Sui, 1997). Over the course of an MJO event, wind mixing from strong surface westerlies can rapidly deepen the ocean mixed layer, and entrainment of cooler water from below can further modify the mixed layer and SSTs (Lukas and Lindstrom, 1991), making the case for use of dynamic ocean models.

Air-sea interaction can have a significant influence on atmospheric moisture and convection associated with the MJO. Marshall et al. (2008) found that the inclusion of atmosphere-ocean coupling with a slab ocean model can improve MJO representation through enhancing the moisture-convergence feedback already present in the atmosphere. The additional variability provided by ocean models results in increased SST ahead of MJO precipitation, where clear skies permit warming, and weak winds induce surface heat fluxes, warming and moistening the atmospheric boundary layer. This leads to increased moistening in the atmosphere, convergence, and results in increased surface westerlies and precipitation to the east of MJO convection, promoting eastward propagation of the MJO. The SST cooling induced by the MJO due to increased cloudiness, strong surface winds, and high air-sea fluxes can help shut down MJO convection to the west. This also explains why models that rely on convective parameterizations tend to produce better MJO events when their convection is triggered by moisture convergence (e.g., Liu et al., 2022; Savarin and Chen, 2022a). A study by Maloney

and Sobel (2004) showed that by eliminating the MJO-induced surface heat flux variability, MJO precipitation becomes decoupled from the surface wind signal. Thus, an accurate representation of air-sea heat fluxes is important for accurate simulations of MJO propagation and interactions between its precipitation and circulation. But air-sea fluxes are hard to represent in models, and even reanalysis products contain significant biases when compared to in-situ observations, such as those measured during the Dynamics of the MJO field campaign (Gao et al., 2016).

Studies of upper-ocean processes and variability associated with the MJO are limited by observations, in part due to the difficulty of observing upper ocean structures from satellites and in situ observations at sparse mooring locations. Nevertheless, there are a number of studies that delve deeper than the surface properties of the ocean, such as sea surface temperature, currents, and air-sea fluxes, for example, from the RAMA mooring array in the IO (McPhaden et al., 2009) and ship observations during field campaigns (e.g., Moum et al., 2016). Studies using observations and models show that enhanced zonal advection, vertical mixing, and formation of barrier layers in the upper ocean can significantly affect the near-surface temperature and SST evolution (Halkides et al., 2015; Jensen et al., 2015; McPhaden and Foltz, 2013). In addition to understanding ocean processes alone, Shinoda et al. (2013) find that the enhancement of eastward upper-ocean currents by the MJO is strongly dependent on the strength of the surface westerly winds; lower-resolution simulations produce weaker winds, weaker upper-ocean currents and weaker horizontal advection during active MJO. For improved forecasting of MJO events without prior knowledge of SST variability, it is imperative to better understand, and accurately represent processes in the upper ocean that can help cool or warm SST in different phases of the MJO.

In this study, we investigate impacts of the atmosphere-ocean coupling on the MJO prediction using the Unified Wave Interface-Coupled Model (UWIN-CM) at convection-permitting (4 km) resolution. We compare three model experiments: 1) uncoupled atmosphere-only, 2) coupled atmosphere-ocean, and 3) coupled atmosphere-ocean with improved air-sea flux algorithm using observations from DYNAMO. We analyze the response of MJO precip-

itation and its eastward propagation, as well as post-MJO ocean recovery, to the representation and biases in air-sea heat fluxes. In section 3.3, we describe the atmosphere-ocean coupled model used for the study, the configuration of experiments, the method for identifying and tracking the MJO, and the data used for model evaluation. The large-scale MJO precipitation, surface wind structure, and SST cooling are described in section 3.4. Section 3.5 focuses on the analysis of air-sea fluxes and their biases over the equatorial IO, and how local air-sea flux differences can lead to basin-wide changes in the MJO. Section 3.6 focuses on the upper-ocean evolution during the MJO event, and the processes through which surface conditions affect SST cooling induced by the MJO. Summary and discussion of the results are presented in section 3.7.

3.3 Model and Data

3.3.1 Model Configuration

The numerical model used in this study is the Unified Wave Interface – Coupled Model (UWIN-CM; Chen and Curcic, 2016; Chen et al., 2013), which allows for interactive coupling between the atmosphere and ocean circulation models. The coupled model and configuration are the same as described in Savarin and Chen (2022a).

The atmosphere component of UWIN-CM is the Weather Research and Forecasting (WRF) model v3.6.1 with the Advanced Research WRF (ARW) dynamical core (Skamarock et al., 2008). WRF is a non-hydrostatic atmospheric model that we configure with 44 terrain-following levels in the vertical, and three nested model grids shown Fig. 3.1. The outermost domain (D01) ranges from 15.4 to 174.6°E in longitude, and from 32.0°S to 32.0°N in latitude, with a grid spacing of 36 km. Two inner nests are centered on the equator, covering the areas from 36.0 to 165.2°E and 15.3°S to 15.3°N at a grid spacing of 12 km (D02), and from 54.0 to 154.6°E and 10.6°S to 10.6°N at a grid spacing of 4 km (D03). The highest-resolution domain is convection permitting, with explicit moist physics and no CP, while D01 and D02 use CP. The surface layer parameterization is based on the Monin-Obukhov

similarity theory. The atmospheric boundary layer parameterization is the Yonsei University scheme (YSU; Hong et al., 2006). The cloud microphysics parameterization used in all three domains is the single-moment five-species scheme in WRF (WSM5; Hong et al., 2004). Initial and boundary conditions of UWIN-CM come from the European Centre for Medium-Range Weather Forecast (ECMWF) operational forecast fields as described in Kerns and Chen (2014), with boundary conditions updated every 12 hours.

The ocean circulation component of UWIN-CM is the HYbrid Coordinate Ocean Model (HYCOM) v2.2.99 (Metzger et al., 2014). HYCOM is a hydrostatic ocean circulation model with a vertical coordinate system that transitions between layers of constant density in deep water, layers of constant depth (z-levels) in shallow water and near the ocean surface, and terrain-following layers in intermediate waters. HYCOM is configured with a single domain with uniform grid spacing of 0.08°, ranging from 9.8 km at the equator to 7.7 km at the domain's northern and southern boundaries, and spans from 30.0 to 172.0°E and from 33.0°S to 33.0°N. Out of 41 vertical layers, 14 are z-layers, 5 of which are located within 15 m of the surface (centered at depths of 0.5, 1.88, 4.33, 8.16, and 12.79 m). Initial and boundary conditions come from daily mean fields of the global HYCOM analysis (Cummings, 2005; Cummings and Smedstad, 2013). Figure 3.1 shows the UWIN-CM nested model grids and the HYCOM SST analysis at the model initial time.

3.3.2 Air-Sea Flux Algorithm

To investigate the effects of the air-sea fluxes on the coupled model simulation of the MJO, we implemented a modification to the parameterization of air-sea latent and sensible heat fluxes in the WRF's surface layer parameterization. The air-sea fluxes in WRF are calculated using the bulk air-sea flux equations (Jiménez et al., 2012):

$$LHF = L_v \rho M C_q U (q_g - q_a) \tag{3.1}$$

$$SHF = \rho c_p C_h U (\theta_g - \theta_a) \tag{3.2}$$

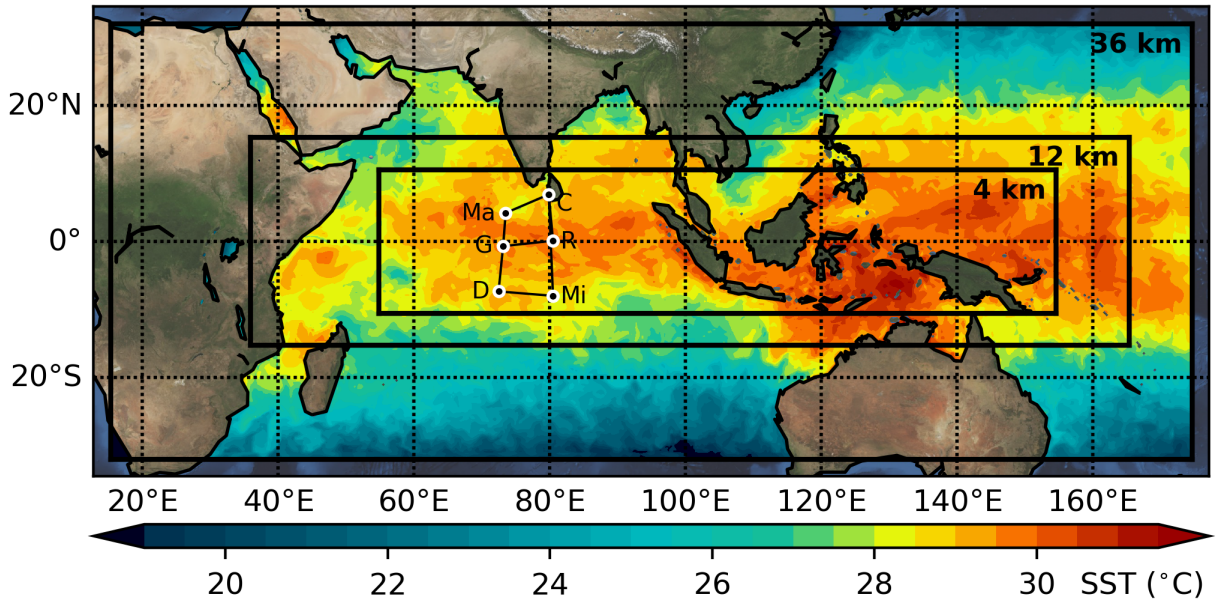

Figure 3.1: UWIN-CM domain of HYCOM and WRF nested domains at 36-, 12-, and 4-km grid spacing. Color shading shows the model initial SST from daily mean HYCOM analysis. Circle markers show locations of the DYNAMO sounding sites in the central Indian Ocean.

LHF and SHF are the fluxes of latent and sensible heat, respectively. C_h and C_q are the dimensionless bulk transfer coefficients for moisture and heat (Stull, 1988), ρ is the surface layer density, M is the soil moisture availability, and c_p is the specific heat capacity at constant pressure. q_g and q_a are the saturated ground surface specific humidity and the specific humidity of the surface layer, θ_g and θ_a are the ground surface and surface layer potential temperature. U represents the wind speed in the surface layer, which is a combination of three factors:

$$U = \sqrt{U_s^2 + u_{sg}^2 + U_{cv}^2} \tag{3.3}$$

U_s is the surface wind speed, U_{sg} is the constant sub-grid velocity (0.61 m s^{-1}, 0.43 m s^{-1}, 0.30 m s^{-1} in the 36-, 12-, and 4-km domains, respectively) (Mahrt and Sun, 1995). U_{cv}

is the convective velocity, which is parameterized based on Beljaars (1995) as:

$$U_{cv} = \begin{cases} 2\sqrt{\theta_{v.g} - \theta_{v.a}} & \text{if } \theta_{v.g} > \theta_{v.a} \\ 0 & \text{, otherwise} \end{cases} \tag{3.4}$$

$\theta_{v.g}$ and $\theta_{v.a}$ are the virtual potential temperatures of the sea surface and surface layer, respectively. When the vertical gradient of θ_v is negative across the air-sea interface, a positive convective velocity due to surface buoyancy is added to the surface layer wind speed. The data for the original parameterization was collected over land-locked Oklahoma, USA, during the Boundary Layer interaction eXperiment (BLX83; Beljaars, 1995). Most common U_{cv} magnitudes fall between 0.5 and 4 m s^{-1}, though they can reach up to 10 m s^{-1}. There are times at which U_{cv} is higher than U_s and the contribution of U_{cv} to air-sea fluxes is substantial, but this mainly occurs at $U_s < 5$ m s^{-1}. Over ocean, U_{cv} is likely smaller that over land, and we modified Eq. 3.4 by reducing U_{cv} to half if its original magnitude ($0.5U_{cv}$). The other components of surface layer winds (Eq. 3.3) remain unchanged, and it is important to note that this change is not reflected in the model output winds - it only exists within the surface layer parameterization for the purpose of calculating air-sea fluxes. Given identical environments, this modification only results in reduced air-sea latent and sensible heat fluxes.

3.3.3 Model Experiments

All experiments include a high-resolution (4-km grid spacing) inner domain in which convection is explicitly resolved by the microphysical parameterization, while the Tiedtke convective parameterization (CP; Tiedtke, 1989) is used in the two outer domains in addition to microphysics. This convection-permitting 4-km resolution is shown to best represent the MJO event compared to DYNAMO observations (Savarin and Chen, 2022a). To investigate the effects of atmosphere-ocean coupling and air-sea fluxes on the MJO simulations, we conduct three model experiments. The first model experiment is an uncoupled, atmosphere-only simulation (abbreviated as UA4). The second experiment is the coupled atmosphere-ocean

model simulation (AO4-CTRL). In the third experiment, we use the modified air-sea flux algorithm described in Section 3.3.2, which is abbreviated as AO4-FLX. The initial SST is identical in all simulations (Fig. 3.1), but remains constant throughout the simulation in UA4, while it evolves in the coupled AO4-CTRL and AO4-FLX simulations. All simulations are initiated at 00 UTC on 22 November 2011, and span 15 days, capturing the time frame of the second MJO event observed during the intense observation period of DYNAMO. At the initial time, observations show that convection is beginning to organize over the equatorial Indian Ocean (IO), while by the end of the period, the MJO has propagated over the eastern Maritime Continent (MC).

3.3.4 Ocean Mixed Layer

The method of calculating ocean mixed layer depth and ocean barrier layers is based on the variable density criterion introduced by Sprintall and Tomczak (1992), with minor modifications. The barrier layer is defined when the ocean mixed layer depth is smaller than the isothermal layer depth, and it is the ocean layer encapsulated between them. When the isothermal layer is shallower than the mixed layer, a barrier layer does not exist. To determine mixed layer depth and barrier layer thickness, we first designate a reference depth of 10 m to remove effects of diurnal variability. After this, a temperature threshold of 0.2°C is chosen for determining mixed layer properties. A temperature difference of 0.2°C from the temperature at reference depth defines the depth of the isothermal layer. Then, the coefficient of thermal expansion is calculated for that temperature difference, based on the TEOS-10 definition (the Python package *gsw* v.3.3.1 is used for the calculation). The coefficient of thermal expansion and the temperature threshold are then used to calculate the density threshold corresponding to the water column properties. The depth at which this density threshold is met is the ocean mixed layer depth. The barrier layer thickness is the difference in depths of the ocean mixed layer and the isothermal layer (when greater than zero).

3.3.5 MJO Tracking

The Large-scale Precipitation Tracking algorithm (LPT), developed by Kerns and Chen (2016, 2020), is used to track the precipitation envelope associated with the MJO. The algorithm tracks a spatially smoothed 3-day rainfall accumulation that exceeds a chosen threshold over an area larger than 3x105 km^2. In the studies by Kerns and Chen, the rainfall accumulation threshold of 12 mm day^{-1} was found to accurately capture MJO events during DYNAMO. In this study, a threshold of 15 mm day^{-1} is used instead, as model simulations tend to over-produce precipitation, compared to TRMM 3B42 observations. After precipitation is tracked, additional constraints are introduced to separate MJO precipitation from other systems. These constraints ensure that the LPT-tracked feature exhibits consistent eastward propagation and persists for at least 7 days to eliminate synoptic scale features. Using LPT to track MJO precipitation provides a major advantage over traditional MJO indices – it allows us to visualize both the spatial and temporal evolution of MJO precipitation.

3.3.6 Observational Data

The simulated MJO event occurred in late November and early December 2011, during the intense observing period of DYNAMO, while many observational platforms were operating simultaneously. This provides a unique opportunity to evaluate the model from different perspectives – including ship measurements and moorings, as well satellite data to provide large-scale context.

The data used in this study includes:

- In-situ observations:
  - Air sea fluxes at R/V Revelle (at 80.50°E, 0.10°N between 22 November and 1 December 2011 available every minute; R in Fig. 3.1) – calculating using the COARE 3.0 bulk flux algorithm Fairall et al. (2003);
  - Upper-ocean temperature and salinity from DYNAMO moorings (at 79°E, 0°N,

and 79°E, 1.5°S, hourly), and upper-ocean and surface observations from an equatorial RAMA mooring (80.5°E, 0°N, hourly) (McPhaden et al., 2009).

- Satellite products:
  - Precipitation - Tropical Rainfall Measuring Mission (TRMM) 3B42, available 3-hourly at 0.25° resolution (Huffman et al., 2007) and the Global Precipitation Measurement (GPM) Integrated Multi-SatellitE Retrievals for GPM (IMERG) v6B, available half-hourly at 0.1° resolution (Huffman et al., 2019);
  - Surface winds - Cross-Calibrated Multi-Platform (CCMP), available 6-hourly at 0.25° resolution (Atlas et al., 2011);
  - SST – Global High Resolution Sea Surface Temperature (GHRSST) Level 4 MUR Global Foundation Sea Surface Temperature Analysis, available daily at 9 km resolution (Chin et al., 2017);
  - Air-sea fluxes - Objectively Analyzed Air-Sea Fluxes (OAFlux), available daily at 1° resolution – using the COARE bulk flux algorithm 3.0 (Yu et al., 2019).
- Model initial and boundary conditions:
  - ECMWF operational analysis for the atmosphere component (updated 12-hourly at 0.25° resolution),
  - daily mean HYCOM global analysis (updated daily at 0.08° resolution)

- In-situ observations:

3.4 MJO Eastward Propagation and its Induced Upper Ocean Cooling

The traditional MJO indices such as the Real-Time Multivariate MJO Index (RMM Wheeler and Hendon, 2004) cannot be used directly in regional model analysis. Time-longitude diagrams are a useful way of examining large-scale characteristics of MJO precipitation and

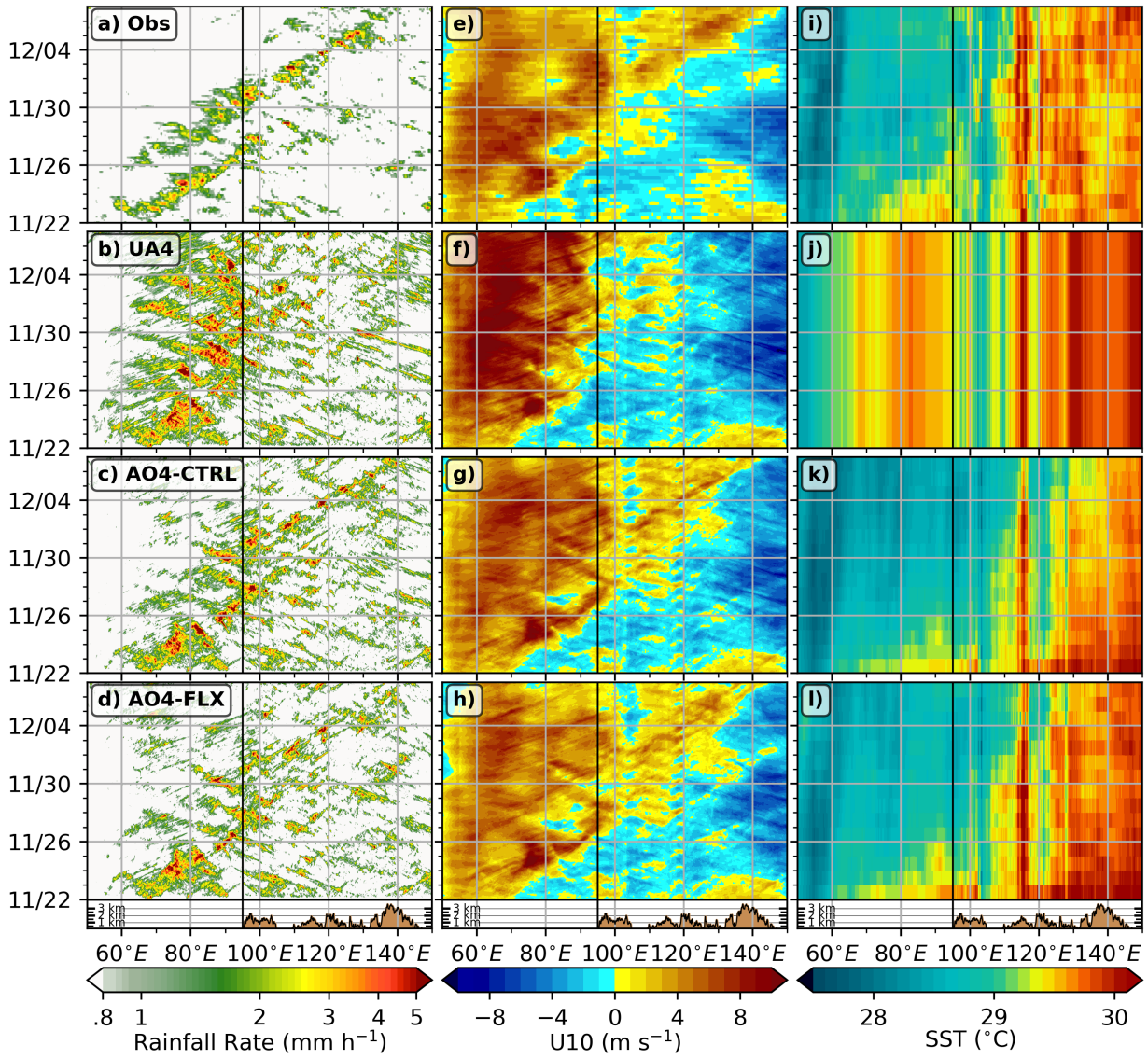

Figure 3.2: Hovmöller diagrams of rainfall rate averaged over 5°S-°N (left), surface zonal wind (middle), and SST (right) in observations (top, from left to right: TRMM 3B42, CCMP, and GHRSST) and model simulations as follows: UA4, AO4-CTRL, and AO4-FLX. Brown shading on bottom panels shows the height of maximum topography in the averaging region, separating the longitudes of the IO from those of the MC (black vertical line at 97°E).

wind patterns. Fig. 3.2 shows Hovmöller diagrams of rainfall rate (left), surface zonal wind (middle), and SST (right), averaged between 5°S and 5°N, for observations and model simulations. Observations are shown in the top row (Fig. 3.2a, e, i), using TRMM 3B42 precipitation, CCMP surface zonal winds, and OISST. The eastward propagation of MJO precipitation occurs in two distinct bursts which are part of the same convective envelope but are separated by local suppression near the equator. The leading edge of precipitation is accompanied by zonal surface wind convergence, with westerly winds extending across the IO to the west, and easterly winds to the east. The westerly winds over the equatorial IO persist, but weaken, after active MJO convection has propagated eastward into the MC, and conditions over the IO are convectively suppressed. The SST in satellite observations is reduced by up to 1°C, then begins to recover after the MJO propagates out of the IO. This cooling range agrees with observations from R/V Revelle, a ship that was stationed at 80.5°E, 0.1°N for the first 9 days of the modeled period (marked with R in Fig. 3.1), and DYNAMO and RAMA mooring observations (Fig. 3.13).

Compared to observations, all UWIN-CM simulations overproduce precipitation (Fig. 3.2a-d), but there is a clear distinction between the uncoupled (UA4) and coupled (AO4) simulations. UA4 produces intense precipitation, which is present throughout the simulation over the IO and, to a lesser extent, over the western Maritime Continent (MC). The precipitation over the IO does not propagate eastward, while AO4 simulations show a clear eastward tendency in both precipitation and surface zonal winds, with some precipitation suppression over the IO in the last days of the simulations. All simulations reproduce broad regions of equatorial westerlies throughout the IO to the west of MJO precipitation. The strongest westerlies in UA4 remain confined to the IO, and in AO4 simulations, the leading edge propagates eastward across the MC, alongside the leading edge of precipitation. Surface westerly winds in AO4 simulations are weaker than in UA4, and weaker in AO4-FLX than in AO4-CTRL. AO4-FLX winds show least bias when compared to satellite observations.

Coupled simulations also produce significant ocean cooling in the IO and western MC. AO4-FLX SST cooling is weaker compared to AO4-CTRL, but AO4-CTRL cools too much

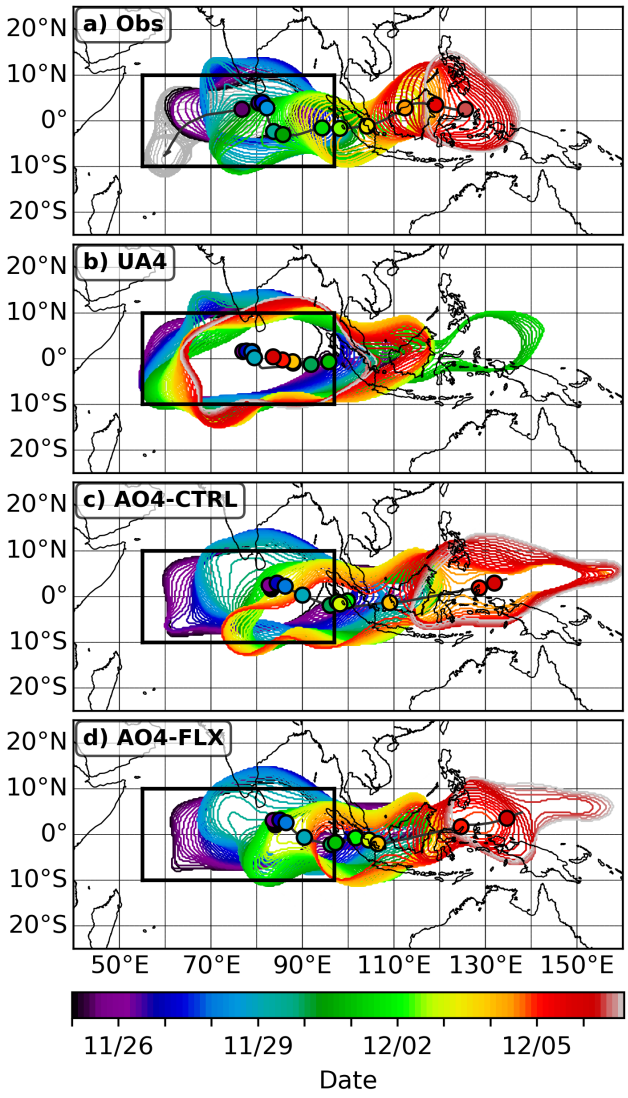

Figure 3.3: LPT evolution of precipitation in a) TRMM observations; b) UA4; c) AO4-CTRL; d) AO4-FLX. Colored contours outline the area over which the mean 3-day precipitation exceeds 15 mm day^{-1}, with color corresponding to time. The colored circles indicate the LPT centroid in 24-hour intervals.

compared to observations to begin with, so AO4-FLX shows improvement. The IO basin-wide SST change from the beginning to the end of the simulation, averaged within 5° of the equator is -1.13°C in AO4-CTRL and -0.91°C in AO4-FLX. For the same 15 days, the satellite-derived SST change is -0.47°C, but that includes the period after MJO passage, when the observed SST begins to recover. At the time when the IO-basin SSTs were lowest (30 November), the observed SST change from initial conditions was -0.58°C. In UA4, SST remains constant and identical to the initial condition depicted in Fig. 3.1, which is on average 0.5°C warmer than observations in the equatorial region. The model SSTs in AO4 simulations level out by the end of the simulations, but there is little sign of post-MJO SST recovery. Compared to observations, the reduction in air-sea fluxes in AO4-FLX improves on the large-scale features of the MJO produced in AO4-CTRL - such as the high bias in precipitation and surface winds, and the exaggerated SST cooling.

The high precipitation bias in model precipitation is evident in LPT tracking shown in Fig. 3.3 – as is the MJO's eastward propagation. The time- and space-evolution of large-scale precipitation is shown for TRMM (top) and UWIN-CM simulations, with colored contours outlining the area over which the mean 3-day precipitation exceeds 15 mm day^{-1}. Colors represent the MJO convective envelope through time. As a 3-day accumulation is required for tracking, the observed track before 25 November 2011 is shown in grey, identifying the observed MJO's initiation area near 60°E and 7°S. The eastward propagation of the MJO in TRMM is smooth, with the precipitating area periodically alternating between the Northern and Southern hemispheres, with a mean eastward propagation speed of 4.76 m s^{-1}. The modeled MJOs are slow compared to observations. The eastward propagation of the MJO in AO4 simulations is clear, at 4.03 m s^{-1} in AO4-FLX, and 3.93 m s^{-1} in AO4-CTRL. In UA4, large-scale precipitation over the IO never ceases (Fig. 3.3b), and the apparent eastward propagation of the MJO centroid (0.72 m s^{-1}) comes from the eastward expansion of the MJO convection between 30 November and 1 December, and not from the propagation of precipitation away from the IO.

Unlike in Savarin and Chen (2022a), all simulations produce trackable large-scale precipi-

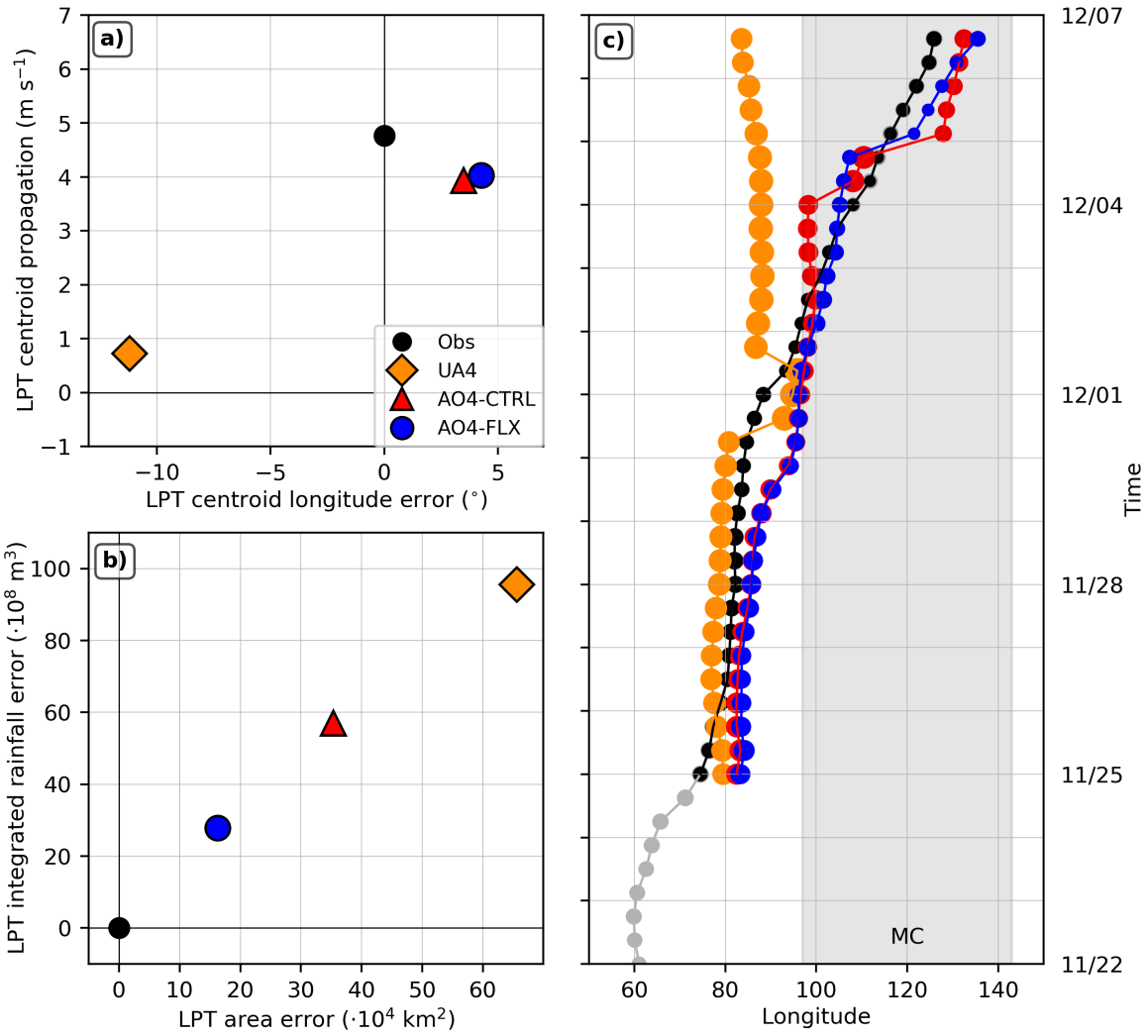

Figure 3.4: Scatterplots of a) LPT centroid propagation speed (m s^{-1}) vs the error in its longitudinal position (°); b) the errors in total rainfall within the LPT (m^3) and its area (km^2); c) the longitude of the LPT centroid in time. The area of circles in c) is proportional to LPT area at a given time.

tation that lasts through the entire simulation, with some characteristics summarized in Fig. 3.4. The LPT centroid in UA4 remains in the IO for the entire duration of the simulation, while AO4 simulations propagate eastward relatively smoothly, producing smaller positional errors. The inclusion of air-sea coupling (UA4 vs. AO4-CTRL) reduces the MJO area and

integrated precipitation by nearly a factor of two, and an additional similar improvement is produced when comparing AO4-CTRL to AO4-FLX (Fig. 3.4b). We see that relatively small changes in the air-sea flux parameterization can reflect significantly on the MJO, both in terms of the amount of produced precipitation, and its eastward propagation. Both AO4 MJO centroids propagate out the IO on 1 December, slightly before the observed MJO does, but the MJO centroid in AO4-CTRL hangs at the western edge of the MC for about three days (with precipitation extending into the IO), while the centroid in AO4-FLX propagates eastward more smoothly, and with fewer discrete jumps (Fig. 3.4c).

Within the MJO, SST cools on average by $\sim$0.5°C, which is well-matched in AO4 simulations (Fig. 3.5). To construct this estimation, we look at time series of SST at each point inside the MJO LPT (Fig. 3.3) over the IO and combine the time series of temperature difference from when a point first enters the LPT (time 0), until the LPT – and the MJO influence - move away. Fig. 3.5 shows the mean (solid), and the 10th and 90th percentiles (bottom and top dashed lines, respectively) of the change in SST as a function of time spent inside the MJO. Based on this, we can estimate that the observed MJO-induced SST cooling after 9 days under an MJO can be as strong as 0.9°C, or as weak as 0.1°C. There are regions where SST increases during active MJO, but they are mainly located on the edges of the MJO convective envelope.

Overall, the modeled distributions match well with the observations in reproducing MJO-induced SST cooling, with stronger SST decrease in AO4-CTRL than in AO4-FLX. At day 9, both the 10th percentile and the mean of the modeled SST cooling agree remarkably well with observations, especially in AO4-FLX. The modeled changes in the top and bottom 10% of the SST changes are more gradual compared to observations, which show both rapid warming and cooling (+/- 0.3°C) within the first day inside the MJO convective envelope. Some of this could be related to the daily resolution of observational data, and to the fact that the observed MJO area is much smaller than in the models, so there are fewer time series to create the distribution from. This can also be inferred because the observed distribution exists for up to 9 days inside the MJO convective envelope, while the modeled distributions

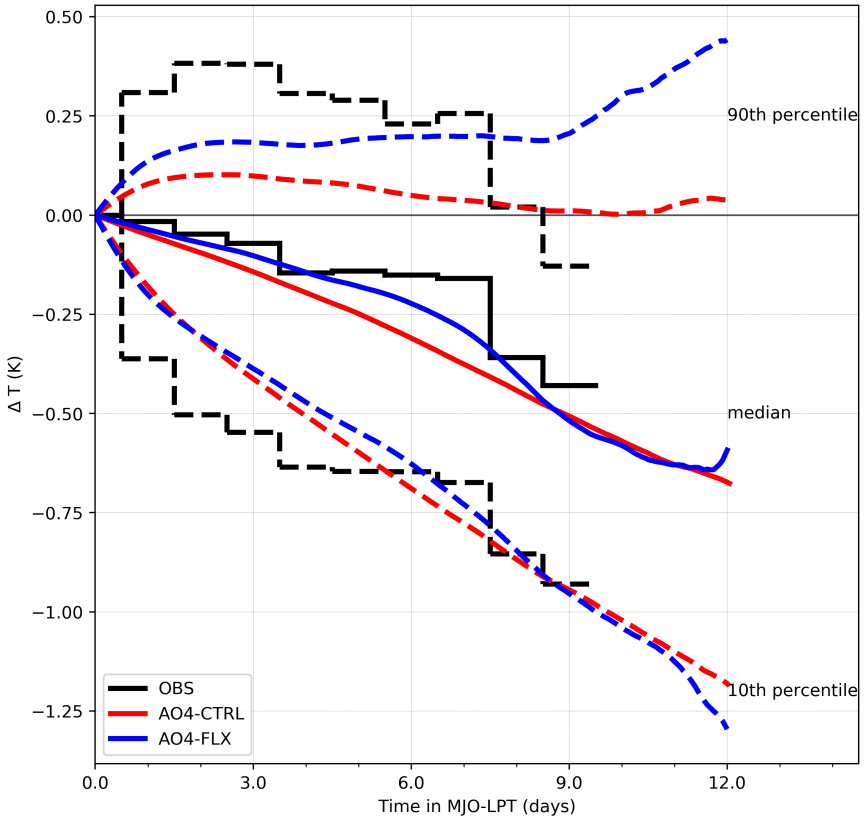

Figure 3.5: The range of MJO-induced SST cooling as a function of time spent inside large-scale tracked precipitation. The solid lines show the median values in for observed SST (black) and AO4-CTRL and AO4-FLX simulations (colors), while the dashed lines denote the 10th and 90th percentiles.

contain locations that remain inside the MJO convective envelope for up to 12 days.

In summary, all UWIN-CM simulations at convection-permitting resolutions produce large-scale equatorial convection and strong surface westerly winds. Only coupled simulations produce significant eastward propagation; the uncoupled simulation constantly produces and reinforces convection over the IO. Between coupled simulations, the eastward propagation is better defined in AO4-FLX, as the amount of precipitation and the size of the MJO convective envelope are less exaggerated. This implies that air-sea interaction provides important insights into the MJO's eastward propagation over the IO. Upper-ocean cooling induced by

the MJO (which is absent in UA4) acts as a push for the MJO's eastward propagation, and a smaller bias in air-sea fluxes (corrected in AO4-FLX) reduces the amount of precipitation and speeds up the MJO's eastward propagation over the IO and into the MC.

3.5 Air-Sea Fluxes, Surface Winds, and Precipitation

The atmosphere and ocean interact through air-sea fluxes of momentum, trace elements such as sea salt, and sensible and latent heat. Of those, SHF and LHF are important sources of heat and moisture for the atmosphere, respectively, and a misrepresentation of their magnitude is partly responsible for the high precipitation bias in UWIN-CM simulations. The AO4-FLX experiment was designed with the awareness that the LHF in UA4 and AO4-CTRL were biased toward high values. Fig. 3.6 shows the distributions of LHF (top) and SHF (bottom) in observations (grey) and model simulations (colored), as a function of the 10-m wind speed. Observations come from R/V Revelle (R in Fig. 3.1), which are available every 10 minutes (grey circles), and the thick black line represents the mean flux value at a given wind speed. To compensate for the model's less frequent output and possible misplacement of features, the model distributions include all points within 1° of R/V Revelle, after which each distribution is normalized by its maximum value. Orange squares show the daily flux values from the OAFlux product at the location R/V Revelle, which are in good agreement with ship observations.

The observed LHF ranges from 20 to 400 W m^{-2}, with a relatively linear increase with surface wind, while the SHF trend is less linear and ranges from -5 to 110 W m^{-2}. The mean air-sea fluxes and their biases compared to R/V Revelle observations are listed in Table 3.1. The mean LHF in UA4 is double that of the observed values at R/V Revelle, with the mean bias of 73.63 W m^{-2}, and the mean of the distribution lying above even the highest observed fluxes for a given wind speed (Fig. 3.6a). With air-sea coupling, the entire SHF and LHF distributions are shifted toward lower values, and the LHF bias is reduced by over 60% in AO4-CTRL, with an additional reduction of over 30% in AO4-FLX. The range of air-sea flux values in AO4-FLX is reduced (we get tighter distributions), but LHF still exhibits a

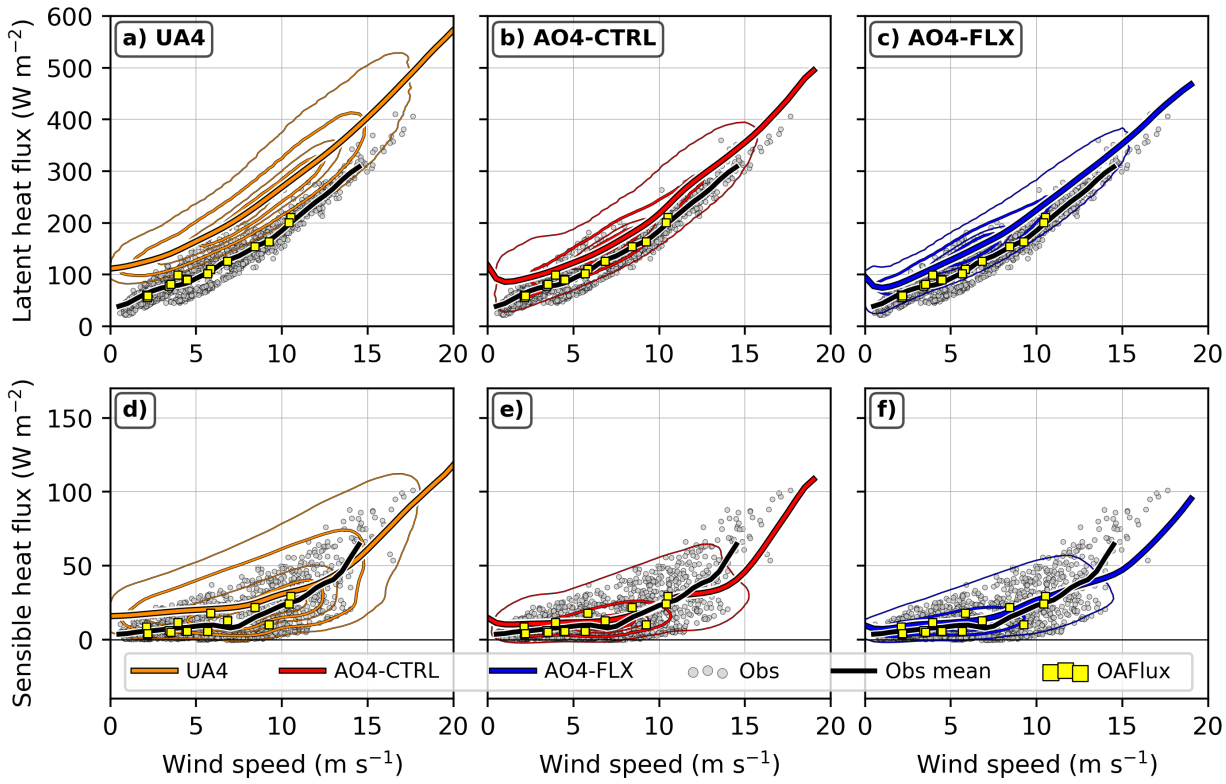

Figure 3.6: Distributions of observed air-sea latent (top) and sensible (bottom) heat flux at R/V Revelle (80.5°E, 0.10°N, grey circles). Model simulated air-sea fluxes (colored contours) come from within 1° of R/V Revelle and are normalized by the highest value in each distribution. The contour levels plotted are at the 1st, 10th, 30th, 50th, and 70th percentiles of the distributions. Yellow squares show the daily OAFlux fluxes at the location of R/V Revelle.

high bias, and the lowest observed fluxes at a given wind speed are not reproduced.

As OAFlux values agree with ship observations, we use the product to compare air-sea flux distributions on a larger scale – over the entire equatorial IO, a region outlined in black in Fig. 3.3, 55-97°E and 10°S-10°N. The SHF and LHF distributions in model and OAFlux are shown in Fig. 3.7, along with the distribution of wind speed over the same region (observations from CCMP). Comparison over the larger region allows us to generalize the

Product	LHF W m^{-2}	LHF bias W m^{-2}	LHF bias (%)	SHF W m^{-2}	SHF bias W m^{-2}	SHF bias (%)
UA4	253.74	128.84	103	30.55	16.45	117
AO4-CTRL	174.92	50.02	40	17.26	3.16	22
AO4-FLX	158.32	33.42	27	15.90	1.80	13
R/V Revelle	124.90	-	-	14.10	-	-

Table 3.1: Mean air-sea heat fluxes and their biases as a function of wind speed compared to measurements from R/V Revelle.

results from R/V Revelle data. The mean values and biases of wind speed, SHF, and LHF distributions over the equatorial IO are recorded in Table 3.2.

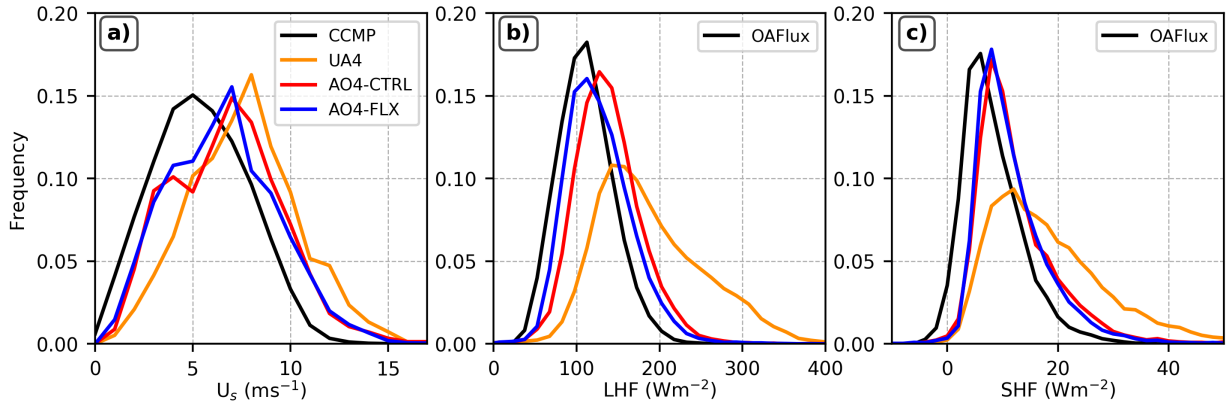

Figure 3.7: Distributions of a) wind speed, b) sensible heat flux, and c) latent heat flux over the equatorial IO. The black line in a) shows the distribution of CCMP surface winds, while the black lines in b) and c) shown the distributions of daily OAFlux air-sea fluxes. Model fluxes have been re-gridded to match the resolution of observations.

The LHF biases at R/V Revelle are higher than over the entire equatorial IO, which is reasonable considering that the ship is located right at the equator and experiences the strongest MJO winds, while the equatorial IO fluxes from OAFlux encompass a significant

Product	U_s	U_s bias	LHF	LHF bias		SHF	SHF bias	
	(m s^{-1})	(m s^{-1})	(W m^{-2})	(W m^{-2})	(%)	(W m^{-2})	(W m^{-2})	(%)
UA4	7.61	2.20	188.71	77.19	69	18.35	10.09	122
AO4-CTRL	6.74	1.33	138.08	26.56	24	12.46	4.20	51
AO4-FLX	6.54	1.13	127.19	15.67	14	11.88	3.62	44
OAFlux			111.52	-	-	8.26	-	-
CCMP	5.41	-						

Table 3.2: Mean values of equatorial IO-averaged wind speed and air-sea flux distributions and their biases (10°S-10°N, 55-97°E).

area not in contact with the MJO convective envelope tracked by LPT (Fig. 3.3). Again, we see the strongest improvement from UA4 to AO4-CTRL (45% in LHF), with an additional smaller reduction in LHF bias in AO4-FLX. The biases in SHF are improved as well, though the SHF magnitude is small to begin with.

The improvements in air-sea flux representation (specifically the LHF) from AO4-CTRL to AO4-FLX are larger than what was expected from a small change to the flux calculation parameterization (Eq. 3.4). The relationship between LHF, surface winds, and precipitation is shown in time series of IO-averaged quantities in Fig. 3.8. In all panels, observations or analysis data are shown in black, and model simulations in color; thick lines show data smoothed using a 24-hour running mean. The reduction in LHF between UA4, AO4-CTRL and AO4-FLX is clear from the beginning of the simulation, while the differences in surface winds and precipitation take some time to develop. This could be related to the upscaling of the change in local air-sea fluxes to the larger basin scale. We see that a reduction in air-sea fluxes results in an overall weakening of surface winds, as well as reduced precipitation over the entire equatorial IO. The impact of LHF on precipitation is relatively straightforward, as reduced LHF means there is less moisture in the atmosphere that is available to precipitate. But the surface winds are affected indirectly, most likely through a CISK-like mechanism,

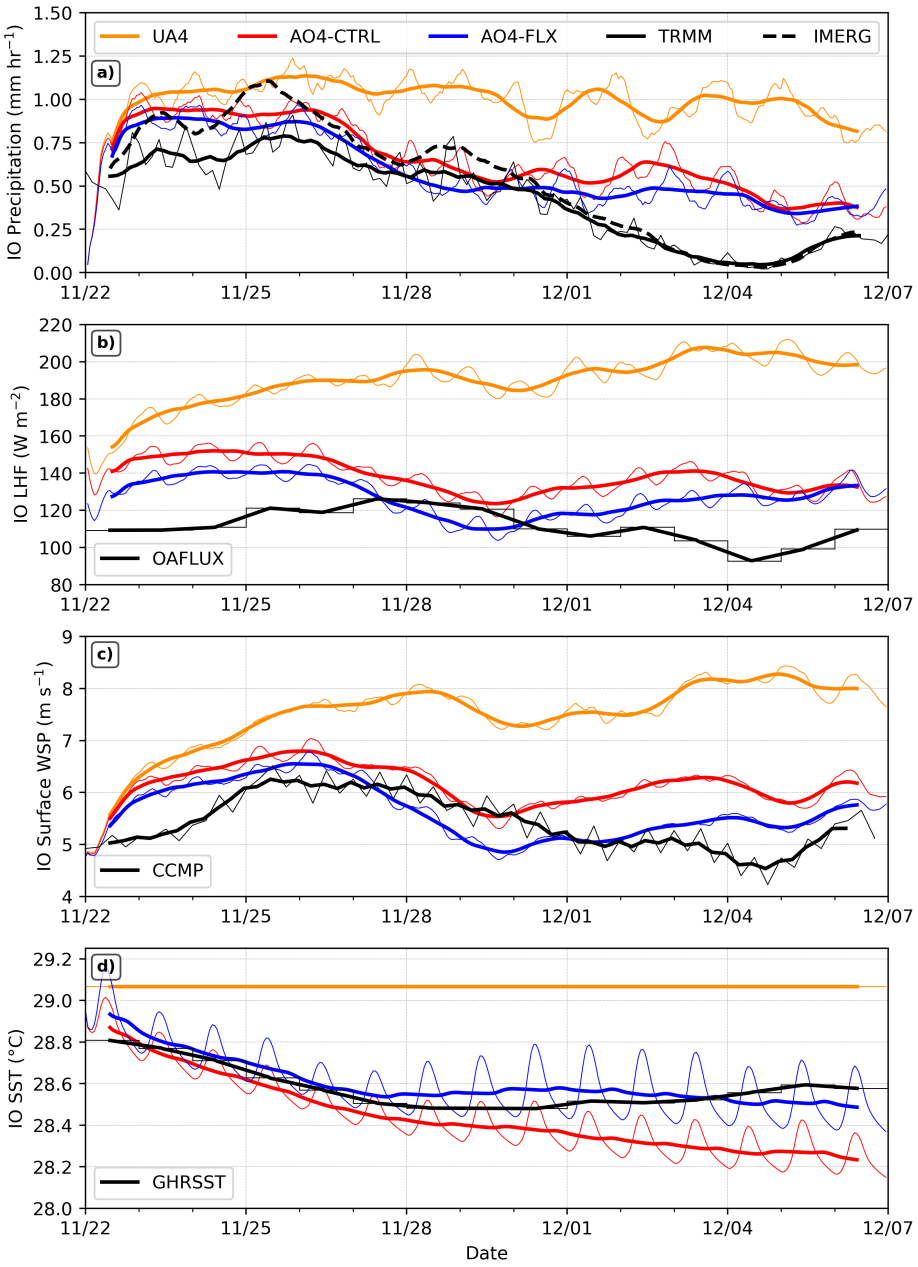

Figure 3.8: Time series of Indian Ocean-averaged a) rain rate (mm hr^{-1}) b) latent heat flux (W m^{-2}), c) surface wind speed (m s^{-1}), and d) SST (°C) in model simulations (color) and observations/analysis (black). Precipitation observations come from TRMM 3B42 (solid) and GPM IMERG (dashed), LHF observations come from OAFlux, surface winds from CCMP, and SST from GHRSST. Thin lines represent data at its native resolution, while thick lines show the 24-hour running mean of the data.

by way of which weaker convection will induce a weaker circulation.

From Fig. 3.8 we can see that the unexpectedly large reduction in LHF (and LHF bias) in AO4-FLX is initially due to the implemented reduction in flux magnitude, but that it is reinforced by weaker surface winds – which will additionally lower air-sea fluxes. However, there are also physical mechanisms that counteract this reinforcement. Specifically, reduced air-sea fluxes and weaker winds lead to less upper-ocean cooling in AO4-FLX compared to AO4-CTRL (Fig. 3.2 k, l), which acts to increase LHF for a given wind speed. We can see evidence of this in the last days of the simulation, when surface winds in AO4 simulations remain distinct (Fig. 3.8b), but LHF magnitudes begin to converge (Fig. 3.8a). This is the result of AO4-FLX SSTs beginning to recover after MJO passage, while the SSTs in AO4-CTRL do not. This mechanism is addressed in more details in the following section.

3.6 Upper Ocean Conditions During and After MJO Passage

The modification to the formulation of air-sea fluxes in the atmosphere portion of UWIN-CM results in an unexpectedly marked difference in SST compared to AO4-CTRL, and the processes behind it are addressed in this section. We focus on the equatorial IO (55°E-97°E, 10°S-10°N; outlined in black in Fig. 3.3), which coincides with the regions of MJO initiation and eastward propagation along the equator, and our convection-permitting domain. Though the model is good at reproducing the MJO-induced SST cooling (Fig. 3.5), the coupled simulations tend to over-cool the IO (Fig. 3.2, right), partly because the modeled MJO persists longer and over a larger area than what was observations show. However, SSTs in AO4-FLX are on average 0.1°C higher than in AO4-CTRL.

This systematic change in SSTs can result from a few different processes, some of which have been explored in the previous section. First, ocean can lose heat through positive SHF and LHF. Second, surface winds apply stress to the ocean surface, which contributes to the mechanical mixing of cooler water toward the surface. Third, cold water can be advected from a different region. And fourth, the ocean surface can cool by precipitation, creating a cool freshwater lens. Additionally, the structure of the ocean mixed layer itself can affect

the change in SST, with effects like the MLD itself (the temperature would be more difficult to change with a deeper mixed layer than a shallower one) and the formation of barrier layers. Since the effect of precipitation is not represented in UWIN-CM, it cannot be the cause for the difference in this case. And though we see a difference in surface winds between AO4-CTRL and AO4-FLX (Figs. 3.7, 3.8), we only see a slight weakening of upper-ocean currents in the latter, which also cannot explain the consistent SST differences. As for the effects of heat loss from the ocean to the atmosphere through SHF, we see in the previous section that the difference in SHF between the simulations is very small, both right at the equator (Fig. 3.6) and throughout the equatorial IO (Fig. 3.7).

The mechanism for SST cooling that we focus on here is related to the ocean forcing by surface winds and air-sea fluxes, their effect on the upper ocean, and consequently, on SST. We know from the previous sections that AO4-CTRL produces stronger surface winds than AO4-FLX, which is an indirect dynamical response to the change in air-sea flux parameterization. Fig. 3.9 shows the relationships among three sets of variable pairs: SST and ocean mixed layer depth (MLD; Fig. 3.9a), SST and surface wind speed (Fig. 3.9b), and surface wind speed and MLD, establishing a relationship among the three quantities. MLD is defined as described in Section 3.3.4. The colored contours show the difference between the normalized joint distributions in AO4-FLX and AO4-CTRL (red means higher frequency in AO4-CTRL), and the black contours outline the AO4-CTRL distributions for reference.

Among each pair of variables, the change from AO4-CTRL to AO4-FLX is seen as a simple shift: higher SSTs are associated with shallower MLD (Fig. 3.9a) and weaker surface winds (Fig. 3.9b), while weaker surface winds are associated with shallower MLD (Fig. 3.9c). Considering these relationships, we can identify a physical mechanism that can explain the differences in SST between AO4 simulations and identify surface winds as the main driver behind MLD and SST changes. Compared to AO4-CTRL, the weaker surface winds in AO4-

FLX force less stress on the ocean surface, contribute to (slightly) slower ocean currents and induce less upper-ocean shear. Reduced shear leads to less mixing between the warm mixed-layer waters and the colder water below, resulting in shallower MLD and less SST

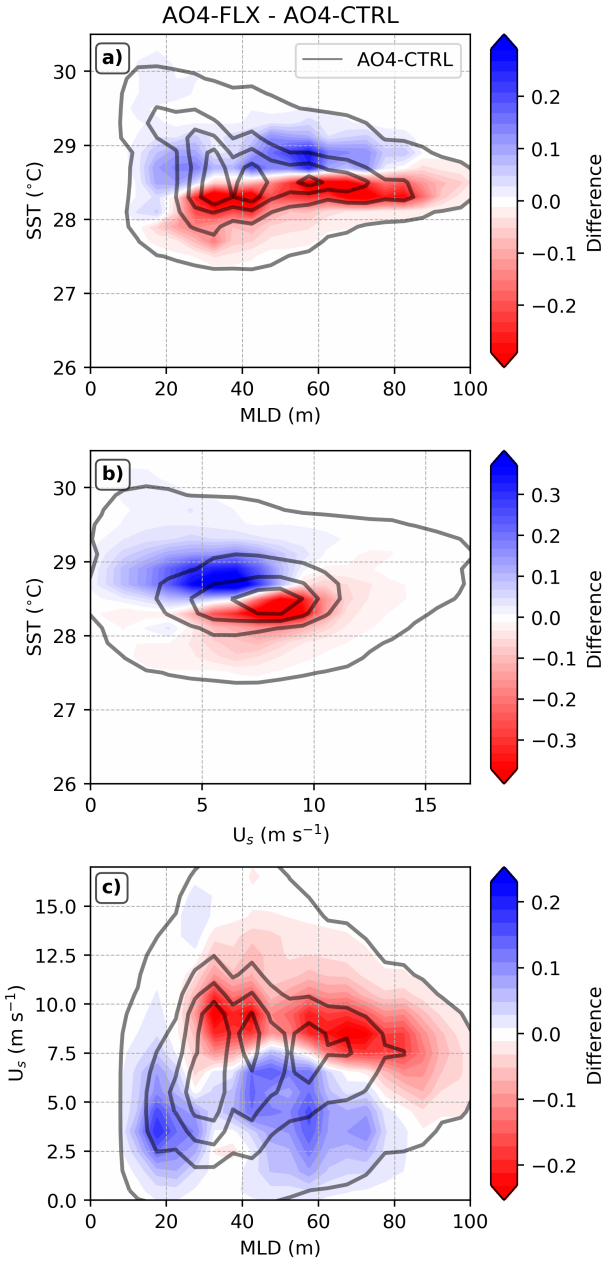

Figure 3.9: Joint probability distribution differences between AO4-FLX and AO4-CTRL for a) SST and MLD; b) surface wind speed and MLD; and c) SST and surface wind speed. The black contours in each panel indicate the 1st, 25th, 50th, and 75th percentiles of the joint distribution in AO4-CTRL for comparison.

cooling. With a shallower mixed layer, suppressed conditions after MJO passage (which include weak winds and clear skies) can work to efficiently recover the SSTs back toward a pre-MJO state. Conversely, stronger surface winds (in AO4-CTRL) induce more cold water mixing into the surface ocean, deepening the MLD, cooling the SST further, and inhibiting its recovery.

To further examine the model simulated upper ocean conditions during and after MJO passage, we compare the model simulations with DYNAMO and RAMA mooring observations at three locations: 79°E and 0°N, 80.5°E and 0°N, and 79°E and 1.5°S (Figs. 13.10-3.12). During the convectively active MJO period from 22-30 November, observations show near-surface (∼10 m) ocean temperature cooling, and a deepening of the ocean mixed layer, especially at the equator. Both the temperature and mixed layer depth are relatively well simulated by the coupled model. Strong surface winds are responsible for upper-ocean mixing.

From 1-6 December, after MJO passage, the observed mixed layer shoals and near-surface temperatures begin to increase due to the formation an oceanic barrier layer driven by reduced salinity (fresh water) near the surface (Figs. 3.10 and 3.11). Both AO4 simulations deviate from observations, missing the near-surface fresh water, the barrier layer formation, and the consequent shoaling of the mixed layer and near-surface ocean temperature (and SST) increase. Instead, the simulated mixed layer after MJO passage remains deep, any surface warming is distributed through a thicker layer, and near-surface ocean temperatures remain steady in both simulations instead of recovering. Fresh water input from precipitation is not coupled to ocean salinity in the current model simulations. However, the ∼20 m deep layer of fresh water in the observations after 30 November (Fig. 3.10) and 2 December (Fig. 3.11) are not associated with local precipitation. Instead, they occur during the post-MJO phase, while there is no precipitation. The observed fresh water may be a result of advection according to the satellite surface salinity data (not shown).

Conditions are different south of the equator, where the upper ocean is generally fresher. At the mooring located at 79°E, 1.5°S, first there is a deepening of the mixed layer (and

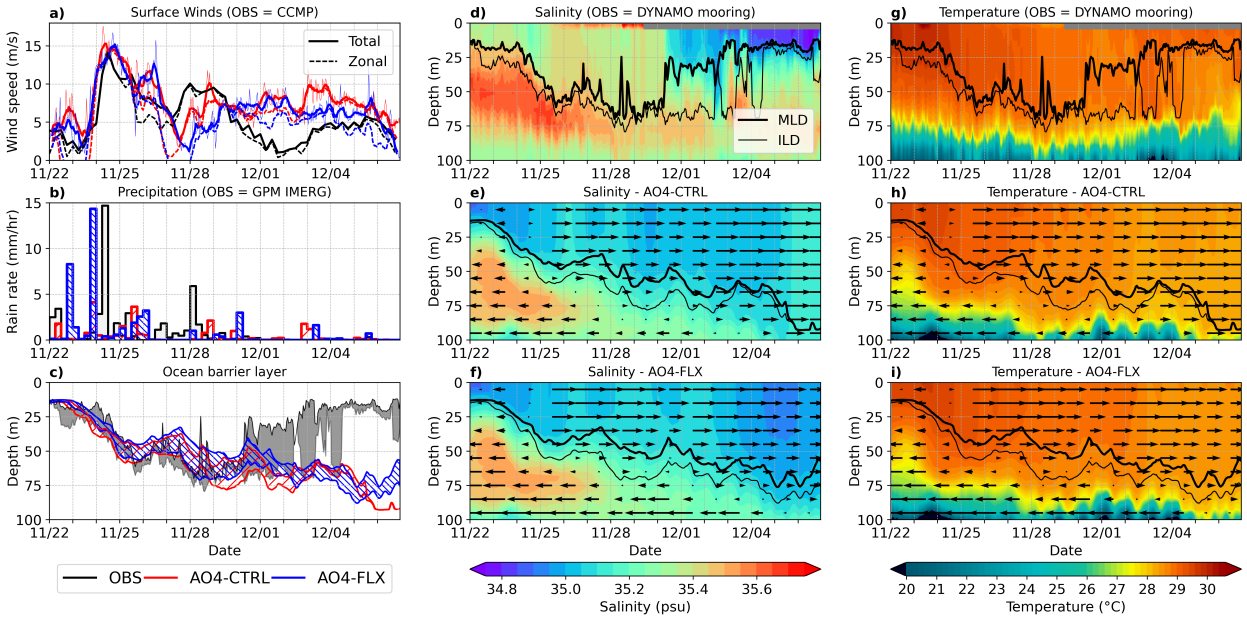

Figure 3.10: Time series of observed and simulated surface and upper-ocean properties at the DYNAMO mooring located at 79°E, 0°N. a) Surface wind speed (m s^{-1}); b) precipitation (mm hr^{-1}); c) upper-ocean barrier layer; d-f) upper-ocean salinity (psu) and g-i) upper ocean temperature (°C) from observations (top), model simulations of AO4-CTRL (middle) and AO4-FLX (bottom) overlaid with zonal current (vectors). In the upper-ocean profiles (d-i), thick black lines indicate the mixed layer depth (MLD), and thin black lines indicate the isothermal layer depth (ILD), which are the bounding depths of the barrier layer (c). Note that the surface observations at the mooring were not available during this period, so the surface winds (a) are obtained from the CCMP product, and the precipitation (b) is from high-resolution GPM-IMERG.

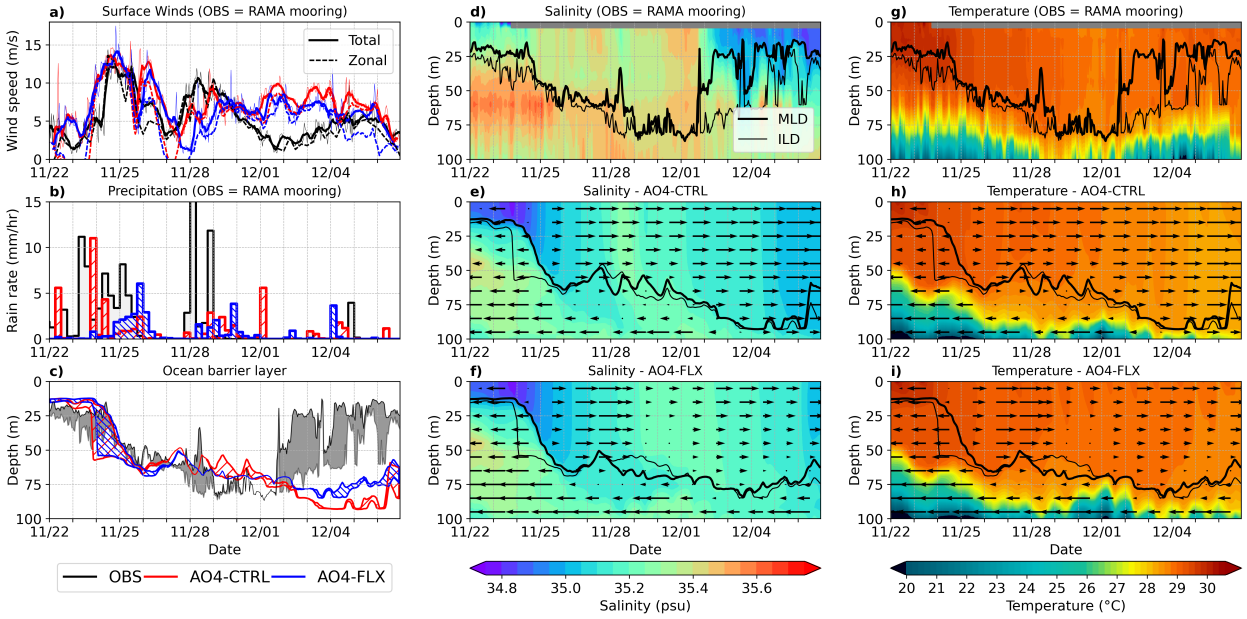

Figure 3.11: Same as Fig. 3.10, except for the RAMA mooring located at 80.5°E, 0°N. The observed surface wind and precipitation measurements were recorded by instruments on the RAMA mooring.

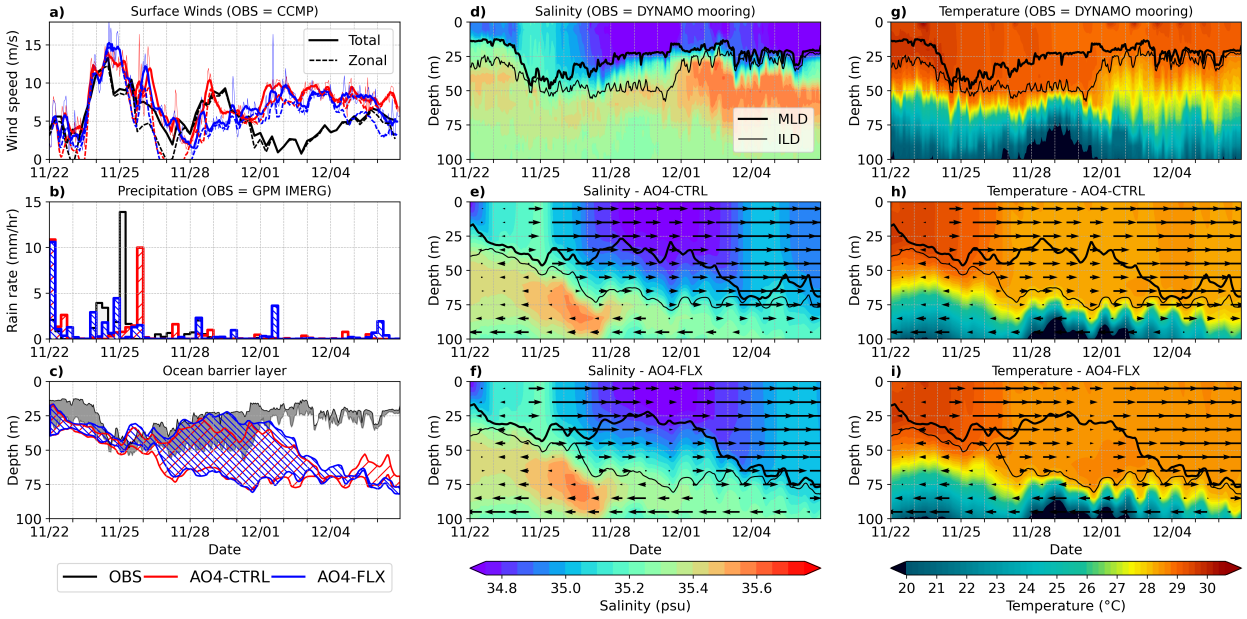

Figure 3.12: Same as Fig. 3.10, except for the mooring located at 79°E, 1.5°S.

SST cooling) that lasts for ∼4 days, then a very thick barrier layer forms due to strong near-surface freshening (Fig. 3.12). These features are relatively well simulated. But the modeled surface winds post-MJO remain biased high, the MLD deepens, and the near-surface ocean temperature continues to decrease beyond what is observed.

The overall evolution of SST and MLD from both observations and model simulations are summarized in Fig. 3.13. At all three locations, the observation and model simulations track relatively close during the active MJO phase, when the strong surface-wind-induced mixing is dominant (22-30 November). However, they differ significantly during the post-MJO phase from 1-6 December. In all cases, AO4-FLX improves on the AO4-CTRL model simulation and reduces model SST bias by ∼50% and MLD bias by ∼16% (Fig. 3.13).

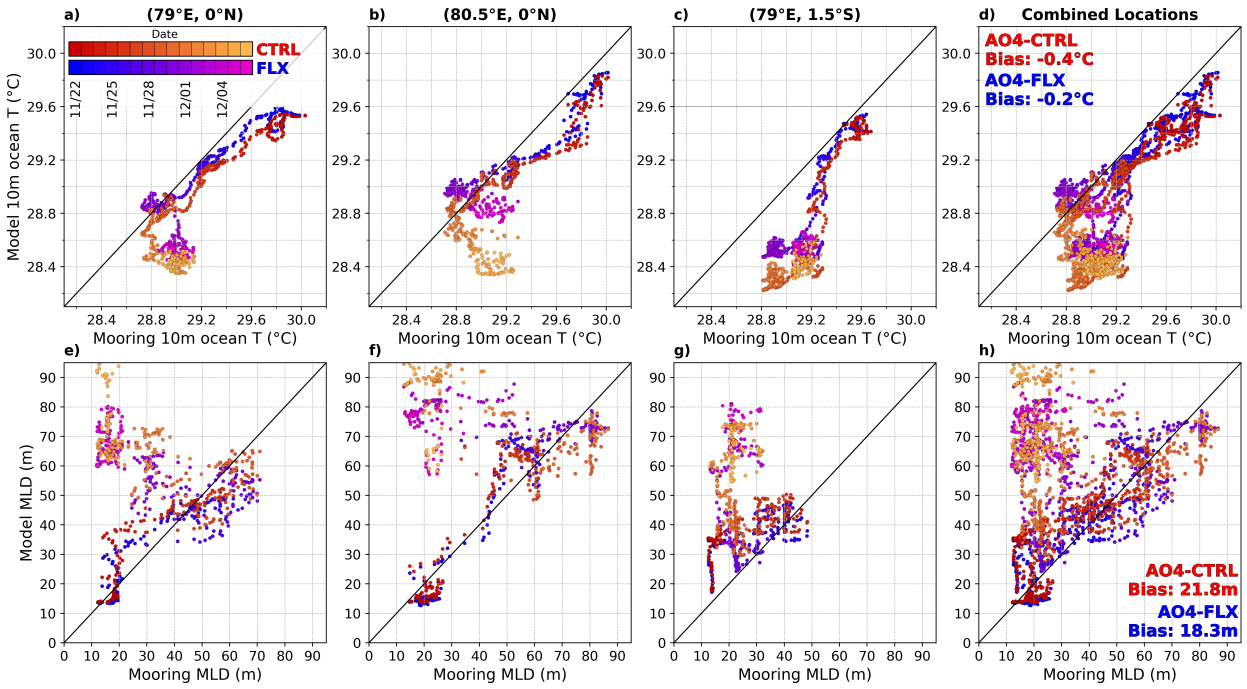

Figure 3.13: Comparison of observed and modeled 10-m ocean temperatures (top) and mixed layer depths (bottom) at three mooring locations: a, e) 79°E, 0°N; b, f) 80.5°E, 0°N, c, g) 79°E, 1.5°S. The rightmost column (d, h) shows the scatterplot of all three locations combined. The color change indicates time progression, with the red and blue colors for the AO4-CTRL and AO4-FLX simulations, respectively.

3.7 Summary and Conclusions

This study investigates impacts of atmosphere-ocean coupling on MJO precipitation and eastward propagation, and upper ocean conditions during and after MJO passage. Three model simulations of the MJO event observed during DYNAMO in 2011 at convection-permitting (4 km) resolution with uncoupled atmosphere only and coupled atmosphere-ocean model are conducted to explore pathways for improving MJO prediction. A revised air-sea flux algorithm is implemented to further improve the coupled model simulation. The combination of ship and mooring observations over the central IO during the DYNAMO field campaign, satellite-derived precipitation and air-sea fluxes, and the high-resolution model data provide a unique opportunity to examine how air-sea interaction processes are represented in numerical models, and how they affect precipitation.

This study exposes three main findings:

- Coupled atmosphere-ocean model reproduces the MJO eastward propagation whereas uncoupled atmospheric-only model fails.

- Upper-ocean cooling induced by the MJO is essential in reducing excessive and prolonged precipitation over the Indian Ocean and aiding in MJO's eastward propagation.

- Improved air-sea flux algorithm reduces model biases in rainfall, surface winds, air-sea fluxes, as well as the bias in upper ocean temperature, all of which improve the MJO prediction.

Atmosphere-ocean interaction is essential for the MJO's eastward propagation from the IO, as it creates local conditions unfavorable for sustained large-scale convection. In the coupled simulations (AO4-CTRL and AO4-FLX), strong surface winds associated with the MJO promote evaporation and provide fuel for precipitation, but they also cool the upper ocean, both through heat loss to the atmosphere, and cold upwelling due to enhanced upper-ocean mixing. Cooler SSTs then suppress further evaporation and limiting moisture

supply from the underlying ocean, reducing local precipitation; the MJO convection shifts eastward over warmer SSTs, where moisture is more readily available. The case is similar in both coupled simulations, with the main difference being that SST cooling, and subsequent warming are better captured in AO4-FLX, as is the MJO's eastward propagation. In the atmosphere-only simulation, a positive feedback is established between the SST, winds, and precipitation. Warm SSTs are conducive to strong evaporation, providing an efficient moisture source for precipitation. But unlike in the coupled simulations, the atmospheric forcing does not affect SST, and, together with strengthening surface winds, evaporation remains high, as does the amount of precipitation. With a convenient endless moisture source, precipitation is ubiquitous, and we see no eastward propagation of large-scale precipitation or surface westerly winds.

Atmosphere-ocean interaction is essential for the MJO's eastward propagation from the IO, as it creates local conditions unfavorable for sustained large-scale convection. In the coupled simulations (AO4-CTRL and AO4-FLX), strong surface winds associated with the MJO promote evaporation and provide fuel for precipitation, but they also cool the upper ocean, both through heat loss to the atmosphere, and cold upwelling due to enhanced upper-ocean mixing. Cooler SSTs then suppress further evaporation and limiting moisture supply from the underlying ocean, reducing local precipitation; the MJO convection shifts eastward over warmer SSTs, where moisture is more readily available. The case is similar in both coupled simulations, with the main difference being that SST cooling, and subsequent warming are better captured in AO4-FLX, as is the MJO's eastward propagation. In the atmosphere-only simulation, a positive feedback is established between the SST, winds, and precipitation. Warm SSTs are conducive to strong evaporation, providing an efficient moisture source for precipitation. But unlike in the coupled simulations, the atmospheric forcing does not affect SST, and, together with strengthening surface winds, evaporation remains high, as does the amount of precipitation. With a convenient endless moisture source, precipitation is ubiquitous, and we see no eastward propagation of large-scale precipitation or surface westerly winds.

These results are supported by previous studies that have been able to accurately reproduce an MJO event only when either using a coupled atmosphere-ocean model, or updating SSTs with observed values (Hung et al., 2013; Miura et al., 2009; Zhang et al., 2006), and very few that were able to reproduce an event when using fixed SSTs (Holloway et al., 2013, 2015). However, Drushka et al. (2012) found that during active MJO, the shear-induced cold upwelling during active MJO conditions represents half of the observed temperature change in the mixed layer, which underlines the importance of dynamical ocean models in lieu of using constant-depth slab ocean models.

Despite these improvements, the coupled simulations still show difficulty representing the convectively suppressed conditions after the MJO passage to the extent seen in observations. There is still excessive precipitation over the IO (Fig. 3.2), part of which could be linked to the models' slightly high-bias in surface winds and air-sea fluxes (especially the LHF) injecting too much moisture into the atmosphere (Fig. 3.8). We also note the difficulties the coupled simulations have in representing the recovering SST through the inadequate formation of barrier layers after MJO passage, in the second half of the simulations. While MJO convection is over the IO, strong winds induce high heat fluxes at the surface, and with entrainment cooling from mixed layer deepening, both factors act to reduce SST by 0.7°C on average – this agrees with previous observational studies (e.g., Lau and Sui, 1997; Maloney and Kiehl, 2002). After active MJO convection passes observed winds weaken, leading to a reduction in air-sea fluxes and upper-ocean mixing, and with increased insolation, we see the formation of oceanic barrier layers near the equator (mooring observations in Figs. 3.10, 3.11). Barrier layer formation rapidly shoals the mixed layer, and as surface fluxes are now distributed over a thinner layer, it makes it easier for SSTs to recover. But in coupled model simulations, convection persists a bit longer, and surface winds to not weaken enough to allow for barrier layer formation – thus, any reduction in surface fluxes and increased insolation keep being distributed through a very thick layer, making post-MJO SST recovery slower and weaker than observed.

It has been noted that air-sea interaction is more important for some MJO events than it

is for others (Fu et al., 2015; Wang et al., 2015), and that the importance of air-sea interaction depends on the underlying ocean (Drushka et al., 2014; Fu et al., 2015; Moum et al., 2016). For example, if an MJO is passing over an ocean with a deep, warm mixed layer, the surface fluxes and wind stress would be distributed through a thicker layer, and any changes to SST would be small compared to an MJO passing over a shallower mixed layer (Fu et al., 2015; Marshall et al., 2008). While most current studies focus on the role of SST in providing an environment for moisture-convergence to the east of the MJO convection, not many studies have studied the processes that lead to the relatively rapid SST recovery after MJO passage, and we have identified the lack of barrier layer formation as one of the culprits in the UWIN-CM simulations. Due to the demonstrated importance of upper-ocean mixing and air-sea fluxes, our results indicate that upper ocean processes and their two-way interaction with the MJO over the Indian Ocean should be examined closely by further studies.

Chapter 4

LAND-LOCKED CONVECTION AS A BARRIER TO MJO PROPAGATION ACROSS THE MARITIME CONTINENT

Savarin, A., & Chen, S. S. (2022). Land-Locked Convection as a Barrier to MJO Propagation across the Maritime Continent. Journal of Advances in Modeling Earth Systems, in review.

4.1 Abstract

Large-scale convection associated with the Madden-Julian Oscillation (MJO) initiates over the Indian Ocean and propagates eastward across the Maritime Continent (MC). Over the MC, MJO-related convection is generally weakened due to complex interactions between the large-scale MJO and the MC landmass. The MC barrier effect is responsible for the dissipation of 40-50% of observed MJO events, which is often exaggerated in weather and climate models. We examine how MJO propagation over the MC is affected by two aspects of the MC - its land-sea contrast and its terrain.

To isolate the effects of mountains and land-sea contrast on MJO propagation, we conduct three high-resolution coupled atmosphere-ocean model experiments: 1) a control simulation (CTRL) of the 2011 November-December MJO event, 2) a run without MC mountains (FLAT), and 3) a no-land simulation (WATER) in which the MC islands are replaced with 50 m deep ocean. CTRL captures the general properties of the diurnal cycle of precipitation and MJO propagation across the MC. The WATER simulation produces a more intense and more smoothly propagating MJO convection compared with that of CTRL. In contrast, the FLAT simulation produces much more convection and precipitation over land than CTRL, resulting in a stronger barrier effect on MJO propagation. The land-sea contrast induced stationary land-locked convection weakens the convective organization of the propagating MJO. The land locked convective systems over land in FLAT are more intense, grow larger, and last longer than those in CTRL, and this drives to be more detrimental to the MJO's propagation across the MC than the mountains that are present in CTRL.

4.2 Introduction

The Maritime Continent (MC) is a unique region comprising thousands of islands in the tropical Pacific warm pool with a complex distribution of topography and terrain. It is a crucible for interactions between many different phenomena including many scales of atmospheric and oceanic variability, from decadal (El Niño - Southern Oscillation), to seasonal (monsoons), intraseasonal (the Madden-Julian Oscillation (MJO), Madden and Julian, 1971, 1972), and some of the strongest diurnal cycles in the world (Moron et al., 2015). Kikuchi and Wang (2008) classify the DC over the MC into a coastal regime under which systems of land- and sea-breezes drive precipitation location and intensity, modified by the background circulation, orography, and coastline orientation (Abbs and Physick, 1992). Differential solar heating during the day induces a sea breeze circulation around islands and precipitation begins to form on the coast, then propagate inland from noon to evening; precipitation over the neighboring oceans is suppressed (Miller et al., 2003). At night and in the early morning, the land breeze, which is associated with weaker precipitation, propagates offshore and suppresses precipitation on the coast (Chen and Jr, 1997).

Numerical models often underestimate the precipitation in this region, in part due to a poor representation of the DC of precipitation around the islands (Neale and Slingo, 2003). Increasing the model resolution reduces the dry bias over the MC and has been linked to better-resolved surface conditions and land-sea contrast (Schiemann et al., 2014), but models are still too quick to trigger precipitation over land and they exaggerate the amplitude of the DC over land compared to what is simulated over water (Lee and Wang, 2021; Li et al., 2017; Love et al., 2011).

The MC impedes the eastward propagation of the MJO from the Indian Ocean toward the western Pacific - its barrier effect is responsible for weakening most MJO-related convective events that cross the region, and completely dissipating 45-50% of them (Kerns and Chen, 2020; Zhang and Ling, 2017). Some studies focus on the physical effect related to the blocking of flow by the topography (e.g., Wu and Hsu, 2009) and its direct consequences, such as

reduced air-sea fluxes over the islands compared to the surrounding ocean (Sobel et al., 2010; Birch et al., 2016). Other studies focus on dynamical barriers to MJO propagation, such as the westward propagation of dry air that meets the MJO over the MC (DeMott et al., 2018; Feng et al., 2015), the Warm Pool Dipole (Zhang and Han, 2020), and recently, the DC has been identified as an important contributor (e.g., Hagos et al., 2016; Ling et al., 2019a). The MC barrier effect is exaggerated in most general circulation models (Ling et al., 2019b), leading to a prediction barrier to the MJO. As one of the largest sources of tropical intraseasonal predictability, the MJO's downstream influences cannot be accurately resolved without capturing its propagation (or dissipation) over the MC.

The active phase of the MJO over the MC is characterized by strong westerly surface winds, which act to increase low-level convergence, and an increased moisture supply (Lu et al., 2019). Rauniyar and Walsh (2011) and (Oh et al., 2012) found that during the active phase of the MJO precipitation over water is increased, but precipitation over land is reduced, and the timing of peak precipitation is delayed. The DC in deep convective clouds was found to be amplified during the active phase of the MJO over both land and water (Tian et al., 2006), but Peatman et al. (2014) show that over the islands of the MC, outgoing longwave radiation is no longer a good proxy for precipitation. Peatman et al. (2014) and Sakaeda et al. (2017) also note that the strongest DC is seen under the convectively suppressed conditions before the arrival of the active precipitation, when the skies are most cloud-free. In addition to the MJO's influence on the MC surface winds, moisture, and amplitude of the DC, Virts et al. (2013) also show that active MJO conditions over the MC suppress lightning activity over the islands, indicating weaker convective systems as compared to non-MJO conditions.

The influence of the DC on MJO propagation is more difficult to infer, but land convection is frequently identified as the main culprit in explaining the MC barrier effect related to the DC. Ling et al. (2019a) find that one factor that separates crossing MJO events from those that dissipate is a strong increase in the DC ahead of precipitation (as described by Peatman et al., 2014). This increases soil moisture ahead of the MJO and damps the land DC during active MJO - more so for crossing MJO-related convective events than the ones that dissipate.

Zhang and Ling (2017) attribute the barrier effect to the inhibition of convective development over water. The MC barrier effect seems to be strengthened either when precipitation over land is anomalously strong, or when precipitation over water is anomalously weak - or both.

Most other studies focusing on the MC barrier effect rely on modeling, where parameters are changed, and their effects examined. The observations of an enhanced DC of precipitation ahead of the active MJO are reproduced in cloud-resolving simulations, while topography plays a role in determining where precipitation develops and how it is distributed among the islands (Wei et al., 2020). Inness and Slingo (2006) find that at low resolution, topography as a physical barrier is more important than the presence of islands themselves. But at higher resolution, many studies that modify the DC in one way or another find that weakening the diurnal cycle over land leads to a weaker barrier to MJO propagation (e.g., Hagos et al., 2016; Oh et al., 2012; Tan et al., 2022; Zhou et al., 2021a).

Though some studies have already been performed with terrain modifications similar to the ones in our study (e.g., Tan et al., 2022; Zhou et al., 2021a), we go a step further by separating the effects of MC topography from the effects of its DC and land-sea contrast and identifying the physical processes through which they impact MJO propagation. The modeling configuration, the MJO tracking, and our unique way of analyzing the DC of precipitation are described in Section 4.3. Section 4.4 focuses on applying the methods to 20 years of precipitation data to establish baseline differences in the DC of precipitation between MJO and non-MJO environments. Section 4.5 addresses the general MJO characteristics, while Section 4.6 describes the DC differences between the model simulations and observations. In Section 4.7, we show that enhanced stationary land locked convection strongly contributes to the weakening of the MJO over the MC. The results are summarized in Section 4.8.

4.3 Methods and Data

4.3.1 Model Configuration and Simulations

The atmosphere-ocean coupled model used in this study is the Unified Wave Interface - Coupled Model (UWIN-CM) (Chen et al., 2013; Chen and Curcic, 2016). All simulations use the configuration that was described in Savarin and Chen (2022b) which includes convection-permitting resolution, atmosphere-ocean coupling, and a modified air-sea flux parameterization that yields a good simulation of the observed MJO event. Simulations are initialized at 00Z on 22 November 2011 and integrated in time for 15 days (360 hours), ending on 7 December 2011.

Briefly, the simulations in this study use the Weather Research and Forecasting (WRF) model v3.6.1 with the Advanced Research (ARW) dynamical core (Skamarock et al., 2008) for the atmosphere component, and the Hybrid Coordinate Ocean Model (HYCOM) v2.2.99 for the ocean (Metzger et al., 2014). The simulated region encompasses the Indian Ocean (IO) and Maritime Continent (MC) with three nested domains of 36-, 12-, and 4 km resolution (Fig. 4.1a); the outer domains use the Tiedtke convective parameterization (Zhang et al., 2011) and the 4-km domain does not use a convective parameterization. The HYCOM grid spacing is a uniform 0.08°. Initial and boundary conditions for the simulations come from the European Centre for Medium-Range Weather Forecast (ECMWF) operational forecast fields for the atmosphere (from CR37R2) and daily mean HYCOM global analysis for the ocean (Cummings, 2005; Cummings and Smedstad, 2013). Similar coupled model configurations have been successfully used to model the MJO (e.g., Wang et al., 2021).

The control simulation (CTRL) has real topography over the MC and is configured identically to AO4-FLX in Savarin and Chen (2022b). We then use the same initial and boundary conditions for two idealized simulations in which we modify topography and bathymetry over the MC to differing degrees. In the FLAT experiment, the MC topography is flattened to a uniform 10 m elevation, and the land-use category for the flattened terrain is changed to evergreen broadleaf forest (Fig. 4.1b). Using the *metgrid* program provided by the WRF pre-

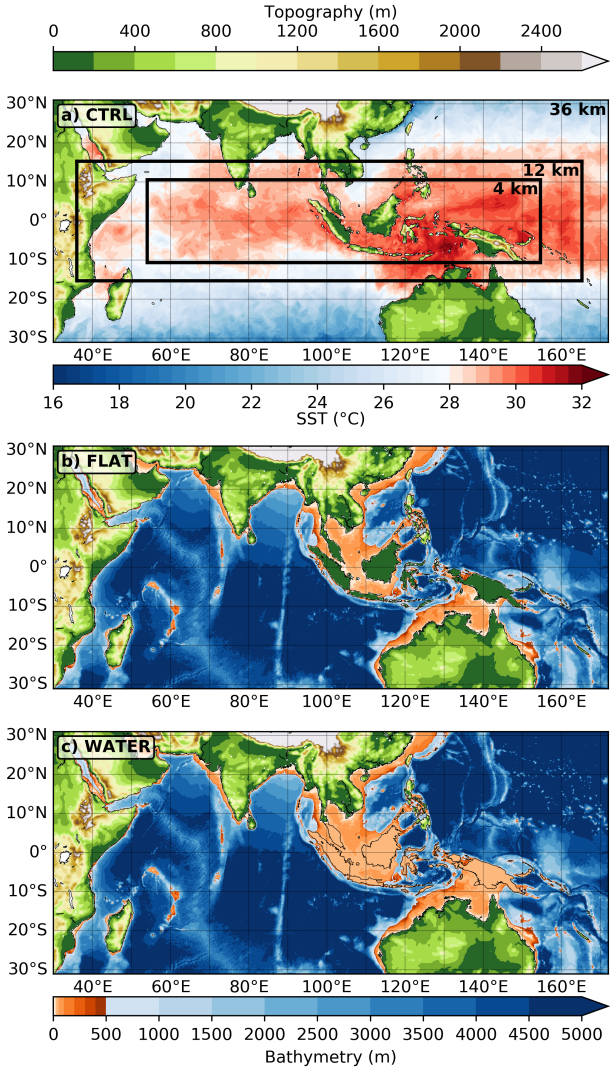

Figure 4.1: Domain configuration and relief in model simulations. a) CTRL topography (m) and initial time SST (°C); b) FLAT topography and bathymetry (m); and c) WATER topography and bathymetry (m). Black rectangles in a) show the boundaries of the nested domains in the atmosphere.

processing system (WPS), atmospheric initial conditions are extended to the surface where topography has been modified, and the ocean initial conditions remain unchanged. In the WATER experiment, MC land is converted to a 50 m deep ocean (Fig. 4.1c). The atmospheric initial conditions are the same as in the FLAT simulation, but the newly created ocean has no currents, while the temperature and salinity fields are interpolated from the nearby ocean and smoothed - thus the ocean temperatures, salinities, and SSTs near the MC are smoother than in the CTRL and FLAT simulations.

4.3.2 Data

Several observational datasets are used in evaluating the model simulations' performance and exploring the physical processes associated with the MJO and the MC. For precipitation, we use the Integrated Multi-satellitE Retrievals for GPM (IMERG) satellite precipitation estimates (V06B; Huffman et al., 2019), which are available at half-hourly intervals at a spatial resolution of 0.1°. 20 years of data (June 2000 - June 2020) are used for MJO tracking and climatology, but when comparing with model simulations, only the 15 days from November 22 - December 7 are considered. In addition to precipitation, we also make use of the Cross-Calibrated Multi-Platform (CCMP) gridded surface vector winds (V2.0; Atlas et al., 2011), which are available 6-hourly at 0.25° spatial resolution. To create a distance-from-coastline reference framework for our analysis of the DC over the MC, we use the ETOPO1 dataset, a global relief dataset at a spatial resolution of 1 arc minute (NOAA National Geophysical Data Center, 2009).

4.3.3 Large-scale Precipitation Tracking of the MJO

The large-scale precipitation tracking algorithm (LPT, (Kerns and Chen, 2016, 2020)) is used to track the MJO-associated precipitation in the IMERG dataset. The algorithm tracks a spatially smoothed 3-day precipitation accumulation that exceeds a chosen threshold over an area larger than $3\text{x}10^5$ km^2. Kerns and Chen (2020) use a 12 mm precipitation accumulation threshold on 20 years (1998-2018) of TRMM 3B42 data, which identifies 215 MJO

events. Before the application of the algorithm to the IMERG dataset, the precipitation data is conservatively re-gridded to 0.25° spatial and 3-hourly temporal resolution to match that of TRMM 3B42. After the LPT algorithm is applied to the IMERG dataset, additional constraints are used to separate MJO events from other large-scale systems, such as a minimum duration of 7 days, and consistent eastward propagation. In the IMERG dataset, the November-December 2011 MJO event remains cohesive and propagates through the MC up to a precipitation threshold of 22 mm. When model simulations are compared to observations, a threshold of 17 mm is used instead of 12 mm to highlight differences between simulations, because the model tends to overproduce precipitation (see Savarin and Chen, 2022b). At the lower thresholds, MJO-associated precipitation can be seen propagating over the MC, but it tends to present as a series of discrete longitude jumps, as the tracking algorithm attempts to connect distinct areas of precipitation with little overlap.

4.3.4 Diurnal Cycle Analysis

We analyze the diurnal cycle (DC) relative to its distance from coastline, which can clearly show us the cycling between land and sea breezes in the MC. The method used is illustrated in Fig. 4.2. We use the 1-arc-minute global relief model dataset, ETOPO1 (Amante and Eakins, 2009) to define a land mask (where global relief is above sea level) and remove islands and bodies of water smaller than 400 km^2 - the modified land mask is shown in Fig. 4.2a. Then the Haversine formula is used to calculate great-circle distances from each point to every other point on the globe, and for each point, the distance to its nearest coastline is chosen (Fig. 4.2a). Negative distances denote inland areas, and positive distances denote areas offshore. In this study, we focus our attention to the western MC (90-120°E, 10°S-10°N), and only data from this region are considered whenever the diurnal cycle is analyzed. The number of points in each 25-km distance bin within is MC region is shown in Fig. 4.2b using a spatial resolution of 0.1° to match the GPM IMERG precipitation dataset.

To construct diurnal cycle composites, precipitation observations are first converted to local solar time (LST), which only depends on longitude, and is rounded to the nearest hour.

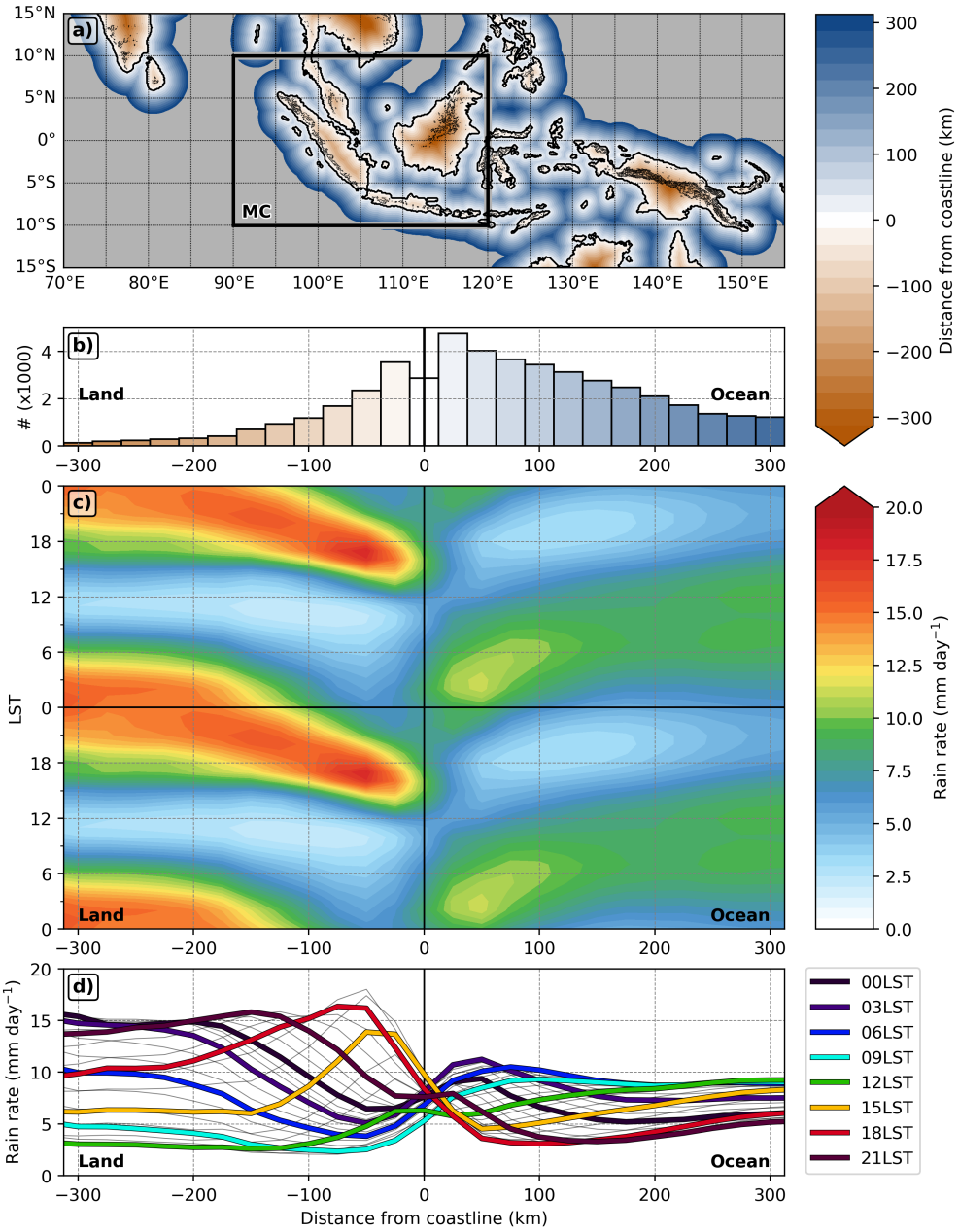

Figure 4.2: Illustration of DC analysis. a) Distance from coastline over the MC (km, negative distances are over land), with the outlined MC area where the DC is analyzed; b) number of points in each 25-km distance bin inside the MC box; c) distance from coastline Hovmöller composite of the 2000-2020 IMERG rain rate DC (mm day^{-1}), repeated twice; d) quantitative composite of the IMERG rain rate DC (mm day^{-1}), with color representing LST.

The LST offsets inside the MC box range from UTC+6 and 90°E to UTC+8 at 120°E. Then precipitation data is binned into 25-km bins for the entire data record and averaged for every LST hour. The resulting distance-from-coastline Hovmöller diagram is shown in Fig. 4.2c for 20 years (June 2000 - June 2020) of IMERG data, and the diurnal cycle is repeated twice for completeness. The analysis can be simplified into a more quantitative line diagram in Fig. 4.2d, in which lines represent the amount of precipitation with distance from coastline, and LST indicated by line color. Displaying the DC in this manner clearly shows the cycling of precipitation between land and ocean (the alternation between land- and sea-breeze) and adds a spatial component to our analysis.

The method described here can be applied to any field, scalar or vector, regardless of whether it is gridded or not. With the additional calculation of bearing based on the Haversine formula, we can obtain the direction from any point to its nearest coastline. This enables us to project vector fields such as surface winds to their across- and along-coastline components in connection with trigonometric functions.

4.4 Diurnal Cycle of Precipitation in MJO and non-MJO Environments

We start by examining the impact of the MJO on the DC of precipitation over the MC in a climatological sense. LPT tracking is used to separate the MC area (outlined in 4.2a) into two categories: active MJO regions directly inside the convective envelope, and the inactive MJO regions outside the convective envelope and its 5° filtering radius. The areas inside the 5° filtering radius but outside the MJO convective envelope are not considered for this analysis. The DC composited for each category is shown in Fig. 4.3, in the form of Hovmöller diagrams of the DC in active MJO and inactive MJO environments and their difference (a-c), as well as the more quantitative line diagrams of the DC (e-f), and the average precipitation and the DC amplitude between the two environments (f), all as a function of distance from the coastline.

Compared to inactive MJO environments, the amount of precipitation is much higher during active MJO events, which increases the amount of DC-associated precipitation. How-

ever, the precipitation increase is not uniform throughout the course of the day, nor is it uniform in its position relative to the coastline. The amount of precipitation over water is more than doubled during most of the day, with the greatest increase in the early morning. Precipitation over land shows a generally lesser increase than over water, and it is most prominent in the evening - in the early morning, there are even times when the DC is unaffected by the MJO (Fig. 4.3c).

These results show that at all hours of the day and at virtually all distances from the coastline, it rains more during active MJO periods. The amplitude of the diurnal cycle is enhanced during the active phase of the MJO, with a much stronger enhancement over water than over land. This indicates that the MJO (as defined by precipitation tracking) is largely carried through the MC over water, and that the DC patterns of precipitation persist even under large-scale active MJO conditions.

4.5 MJO Characteristics in Model Simulations

To evaluate the relative effects of flattening topography and removing the land and its associated DC over the MC, we consider how the MJO is represented in observations and our simulations. The large-scale precipitation and surface wind fields for the simulations are shown in Fig. 4.4, Fig. 4.5 shows time series of precipitation over the MC, Fig. 4.6 shows the LPT-tracked MJOs. Fig. 4.7 summarizes some statistics that help characterize the differences in the MJOs among model simulations.

The CTRL simulation does a good job at representing the large-scale environment of the November-December 2011 MJO event Chen et al. (2016), as can be seen the Hovmöller diagrams of rain rate and surface zonal winds in Fig. 4.4. The CTRL's precipitation signal is noisier than in observations due to its higher resolution and a high bias in precipitation (see Savarin and Chen (2022b), their AO4-FLX experiment). The post-MJO suppression in CTRL is not as strong as was observed, but it does propagate through the MC, even though the signal is not as smooth as over the IO or in observations (Fig. 4.4b). The surface westerlies associated with the MJO are well reproduced, and they persist over the

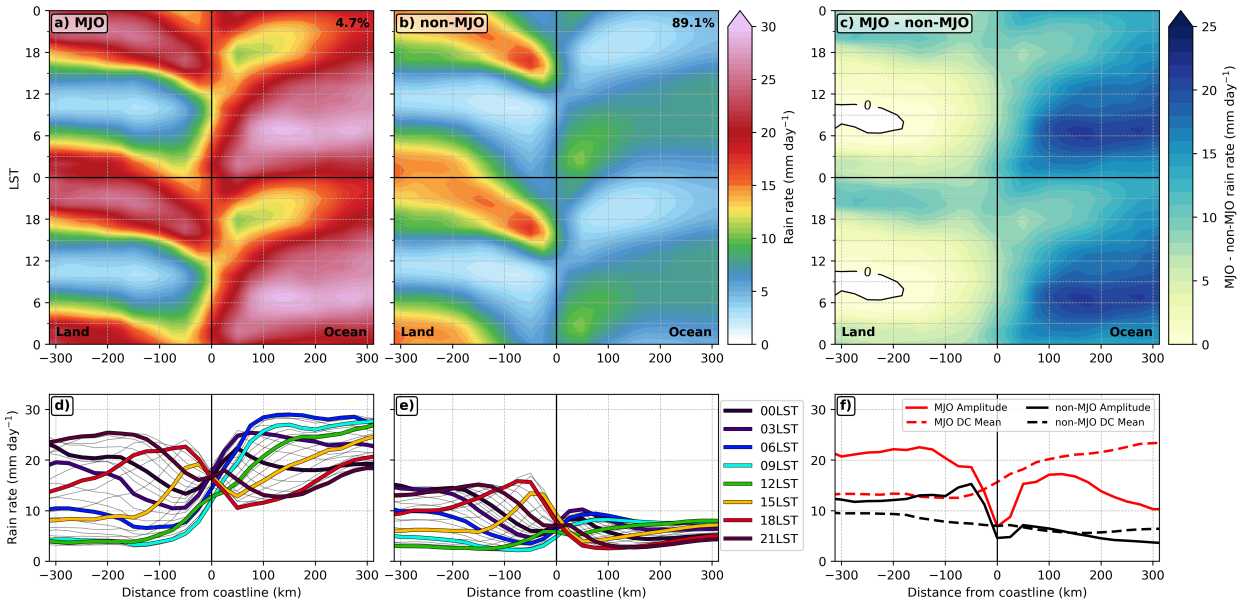

Figure 4.3: 20-year IMERG DC composites in a, d) active MJO and b, e) inactive MJO environments and c, f) active - inactive MJO - MJO DC composite differences. The color bar in a) and b) is the same as in 4.2c up to 20 mm day^{-1} for easy comparison, and new colors have been added for rain rates above 20 mm day^{-1}. In f), the solid lines show the amplitude of the DC composite, and the dashed lines show the average value of the DC composite, red for areas inside the MJO convective envelope, and black for areas outside the envelope and its 5° filtering area. The percentages of in the top right corner of a) and b) denote the percentage of time that the MC experiences active and inactive MJO environments, respectively. The remaining 6% is the area outside the MJO but inside the 5° filtering area.

IO after the MJO has propagated east. Flattening MC terrain results in small changes in the large-scale environment compared to the CTRL. Over the MC, precipitation seems more scattered and the MJO-associated eastward-propagating precipitation is more difficult to distinguish until 3 December, where a heavy rainfall event forms near 130°E. Surface westerly winds over the MC are stronger than in CTRL, which can be attributed to the removal of topographical barriers. When MC land is removed in the WATER simulation, we see a lot more precipitation and a much clearer eastward propagation associated with MJO

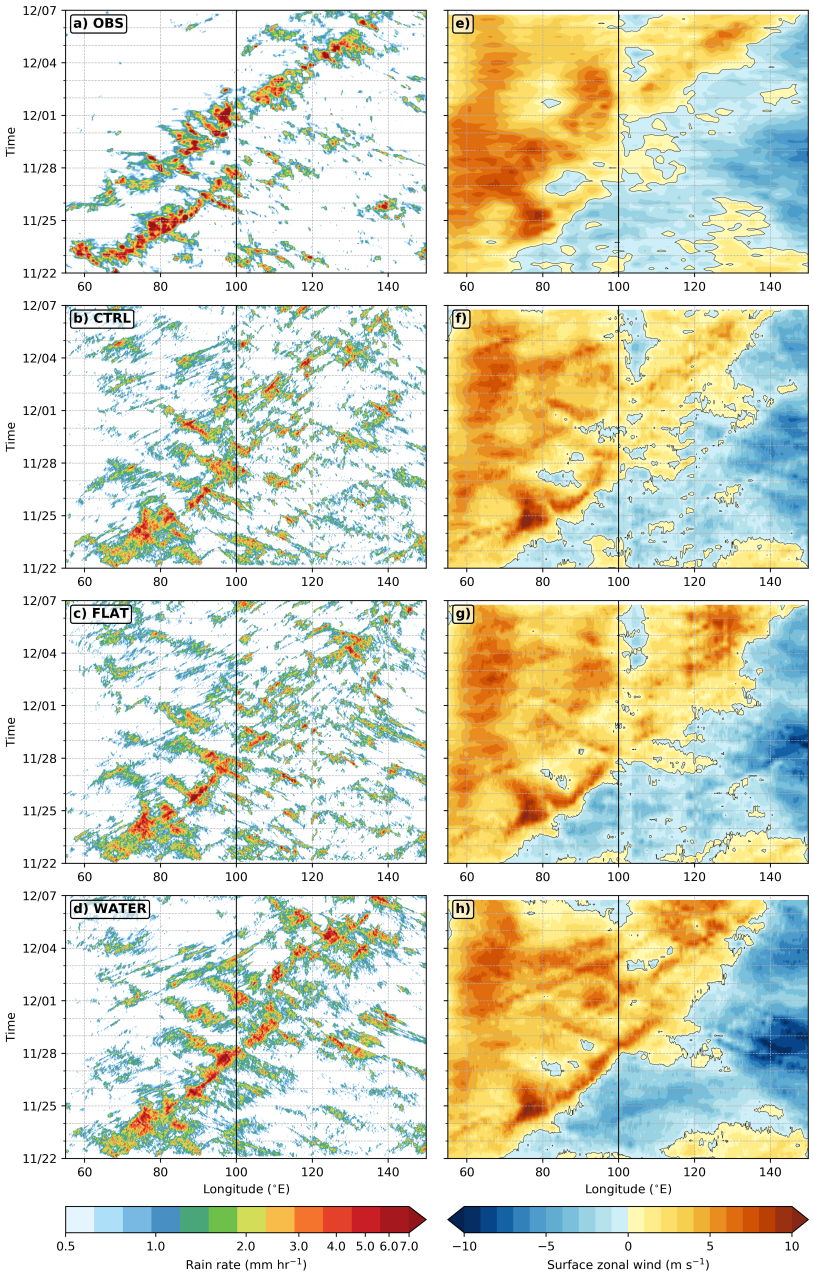

Figure 4.4: 5°S - 5°N Hovmöller diagrams of rain rate (left, mm hr^{-1}) and surface zonal wind (right, m s^{-1}) in observations and model simulations. The products are ordered from top to bottom as follows: observations (IMERG precipitation and CCMP surface winds), CTRL, FLAT, and WATER simulations. The vertical line at 100°E denotes the separation of the IO and MC. CTRL simulation contains real topography, which is flattened over the MC in FLAT, and completely removed in WATER experiments.

convection. After MJO passage, precipitation suppression over the IO is stronger than in previous simulations, as are surface westerly winds - this is a result of reduced friction over the entire MC.

Fig. 4.5 shows time series of MC precipitation averaged over the MC box outlined in Fig. 4.2 for IMERG observations and model simulations. All model simulations reproduce an increase in precipitation associated with the MJO that begins after November 25, ahead of the MJO centroid entering the region. The WATER simulation produces the largest amounts of precipitation, and the most precipitation increase associated with the MJO, while simulations containing land produce less of both. This indicates that during MJO passage (the time range during which the MJO centroid is located over the MC are outlined with colored horizontal bars on the bottom of Fig. 4.5), the presence of MC land is disruptive to MJO-associated precipitation enhancement.

These large-scale differences are reflected in LPT-tracked MJOs shown in Fig. 4.6. At the 17 mm precipitation threshold, both the CTRL and FLAT simulations dissipate over the MC before the end of the simulation, while the observed and WATER MJOs propagate smoothly. The average 24-hour propagation speed in observations is 5.8 m s^{-1}, which is closely matched by 5.6 m s^{-1} in WATER. The propagation speeds of CTRL and FLAT MJOs are 3.4 and 3.5 m s^{-1}, respectively, so in addition to dissipating over the MC, they are also slower.

Soon after the CTRL and FLAT MJOs extend into the MC region (after 28 November), the MJO area begins to shrink, and then remain relatively steady while the MJO centroid is still in the IO. After the MJO centroids enter the MC on 2 December (at which point more than half of the MJO is over the MC), the CTRL and FLAT MJOs begin to quickly dissipate, with the FLAT MJO weakening at a faster rate. The initial reduction in MJO size when first entering the MC is also present in observations - but after the initial weakening, the observed MJO's size remains relatively steady until the end of the simulation period. As there is no land present in the WATER simulation, the MJO area remains relatively steady throughout the simulation, with some size fluctuations as the tracking algorithm picks up

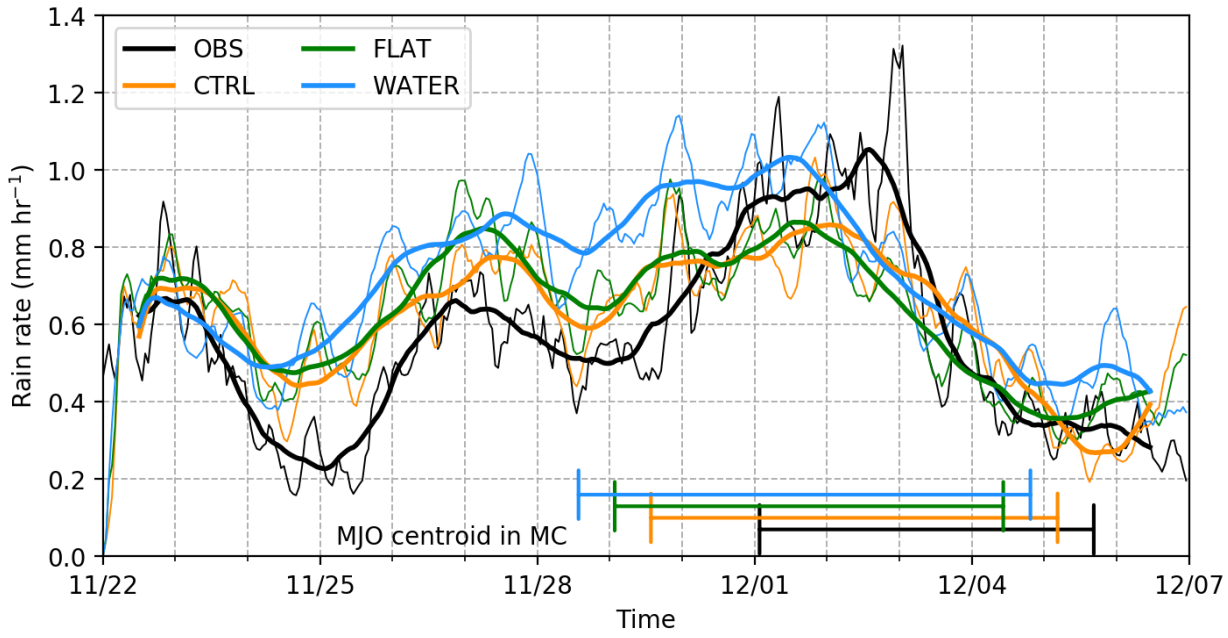

Figure 4.5: Time series of average rain rates over the MC (90-120°E, 10°S-10°N). Thick lines show the 24-hour running mean of hourly precipitation. The horizontal bars indicate the time during which the MJO centroid is over the MC. Observations are from IMERG; CTRL simulation (orange) contains real topography, which is flattened over the MC in FLAT (green), and completely removed in WATER experiments (blue).

some convection over the western Pacific.

These results show that, as expected, when all obstacles are removed from the MJO's path (such as in WATER), its propagation is smooth, and its precipitation does not weaken. Removing mountains alone but keeping islands where they are (as in FLAT) has a much smaller impact on MJO propagation (compared to CTRL), and, surprisingly, that impact acts to weaken the MJO and impede its propagation even further. In the next section, we take a closer look at the diurnal precipitation patterns over the MC and how they can disrupt MJO propagation to explain this unexpected result.

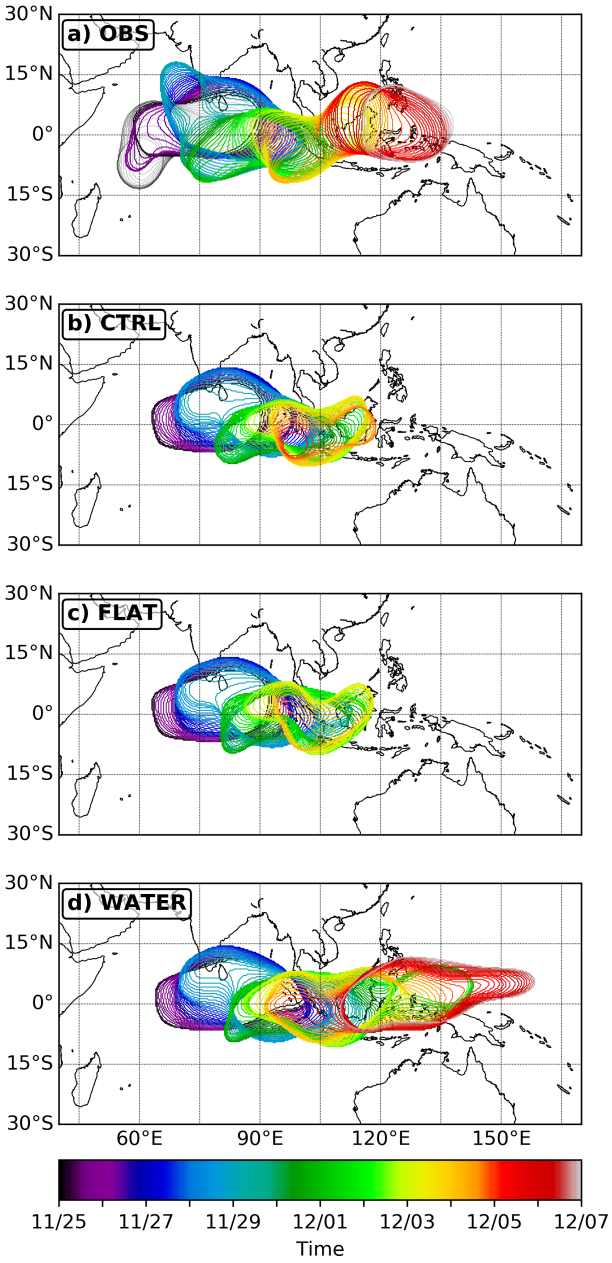

Figure 4.6: LPT tracking of the MJO convective envelope in a) IMERG observations, b) CTRL, c) FLAT, and d) WATER simulations at the 17 mm precipitation accumulation threshold. The colors represent the MJO convective area at a given time. CTRL simulation contains real topography, which is flattened over the MC in FLAT, and completely removed in WATER experiments. Observations (black) are from tracking IMERG precipitation at a 17 mm threshold. CTRL simulation contains real topography, which is flattened over the MC in FLAT, and completely removed in WATER experiments.

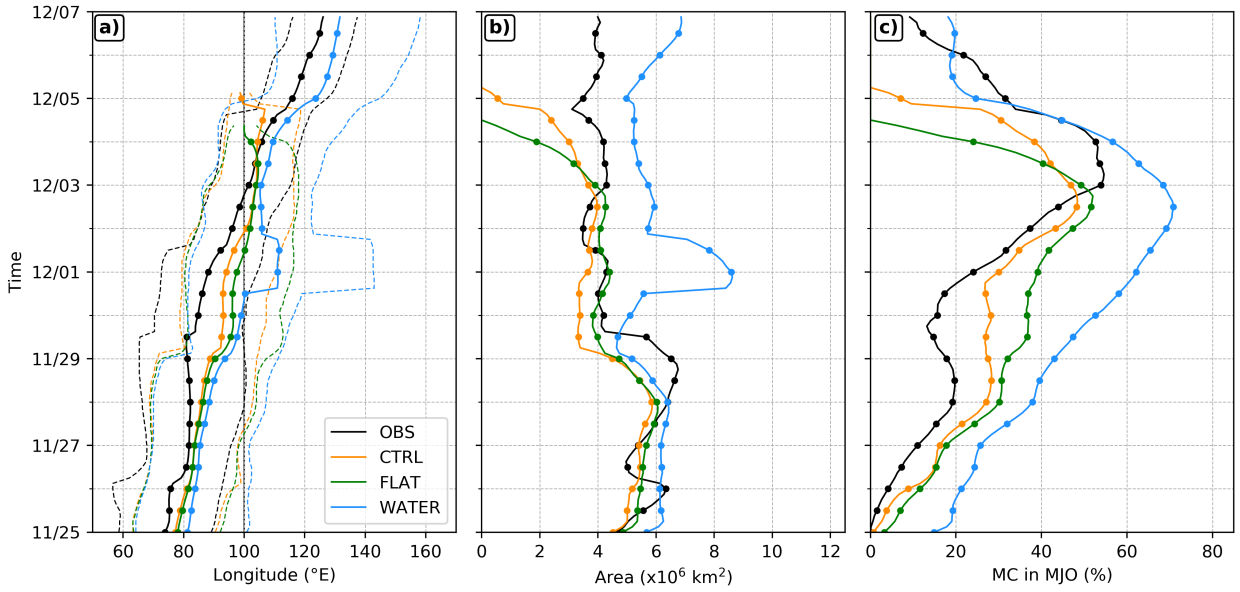

Figure 4.7: MJO tracking summary with time. a) Location of the MJO centroid (solid lines) and its trailing and leading edges (dashed lines), b) MJO area (x10^6 km^2), and c) the portion of MC inside the MJO (%). The MC area is defined from 90-120°E, 10°S-10°N as in Fig. 4.2a. The vertical line at 100°E in a) denotes the separation between the IO and MC. Observations are from IMERG; CTRL simulation (orange) contains real topography, which is flattened over the MC in FLAT (green), and completely removed in WATER experiments (blue).

4.6 Diurnal Cycle of Precipitation

In this section, we examine the DC of precipitation over the MC (90-120°E, 10°S-10°N) for the period from 22 November to 6 December 2011 to evaluate how well the DC is represented in CTRL, and how it changes among model simulations. Fig. 4.8 shows the average rain rates over all MC land and ocean points (a, b), and the percentage of total rain that falls over them (c) relative to local solar time. To put our 15-day period into broader context, observations for the model period are shown in solid colors and bars, while the dashed lines and hatched bars show the 20-year IMERG climatology. Unsurprisingly, the amount of

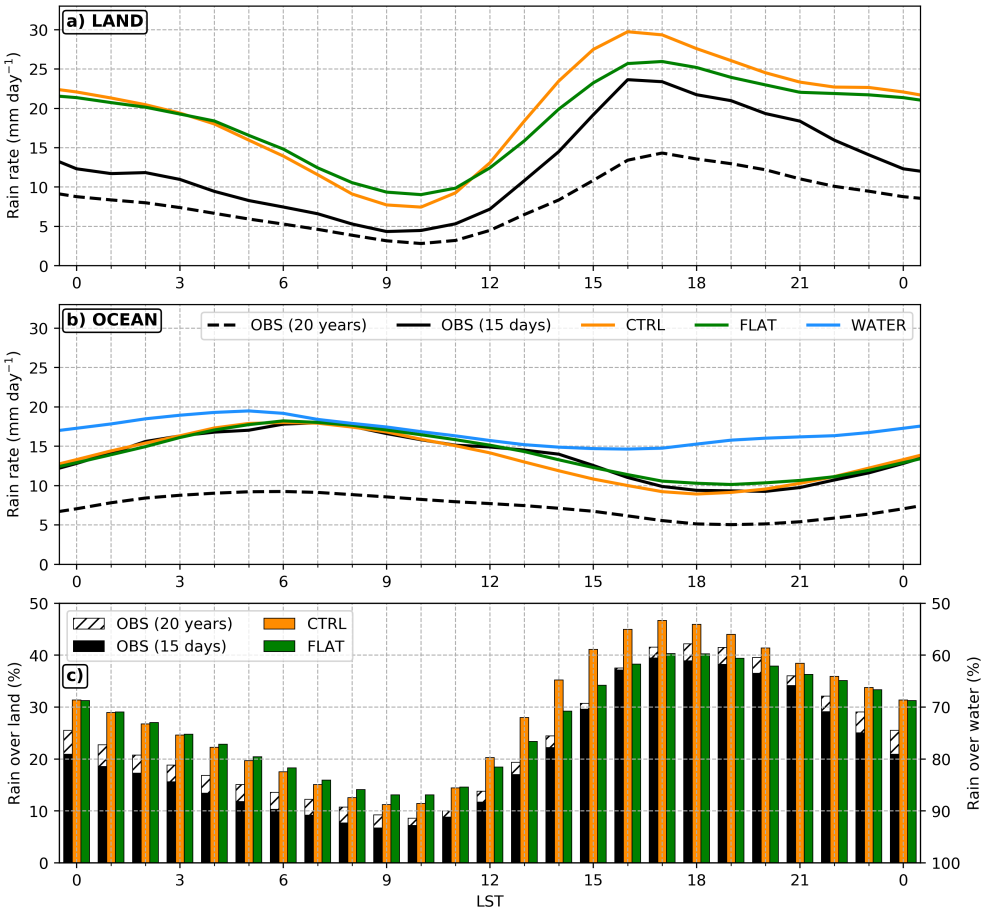

Figure 4.8: DC of precipitation over the MC. The DC is shown over a) land points and b) ocean points; c) percentage of total precipitation over the MC that falls over land (left axis), or water (right axis). The dashed black lines show the 20-year composite DC, while the solid black lines are only for the period of the model simulation. The DC is only composited over the MC area outlined in 4.2a. Observations are from IMERG; CTRL simulation (orange) contains real topography, which is flattened over the MC in FLAT (green), and completely removed in WATER experiments (blue).

precipitation in the 15-day period is higher than the 20-year averages at all times of day. This is due to two factors: first, we are considering a shorter period, so extreme rain rates would contribute more strongly to the average, and second, the 15-day model period contains

an MJO event, which increases the amount of precipitation over the MC - especially over water (Fig. 4.3). The signature of the MJO can be inferred from the fact that at any time of day, the portion of precipitation that falls over water is greater in the 15-day composite than in the 20-year one (Fig. 4.8c). Apart from the difference in magnitude, the 15-day, and the 20-year DC composites over land and water have the same characteristic timing, indicating that the method we use for analyzing the DC is appropriate even for such short time periods.

We noted previously that both the CTRL and FLAT simulations tend to overproduce precipitation (Fig. 4.4), but when considering only precipitation over the MC ocean points (Fig. 4.8b), the average rain rates in model simulations accurately reproduce IMERG observations both in intensity and timing of precipitation extrema. In the WATER simulation, the amount of precipitation over water is higher over the course of the day, and closer to the DC we would see over open ocean, with smaller amplitude and a precipitation maximum slightly earlier in the day (Nesbitt and Zipser, 2003). Over MC land, the timing of the diurnal precipitation extrema still matches that of observations, but the precipitation intensity is consistently exaggerated (Fig. 4.8a), which results in proportionally more rain falling over land. The land-sea contrast present in observations and CTRL and FLAT simulations results in land-locked convection in the afternoon, with convective systems that are much more intense than what we see over water.

The separation of land and water points for the DC of precipitation in Fig. 4.8 shows that in model simulations, convection over land is more intense in than in observations, with a slightly lower-intensity and longer-lasting precipitation peak in FLAT. However, this way of looking at land and sea precipitation obscures the changes in precipitation patterns over land that arise from imposed terrain modifications. To investigate those, Fig. 4.9 shows distance-from-coastline relative Hovmöller diagrams of rain rate for the 15-day period in observations and CTRL and FLAT simulations (top), and their 15-day composites (bottom). Seen in this manner, we can note that flattening MC terrain results in changes in the location of precipitation, as well as in precipitation frequency.

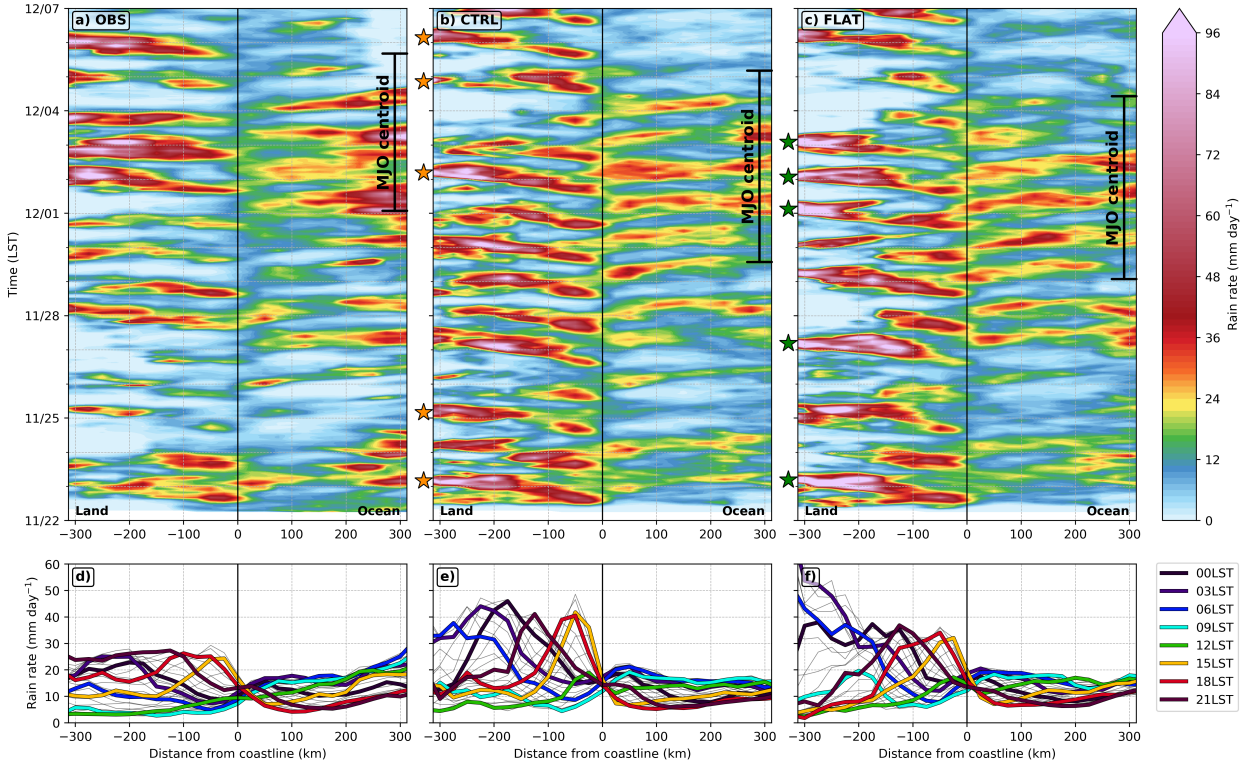

Figure 4.9: Distance-from-coastline DC composites. Top: hovmöller diagrams of rain rate (mm day^{-1}) with LST for a) IMERG observations, b) CTRL, and c) FLAT simulations. Bottom: quantitative 15-day composite DC of rain rate (mm day^{-1}) for d) IMERG observations, e) CTRL, and f) FLAT simulations. The arrows on the right edge of Hovmöller diagrams denote the times during which the MJO centroid is located over the MC (between 90 and 120°E). The stars on the left indicate the five most intense convective events that occurred more than 200 km inland (see Fig. 4.11). Observations are from IMERG; CTRL simulation contains real topography, which is flattened over the MC in the FLAT experiment.

Compared to observations, the DC of precipitation in CTRL is stronger and more regular, with sea breeze precipitation propagating far inland on most afternoons while observations show more day-to-day variability. As inferred from Fig. 4.8, the amount of precipitation over land is exaggerated by up to 80% while the amount of precipitation over water is simulated more accurately (Fig. 4.9e); therefore, the precipitation in the model is more land-dominated

than in observations.

Flattening terrain results in precipitation pattern changes that can be separated into two regions over land: the near-coastal region (within 100 km inland), and the far-inland region (more than 200 km inland). In the near-coastal region, the FLAT DC is diminished but remains regular while in the far-inland region, it is strongly amplified in intensity but reduced in frequency. Near the coast, the reduction in peak precipitation is due to two effects - concurrent effects of sea- and valley-breezes that amplify onshore flow in the early afternoon, and mountains near the coast (along the west coast of Sumatra) that both act to amplify precipitation in CTRL but not in FLAT. But the more interesting changes are happening far inland, where sea breezes from different sides of islands (mainly Borneo) in FLAT converge and grow into organized mesoscale convective systems that are more intense, larger, and last longer than in CTRL. Outside of MJO conditions (before 29 November), these systems persist into the next morning and suppress precipitation for the rest of the day, creating a two-day cycle. During active MJO, the increased moisture supply means that these large systems are formed every day. In a 15-day composite from the FLAT simulation (Fig. 4.9f), inland precipitation peaks are significantly stronger than in CTRL even though they occur less frequently.

To summarize, these results show that model simulations with land-sea contrast simulate the DC over MC water accurately, but show more, and more intense land-locked convection in the afternoon. When terrain is flattened, we see the coastal sea-breeze precipitation is diminished in amplitude, but a convergence of sea-breezes from all around islands, which are no longer disrupted by terrain, results in an amplification of convection far inland. In the next section, we focus on the differences in convective systems that arise from modifying MC terrain.

4.7 Land-Locked Convection and Suppression of MJO Precipitation over Water

In this section, we take a closer look at the differences in land-locked convection between the CTRL and FLAT simulations. As noted previously, the FLAT simulation produces inland convective systems that are more intense, larger, and longer-lasting than in the CTRL simulation (Fig. 4.9, where mountains disrupt the convergence of sea breezes from different sides of the island. In Fig. 4.10, we show an example of the evolution of one such convective system in the FLAT simulation that developed overnight between 26 and 27 November. Fig. 4.11 demonstrates that the case shown in Fig. 4.10 is not unique, and the associated patterns of low-level convergence and moisture supply are illustrated in Fig. 4.12.

The evolution of sea-breeze fronts into a large MCS in the FLAT simulation in Fig. 4.10 shows precipitation and surface wind maps (left) and vertical cross-sections of hydrometeor mixing ratio to indicate clouds (dotted in black), potential temperature anomaly (shaded in color) from the previous hour, and zonal and vertical wind components (right). The vertical cross-sections are plotted with longitude and averaged between 1°S and the equator, and the vertical winds have been multiplied by a factor of 10 for better visibility. The three rows of figures correspond to three different times, one in the early stage of MCS development (21-22 LST on 26 November), when convection is beginning to converge inland, along the south-east coast of Borneo (top), one in the mature stage (00-01 LST on 27 November) when convection is organized on a very large scale (middle), and one in the dissipating stage (05-06 LST on 27 November), when convection is dissipating in this region, but intense precipitation has migrated to the north and west (bottom).

The evolution of the convective system in Fig. 4.10 indicates that in the FLAT simulation, a large, organized, and robust mesoscale convective system (MCS) and its associated circulation develop and propagate over Borneo. During the early stage, the system is just beginning to propagate and develop inside the averaging box near 115°E (Fig. 4.10a). There is some upward motion, and a weak warm anomaly is beginning to develop in the mid-troposphere, coincident with where clouds are present (Fig. 4.10d). Three hours later, the

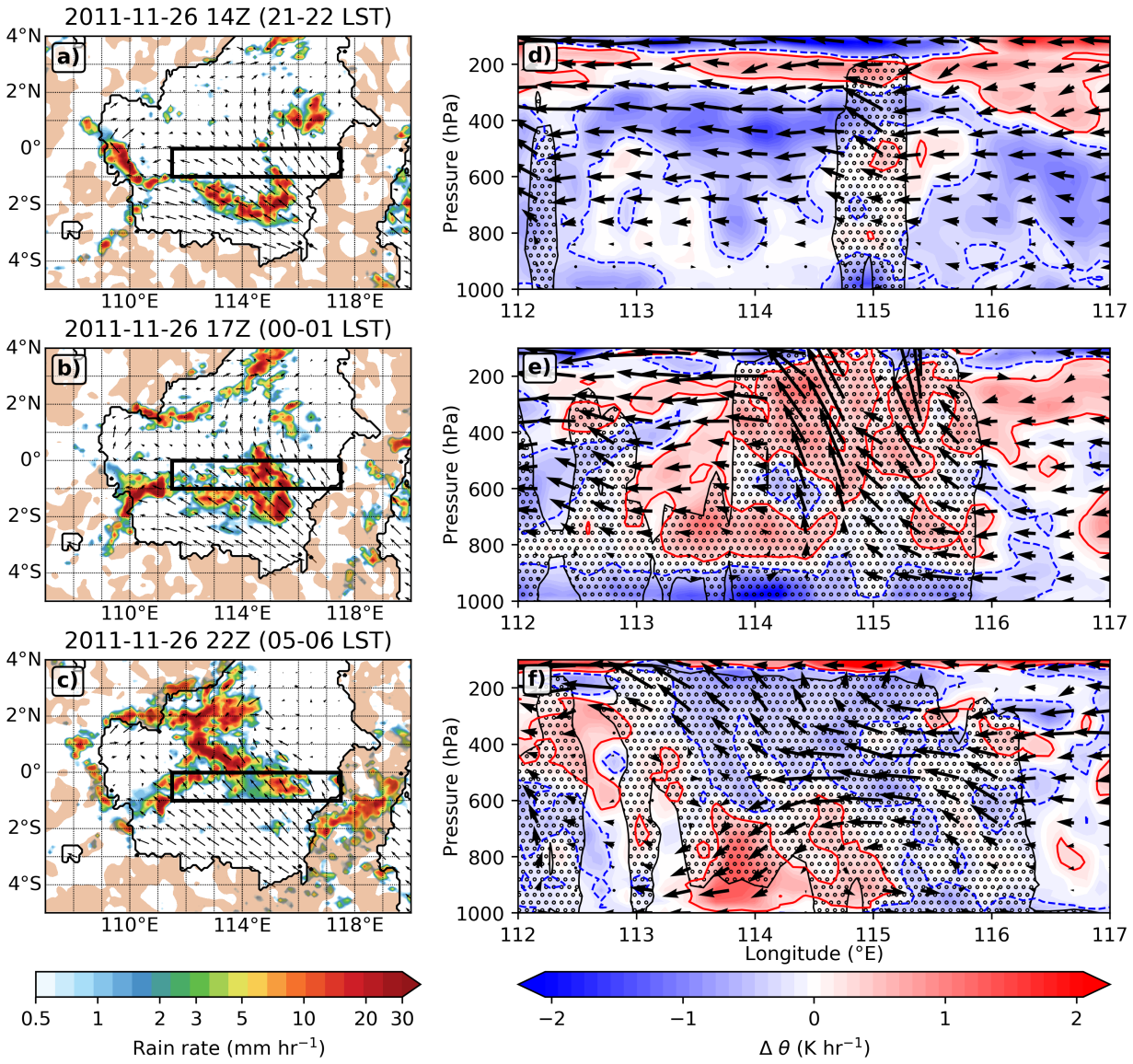

Figure 4.10: Evolution of a large, long-lasting mesoscale convective system in the FLAT simulation (flattened topography over the MC). Left: 3-hourly averaged precipitation (mm hr^{-1}), 10 m winds over land (vectors), and 500 hPa downward vertical velocity over water (brown shading) centered on 26 November at a) 14Z (21-22 LST), b) 17Z (00-01 LST on Nov 27), and c) 22Z (05-06 LST on Nov 27). Right: 1°S-0° averaged vertical cross-sections of zonal and vertical winds (arrows), potential temperature change from the previous hour (K hr^{-1} ; red-blue shading), and cloud area approximated by hydrometeor content (black hatching) for the corresponding times. Vertical velocity is multiplied by 10 to emphasize the pattern, and red and blue contours outline a temperature change of 0.25 K hr^{-1}.

system has matured and is more than 200 km across, with strong updrafts and strong mid- and upper-tropospheric heating, indicating that the MCS is beginning to develop its own circulation and a broad upper-level region of stratiform clouds (Fig. 4.10b, e). The presence of a deep inflow layer we can see in Fig. 4.10e is associated with mature MCSs, where large regions of stratiform clouds and precipitation are likely present, and has been numerically shown by Mechem et al. (2002). Five hours later, the system has grown to over 300 km across and precipitation is dissipating inside the averaging box as the system is propagating away from it. There is subsidence from the mid-troposphere, and warming has moved closer to the surface, while upper levels begin to cool (Fig. 4.10c, f).

To show that the development of the MCS described in Fig. 4.10 is not a singular occurrence but a systematic difference between CTRL and flat simulations, we take the five most intense convective events that occur far inland and compare the results between the simulations. The five most intense events are determined based on average rainfall rate more than 200 km inland and marked with starts next to the Hovmöller diagrams in Fig. 4.9. Fig. 4.11 shows the time series of far-inland rain rate (top), with the highlighted intense convective events and the rain rate thresholds that need to be exceeded for each simulation. The thresholds have been chosen so that they result in the same number of hours within the simulation during which the threshold is exceeded. A rain rate threshold of 3.6 mm hr^{-1} in FLAT results in 20 hours separated between 5 convective events, while the same number of hours and convective events are identified with a threshold of 2.2 mm hr^{-1} in CTRL - the convective events are over 60% more intense in FLAT. The precipitation for the highlighted times is composited together for the CTRL and FLAT simulations (Fig. 4.11b, c), and their difference is shown in Fig. 4.11d, with red colors indicating where rain rates are higher in FLAT than in CTRL.

Large land-locked convective events in the FLAT simulation are spread over larger and more central areas of islands, and that the precipitation that occurs in them is more intense when compared to the systems that develop in CTRL. These large MCSs suppress precipitation over the surrounding waters (brown shading in Fig. 4.10) where the MJO is attempting

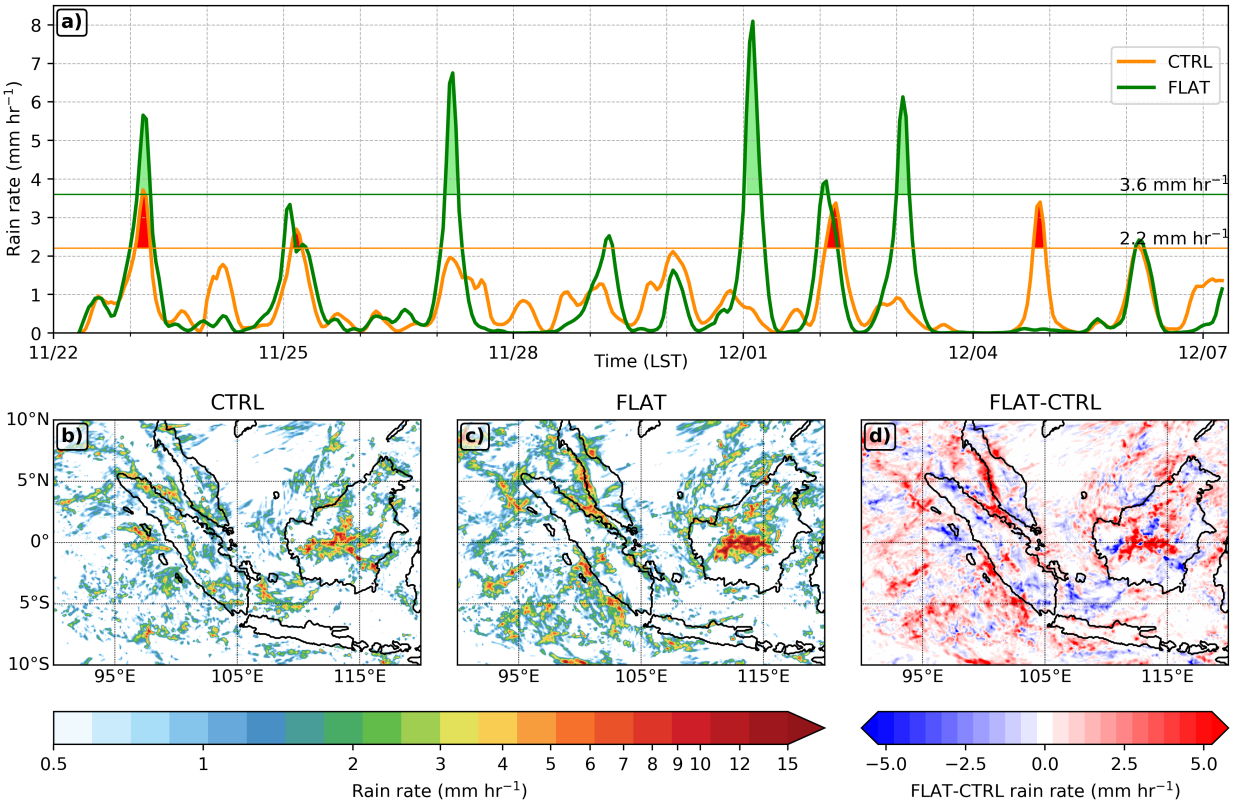

Figure 4.11: Comparison of inland convective systems in CTRL and FLAT simulations. a) Time series (in LST) of rain rate (mm hr^{-1}) averaged over land areas greater than 200 km from the coast, highlighting the five most intense convective events for each simulation. b, c) Rain rate (mm hr^{-1}) composites of the five intense convective events in CTRL and FLAT simulations, respectively. d) The difference in precipitation (mm hr^{-1}) associated with intense convective events between FLAT and CTRL simulations. CTRL contains real topography, while in FLAT, topography over the MC is flattened to sea level.

to enhance precipitation around the same time of day. In FLAT, the larger and more intense MCSs can develop because there is no terrain disrupting the convergence of sea breezes from different sides of the islands, and there are no mountains forcing upward motion in specific locations.

The systematic differences in precipitation patterns between CTRL and FLAT are also

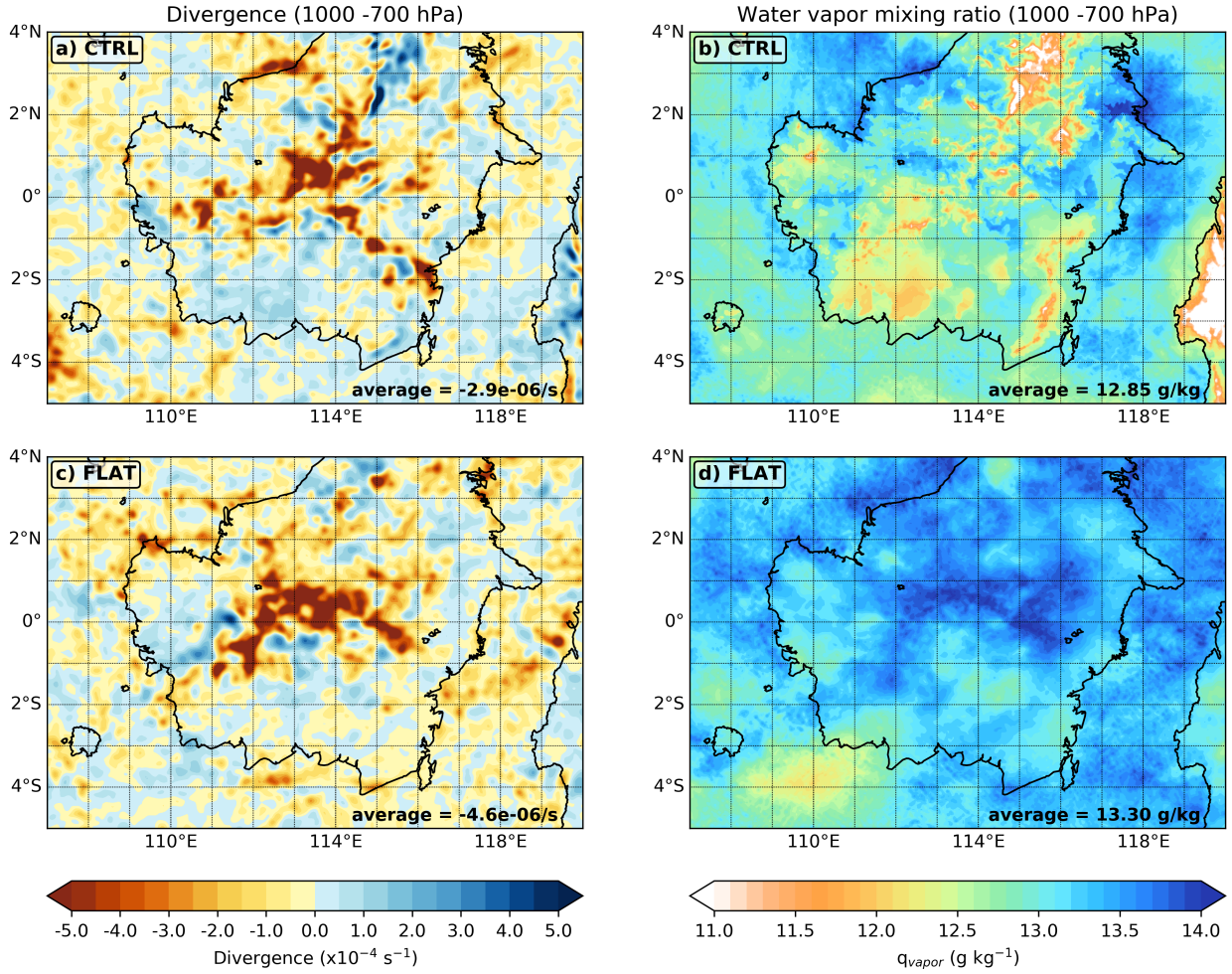

Figure 4.12: Comparison of 1000-700 hPa divergence (s^{-1}, left) and water vapor mixing ratio (g kg^{-1}, right) in the CTRL (top) and FLAT (bottom) simulations. The comparison is made using the five most intense convective events for each simulation, as defined in Fig. 4.11. The numbers at the bottom right indicate regional averages of the depicted fields. CTRL contains real topography, while in FLAT, topography over the MC is flattened to sea level.

evident in the accompanying patterns of low-level convergence and water vapor supply shown in Fig. 4.12. The compositing is done in the same manner as for precipitation in Fig. 4.11, and we can see that most of Borneo is covered in large-scale convergence in the FLAT simulation (Fig. 4.12c). In CTRL, the convergence region is smaller and less contiguous,

and we also see the signature pattern of elevated topography, with dipoles of convergence and divergence in the north of the island (Fig. 4.12a). The convergence and water vapor mixing ratio shown are averages for a layer that spans between 1000 and 700 hPa, indicating that the low-level convergence is not confined solely to the boundary layer, which implies a presence of mature MCSs and elevated mid-level moisture Mechem et al. (2002). But the sharper difference is evident when looking at low-level moisture availability - due to elevated terrain in CTRL, large areas of Borneo show much lower water vapor content near the surface than in FLAT (Fig. 4.12b, d). In fact, the during the most intense convective events, low-level convergence in FLAT is 58% higher than in CTRL, and the low-level water vapor shows a 3% increase, indicating that convection mainly grows due to increased and widespread convergence. Fig. 4.12 explains why convective systems can grow larger and stronger in FLAT in a physical sense - the collocation of low-level convergence and moisture supply can support precipitation. In CTRL, though we see large areas of convergence, the moisture supply is lower, so the systems can only grow in a limited capacity.

These effects can be seen in the differences between the composite DC in the CTRL and FLAT simulations separated into the MJO and non-MJO environments shown in Fig. 4.13, following the same method as in Section 3. We can clearly see the amplified enhancement of far-inland convection in the early morning on the FLAT simulation, while far-inland convection is slightly suppressed by the MJO in CTRL. At the same time, the enhancement of precipitation over water in MJO environments is smaller in FLAT than in CTRL, indicating that the mountains in CTRL present a physical barrier to MJO flow, but they also disrupt the large-scale organization of convection due to convergence of multiple sea breeze fronts. The resulting MCSs that develop over land in CTRL occur on a smaller scale - which is still disruptive to the MJO, but to a lesser extent. So, in a way, mountains can help the MJO propagate across the MC by disrupting the large convective systems that would develop in their absence.

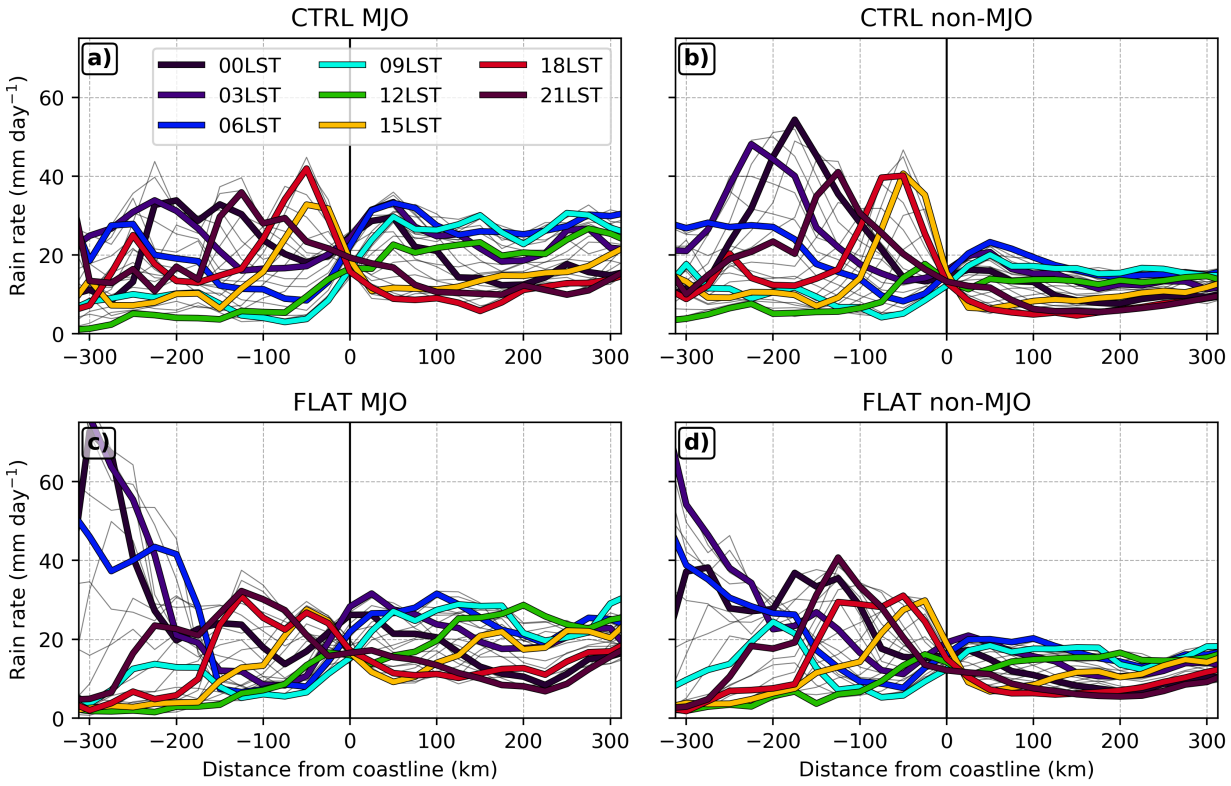

Figure 4.13: Comparison of DC composites for the CTRL (real topography, top) and FLAT (flattened topography over the MC, bottom) simulations under MJO (left) and non-MJO environments (right). The MJO and non-MJO environments are defined as in Section 4.4 and Fig. 4.3.

4.8 Summary and Conclusions

This study investigates the MC barrier effects to MJO propagation through a systematic analysis of the impacts of MC terrain and land-sea contrast. Three atmosphere-ocean coupled simulations at convection-permitting resolution are conducted to evaluate the responses in MJO evolution and eastward propagation to changes in MC topography.

The main results can be summarized as follows:

1. Land and land-sea contrast weaken the MJO and disrupt its propagation over the Maritime Continent.

2. Land-sea contrast of MC islands induces a strong diurnal cycle with strong land-locked convection in the afternoon.

3. Mountains are less disruptive to MJO propagation than the larger and stronger land-locked convective systems that form over land without them.

When MC land is removed and replaced by shallow ocean (the WATER simulation), the MJO moves across the region as a smoothly-propagating, coherent area of large-scale precipitation that does not weaken in the process. When islands are present, with or without mountainous terrain, the MJOs over the MC are first reduced in area, and eventually dissipate over the region. This indicates that the presence of land and the land-sea contrast induced by it act to weaken the MJO during its propagation over the region (Figs. 4.4, 4.6, 4.7). This was an expected result, and it agrees with previous studies showing that once an MJO enters the MC, it is frequently weakened, and its structure altered by land interactions (e.g., Burleyson et al., 2018; Hagos et al., 2016; Zhang and Ling, 2017).

As land is introduced into the MC without terrain (FLAT simulation), it results in the addition of a DC that follows the pattern of the coastal regime described in Kikuchi and Wang (2008). This regime experiences an alternating diurnal pattern characterized by offshore phase propagation with peak precipitation occurring in late evening and early morning (the land breeze; Fig. 4.8b), and onshore phase propagation with more intense peak precipitation in the afternoon (the sea breeze; Fig. 4.8a). The resulting convective systems over land can be separated into two types. The near-coastal convection that is directly forced by sea-breezes (and the background flow) is present on each day of the model simulation. The far-inland convection that is forced by the convergence of multiple sea breezes (and the background flow) is present on each day during active MJO conditions, but only occurs every other day before MJO arrival (Fig. 4.9c). The far-inland sea breeze convergence results in the formation of very large organized MCSs that develop their own circulation, produce heavy-precipitation, and last well into the morning hours (Figs. 4.9c, 4.10). The long-lasting systems then suppress the far-inland convection on the following day (when there is no

MJO) due to reductions in mid-upper-level moisture and insolation-induced surface heating. During active MJO conditions, the intense far-inland MCSs are triggered every day due to increased background moisture and upward vertical velocity.

The large daily MCSs that form far inland in the FLAT simulation last into the next morning, suppressing precipitation that is supposed to be initiating over coastal waters at the same time due to the land breeze. The early morning is also the time during which, climatologically, the MJO tends to most enhance precipitation over water, and this local suppression works against that. Therefore, the large land-locked MCSs that develop in the later afternoon and persist until morning reduce the precipitation enhancement over water that happens due to the MJO (Fig. 4.13c) and result in a weakened MJO with a discontinuous propagation across the MC (Figs. 4.6c, 4.7)

The mountainous terrain added in CTRL provides a disruption to the FLAT DC that results in a change in diurnal precipitation patterns. Compared to FLAT, the amount of precipitation falling over land is increased in CTRL (Fig. 4.8a), but it is distributed in smaller systems that are less disruptive to the MJO. The amplitude of the DC near the coastline, both of land and water) is increased (Fig. 4.9e) while the systems that develop far inland are smaller in area and less intense (Fig. 4.11). The low-level convergence associated with these systems is much weaker than in FLAT due to flow disruption by mountains, and as they cannot grow as large, they induce less suppression to precipitation developing over nearby waters (Figs. 4.12, 4.13a, b).

Compared to FLAT, the MJO propagation in CTRL is smoother contains more precipitation, and dissipates later (Figs. 4.6b, 4.7). This implies that considering that the land-sea contrast is disruptive to the MJO, mountains act to reduce the disruption to MJO propagation, because they disrupt the even-stronger MCSs that would develop in their absence.

4.9 Discussion

Our results show that the active MJO in IMERG observations increases the amount of precipitation throughout the MC, and thus increases the amplitude of the DC over both land

and water (Fig. 4.3), though the increase over water is dominant. These results disagree with previous studies on the subject, which found that while the amplitude of the DC over water is increased by an active MJO, the amount of precipitation over land is reduced (Oh et al., 2012; Rauniyar and Walsh, 2011). We believe the reason for this discrepancy lies in the methodology of MJO and DC identification. Most other studies of the MJO identify events based on the Real-Time Multivariate MJO Index (RMM, Wheeler and Hendon, 2004), or similar indices based on global anomaly fields. Our MJO identification method relies on large-scale precipitation tracking (LPT), which directly tracks MJO precipitation, and only considers the points that lie inside the MJO convective envelope as active, so that at any one time, parts of the MC can be inside the MJO, while other parts are not.

Our results also disagree with the earlier study by (Inness and Slingo, 2006) which finds that it is the mountains, and not the presence of islands, that blocks MJO propagation through the MC. However, their model simulations were performed at very low resolution (2.5° x 3.75°), and many studies have shown that increasing resolution helps with the representation of the MJO (Love et al., 2011; Savarin and Chen, 2022a), so their findings could be attributed to something other than the barrier effect of the MC.

A similar set of convection-permitting simulations with real and flattened topography was performed by Tan et al. (2022) and by Zhou et al. (2021a), both without dynamic atmosphere-ocean coupling and for two different MJO events. Tan et al. (2022) find similar high biases in the DC of land precipitation that are characteristic of our simulations, but also show a low bias in the amplitude of the DC over water, indicating that air-sea coupling could be an important contributor to the variability of precipitation over water. Their results generally agree with our study in that when topography is removed, the peak precipitation over land is reduced, but tapers off more slowly than when topography is present (e.g., Fig. 4.8a). Though their analysis focuses on different aspects of the DC, the fact that they find similar differences in their simulations makes the results of our study more robust.

We recognize that the afternoon peak land-locked convection in our coupled model simulations is higher than indicated by IMERG observations (Fig. 4.8a), though it is unclear

whether the land precipitation bias is as large as it appears. Previous studies have found the resolution of IMERG to be high enough to accurately represent the DC of precipitation (e.g., Tan et al., 2019), and our results qualitatively compare well with precipitation radar studies in the region from the TRMM era (e.g., Biasutti et al., 2012). But the accuracy of hourly IMERG precipitation retrievals over the MC region's sharp land-sea contrast areas and dynamic terrain has not yet been thoroughly evaluated. Some evaluation studies indicate that IMERG tends to underestimate precipitation associated with tropical cyclone precipitation over the United States (e.g., Mazza and Chen, 2022; Tian et al., 2018), while a study by Hayden and Liu (2021) showed both regional under- and over-estimates in the tropics. In addition, many modeling studies performed at higher resolutions show a high bias in land convection over the MC; at lower resolutions, the timing of the DC as well as its amplitude are frequently misrepresented (e.g., Love et al., 2011; Watters et al., 2021).

Though this study only contains model simulations of a single (though well-observed) MJO event, our findings have large implications for numerical modeling of the MJO and its propagation over the MC. Specifically, we expose the role of mountainous and diverse terrain over the MC as important to disrupting the formation of very large MCSs over land that could act to obstruct MJO propagation. In models run with low-resolution terrain (such as in climate simulations), MC mountains would appear smoother and flatter, and their effects on the DC would be smaller. Based on the results of this study, they would provide a lesser disruption to the formation of large land-locked MCSs, and, consequently, they would provide a greater barrier to MJO propagation over the MC.

Chapter 5

SEASONAL AND INTERANNUAL VARIABILITY OF MJO PROPAGATION AND THE MARITIME CONTINENT BARRIER EFFECT

5.1 Abstract

The MJO's organized convection induces large-scale heating that can influence atmospheric conditions downstream, both in and away from the tropics. The downstream influences of the MJO can depend on the latitudinal position of MJO convection, and the atmosphere can respond very differently to a heating source that is centered on the equator compared to ones in the Northern or Southern Hemispheres. Traditional MJO indices (e.g., RMM) can estimate the general longitudinal information of the MJO but cannot provide information on the latitudinal position or extent of MJO convection. The large-scale precipitation tracking algorithm (LPT) allows for direct tracking of MJO convection in time and space, and can provide additional details of tracked MJO events, such as its exact location, and spatial extent in both zonal and meridional directions.

The main objective of this study is to better understand seasonal and interannual variability of MJO convection, especially on its initiation locations and meridional variability of the MJO eastward propagation. The LPT algorithm is used to track MJO events in 20 years of satellite-observed precipitation, and we explore how MJO propagation and the MC barrier effect to MJO propagation vary at seasonal and interannual time scales. We find that MJO propagation shows strong seasonality in meridional propagation, with December-May MJOs propagating through the MC along and south of the equator, and June-November MJOs bypassing the MC to the north. Interannual modes of variability that control the distribution of SST in the Indo-Pacific warm pool (ENSO, IOD) can affect the location of MJO initiation. During La Niña (-IOD), when the MC experiences positive SST anomalies, MJO events tend to initiate closer to the MC than when negative SST anomalies are present over the region. QBO, associated with stratospheric variability, has little effect on the location of MJO initiation, but we find that MJO activity is enhanced during the QBO-E phase.

The seasonal and interannual variability in the background atmospheric state over the MC modulates the strength of the MC barrier effect. Seasonally, the barrier effect is strongest in the spring (March – May, when MJOs propagate through the MC along the equator), and

it is weakest during peak monsoon seasons. The barrier effect also shows distinct variability at interannual time scales, with states that enhance the ascending branch of the Walker circulation over the MC (La Niña, -IOD) promoting more MJO activity over the MC and resulting in a weaker barrier effect. Additionally, MJO events that start closer to the MC are more resilient to the MC barrier effect than MJO events that initiate farther west.

5.2 Introduction

Active Madden-Julian oscillation (MJO) events are associated with intense convection organized on a large scale that propagates eastward from the tropical Indian Ocean (IO) to the West Pacific ocean (WP) through the Maritime Continent (MC). The MJO convective envelope consists convective systems at multiple scales, but is often organized into westward-propagating mesoscale convective systems (MCSs; Chen et al., 1996). A major way in which convection affects the general circulation is through the release of latent heat, and the multi-scale convection within the MJO convective envelope results in the heating throughout the troposphere (Barnes et al., 2015). The heating associated with the MJO can excite Rossby waves that propagate into the midlatitudes and modify atmospheric conditions away from the tropics (Matthews et al., 2004).

An idealized global circulation model study of MJO impacts by Zheng and Chang (2019) found that the midlatitude response to MJO-generated heating in the tropics varies with MJO characteristics. MJO events that propagate slower and last longer excite a stronger extratropical response compared to their shorter-lived and faster-propagating counterparts. They also find that the MJO events that remain at a consistent intensity through most of their lifetime excite weaker midlatitude responses than MJO events that vary in intensity, and that strongest midlatitude teleconnections occur when the MJO is over the WP (RMM Phase 6).

A significant drawback that studies on MJO impacts face is that they treat the MJO as a statistical quantity instead of as a physical phenomenon. MJO indices such as the Real-Time Multivariate MJO Index (Wheeler and Hendon, 2004, RMM;) abstract the MJO into its departure from the long-term global mean outgoing longwave radiation, lower- and upper-tropospheric zonal winds. This commonly-used definition of the MJO is used in most studies on MJO impacts and prediction, but they cannot provide details on where exactly the MJO convection is located. Specifically, an MJO event that propagates along the equator will most likely produce different impacts than an MJO event that propagates north of

the equator. However, since most studies focus on the predictability of the MJO through RMM or intraseasonal filtering, the information on latitudinal variability of the MJO is not available.

While studies examining the effects of the seasonal cycle, El Niño-Southern Oscillation (ENSO), the Indian Ocean dipole (IOD), and the Quasi-Biannual oscillation (QBO) already exist, they tend to use traditional indices to identify MJO events, and miss out on the spatial variability of individual MJO events. Lu and Hsu (2017) describe the strong seasonal cycle of MJO activity, showing that the frequency, strength, and lifespan of MJO events are all reduced during the boreal summer and autumn, compared to winter and spring. Tam and Lau (2005) show that ENSO modulates MJO activity, with El Niño events increasing the frequency of MJO propagation toward the central Pacific, and reducing the propagation speed of MJO in the Pacific ocean. Wilson et al. (2013) find that MJO activity is enhanced over the IO and MC during negative IOD events, when the eastern IO is anomalously warm compared to the western IO.

The variability of ENSO and IOD have a direct impact on the MJO as they vary the sea surface temperature patterns in the Indo-Pacific warm pool. The QBO's modulation of MJO activity is more indirect, as it affects the conditions in the tropical upper troposphere. Martin et al. (2021) find that during boreal winter, MJO events are stronger, slower-propagating, and longer-lived during the easterly phase of the QBO, compared to when the stratospheric winds are westerly, but only for boreal winter. The mechanisms by which QBO affects MJO are often linked to the QBO-mediated stability changes in the upper troposphere, but the link between QBO and MJO is not reproduced in numerical models.

In this study, we use large-scale precipitation tracking (LPT; Kerns and Chen, 2016, 2020) to track MJO events in 20 years of satellite-derived precipitation observations. As MJO events are tracked directly through precipitation, the tracking algorithm provides the evolution of each individual MJO event in both time and space. In this way, we can examine the spatial variability of MJO convection, and how it is related to the seasonal cycle and modes of interannual variability. We can also directly assess the strength of the MC

barrier to MJO propagation, and we show how this changes seasonally and under different climatological background states.

5.3 Methods and Data

5.3.1 MJO Tracking and Identification

To identify MJO events, we apply the large-scale precipitation tracking algorithm (LPT; Kerns and Chen, 2016, 2020) to 20 years of satellite-derived precipitation observations. LPT allows us to track large-areas of high three-day precipitation accumulations in the global tropics and midlatitudes, and has been used to identify MJO events by isolating tracked features that propagate eastward and persist for a minimum of seven days. Kerns and Chen (2020) have used LPT to create a 20-year climatology of MJO events using the Tropical Rainfall Measuring Mission's (TRMM) Multisatellte Precipitation Analysis (TMPA; Huffman et al., 2007) version 7 to identify 215 MJO systems. In this study, we apply the same algorithm TRMM TMPA's successor, the Global Precipitation Mission's (GPM) Integrated Multi-Satellite Retrievals for GPM (IMERG Huffman et al., 2019), using version 6B from the algorithm's final processing run. IMERG is available in 30-minute increments at a spatial resolution of 0.1°, and we use a 20 year period from June 2000 to June 2020. The higher resolution presents a benefit when analyzing diurnal variability of precipitation over the MC, as in Chapter 4.

To match the method of (Kerns and Chen, 2020), we first re-grid IMERG to match the resolution of TRMM TMPA - 3-hourly at a spatial resolution of 0.25°. As LPT tracking accumulates precipitation for three days, and uses spatial smoothing, this coarsening of IMERG data does not affect the results of MJO tracking, but significantly speeds up the time it takes to process 20 years of observations. The LPT tracking on IMERG was first run with a three-day precipitation accumulation threshold of 12 mm day^{-1} (as in Kerns and Chen, 2020), which identified 274 events in the 20-year time period. This number is significantly higher than the 215 events identified in TRMM TMPA from June 1998 to June

2018 by Kerns and Chen (2020), in part because IMERG produces higher rain rates for heavy precipitation events. To better match the number of events identified by Kerns and Chen (2020), the three-day precipitation accumulation threshold was raised to 13 mm day^{-1} for this study, which identified 212 MJO events over the global tropics.

One important benefit of using LPT to track MJO events instead of traditional MJO indices such as the RMM is that LPT tracking provides a way to spatially separate active MJO convection from its environment for each 3-hourly frame of the 20-year dataset. MJO events show a significant amount of variability from one event to another in terms of size and propagation pathways (Section 5.4 Kerns and Chen, 2020), and LPT tracking allows us to spatially follow the evolution of each individual MJO event and its impacts. In addition, as LPT tracks MJO events based on absolute precipitation, it is directly correlated with MJO-induced heating which is responsible for downstream impacts of the MJO.

5.3.2 MJO Frequency Composition

The 212 MJO events identified by LPT tracking provide a large sample size for analysis. But considering each event as an individual entity makes data compositing difficult, as some MJOs initiate in one month and terminate in another - which could be in a different season, or a different state of interannual variability as defined by common climate indices (e.g., ENSO). In this case, the resulting MJO numbers and composites can be sensitive to which time we choose to represent the entire MJO - whether that is its initiation, termination, or median time.

To get around the sensitivity to MJO time when compositing MJO events, I instead separate each event into it's 3-hourly frames. Then, if a given frame falls within a certain month, season, or climate state, there is no ambiguity about its timestamp. In addition, this significantly increases the sample size for comparison - an average MJO event persists for around 23 days, providing 187 frames for compositing. Compositing is done either month-by-month, seasonally for three-month periods (e.g., December-January-February, DJF), or according to indices of interannual variability. Then, data are either plotted as the number

of days a particular location is within the MJO, or they are normalized by each composite's maximum value to enable comparison other composites.

During composition, we leave out the central and eastern Pacific MJO events (there are 19, labelled as Other in Fig. 5.4), as our analysis focuses on the Indo-Pacific warm pool.

5.3.3 Indices of Interannual Variability

Interannual variability indices considered in this study include El Niño-Southern Oscillation (ENSO), the Indian-Ocean Dipole (IOD), and the Quasi-Biannual Oscillation (QBO). Data for the Oceanic Niño Index (ONI, a measure of ENSO), the Dipole Mode Index (DMI, a measure of IOD), and the QBO have been downloaded from NOAA's Physical Sciences Laboratory. Each index is available at a monthly frequency.

ONI is calculated as a three-month running mean of the NOAA ERSST.V5 SST anomalies in the Niño3.4 region (5°S-5°N, 120-170°W) based on changing base period which consists of multiple centered 30-year base periods. These 30-year base periods are be used to calculate the anomalies for successive 5-year periods in the historical record. An ONI value less than -0.5 represents a La Niña event, which identifies cold SST anomalies in the central and eastern Pacific. An ONI value greater than $+0.5$ represents an El Niño, with warm SST anomalies in the center and eastern Pacific, and a value between -0.5 and $+0.5$ is considered ENSO-neutral.

DMI represents the anomalous SST gradient between the western equatorial IO (10°S-10°N, 50-70°E) and the south-eastern equatorial IO (10°S-0°N, 90-110°E). When DMI is positive, waters in the western IO are warmer than in the eastern IO (near the MC), and when DMI is negative, waters near the MC are warmer than in the west. To match the processing of ONI, the entire time series is smoothed using a three-month running mean, and +IOD events are defined for DMI > 0, and negative events for DMI < 0.

QBO index is calculated from the zonal average of the 30mb zonal wind at the equator from the NCEP/NCAR Reanalysis. Similarly as for DMI, QBO index is smoothed using a three-month running mean before positive values are associated with westerly winds in the

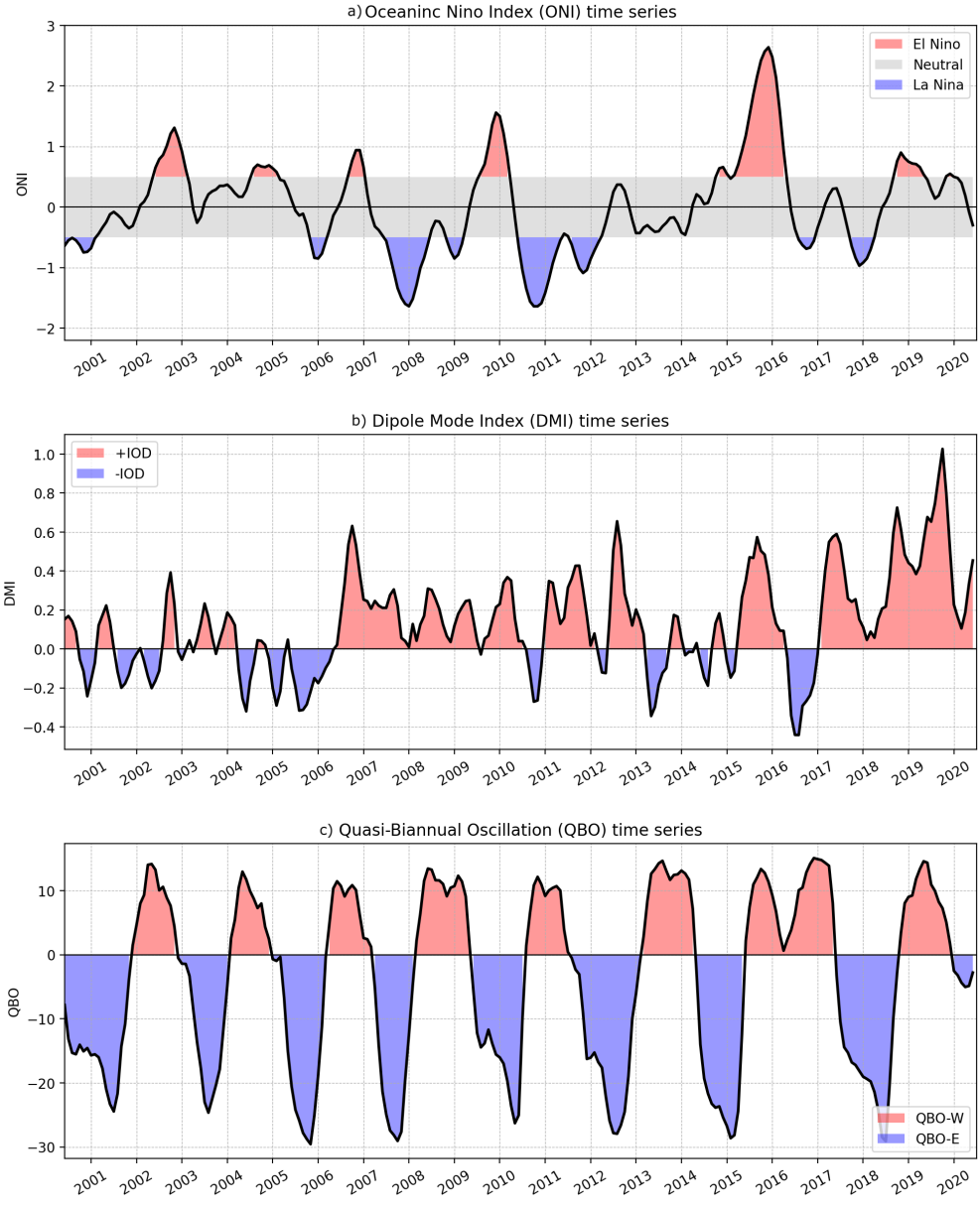

Figure 5.1: Time series of indices of seasonal and interannual variability for the 20-year period of analysis. a) Oceanic Niño Index (ONI) that represents the phase of ENSO; b) Dipole Mode Index (DMI) that represents the phase of IOD; c) Quasi-Biannual Oscillation (QBO). The highlighted red, grey, and blue regions represent times during which a given index is considered positive, neutral, and negative, respectively.

tropical stratosphere (QBO-W), and negative values are associated with easterlies (QBO-E).

Fig. 5.1 shows time series of ONI, DMI, and QBO indices for the 20-year time period of analysis, with highlighted positive regions (red), negative regions (blue), and neutral regions (grey) of each index. The 20-year time period includes six El Niño events and 8 La Niñas, and 9 positive and 8 negative QBO events. IOD is much more variable, with some events lasting years, while other events last only a few months. While the average ONI value is around 0, the average DMI for the 20-year period is significantly positive (0.42) and we see many more, and stronger +IOD events than −IOD events. The average QBO index is negative (-0.34) as periods of easterly stratospheric winds (QBO-E) have much greater amplitude than the periods of westerly stratospheric winds (QBO-W). When we separate the 20-year periods into the positive, neutral, and negative phases of these three indices, we get the following distributions with respect to time:

- ENSO: El Niño 23.7%; neutral 50.2%; La Niña 26.1%.
- IOD: +IOD 68.5%; −IOD 31.5%.
- QBO: QBO-W 52.7%; QBO-E 47.3%.

5.3.4 Quantification of the MC Barrier Effect

The MC barrier effect has been quantified in a number of different ways by a number of studies. Using ray-tracing to identify MJO events (Zhang and Ling, 2017) based on intraseasonally-filtered precipitation anomalies, an ending longitude of 150° is frequently chosen to denote the separation between MJO events blocked by the MC (which terminate before it) and crossing MJO events (which propagate past it). Using the RMM index, MC barrier effect is often inferred from the weakening of the RMM amplitude between phases 4 and 6, when the MJO is over the MC and over the western Pacific, respectively (e.g., Burleyson et al., 2018). Even Kerns and Chen (2020), who identify MJOs using LPT tracking, define a longitude of 130° to separate the blocked events from the crossing ones, only taking into account the location of the MJO centroid.

The MJO's precipitation is distributed throughout the entire convective envelope identified by LPT, and half of the MJO convective area extends ahead of the centroid; if we want to evaluate the MJO's impacts, the MJO's convective extent should also be considered. To estimate the strength of the MC barrier effect on MJO propagation in this study, we design a new metric for its quantification that is based on MJO activity - the amount of time for which an MJO convective envelope is present within a given region. We define three regions for estimating MJO activity: in the Indian Ocean (IOA, 20°S-20°N, 80-100°E), in the Maritime Continent (MCA, 20°S-20°N, 115-135°E), and in the West Pacific (WPA, 20°S-20°N, 150-170°E). The regions are marked in black in Fig. 5.2, which shows them overlaid on top of MJO frequency for the subset of MJO events that initiate over the IO (the MJO events for which the centroid begins west of 100°E). Only the IO-starting MJO events are used in the quantification of the MC barrier effect in Section 5.6, and before processing, we further remove the MJO events that terminate before their centroid reaches 90°E, as those events dissipate before reaching the MC. This leaves us with a total of 112 MJO events that being in the IO and propagate into/through the MC.

MJO frequency, the number of days for which a given location is within the convective envelope of an MJO event, is taken as a proxy for MJO activity. The MJO frequency is integrated within individual MJO activity regions (values are listed in the top left corners of each panel in Fig. 5.2), and the ratios are calculated between IOA and the other regions to quantify the change in MJO activity from one region to the next. There are benefits to estimating MJO activity within a given region instead of a cutoff value for the centroid location: our estimation of the strength of the MC barrier effect accounts for the entire MJO convective envelope. Additionally, the regions were chosen so they cover the latitude range through that captures the majority of MJO convective envelopes from all regions; our results are also not very sensitive to changing the longitudinal extent of MJO activity regions.

R_{MC} is the ratio between MJO activity over the MC and MJO activity over the IO, and its value quantifies how much MJO activity has changed over the MC. R_{WP} is the ratio between MJO activity over the WP and MJO activity over the IO. On its own, R_{WP} is not

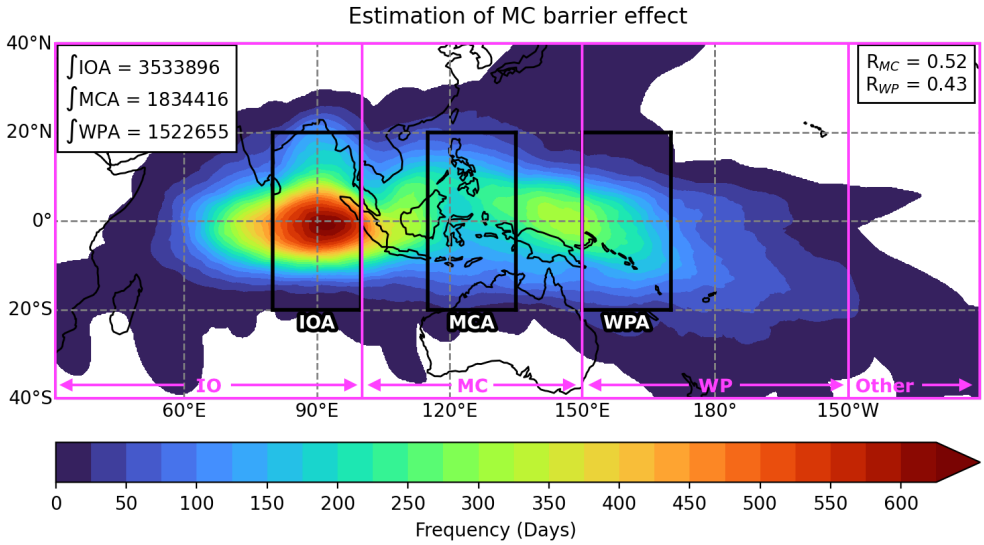

Figure 5.2: MJO frequency for IO-starting MJO events. Magenta outlines denote the IO, MC, and WP regions, and black outlines define IOA, MCA, and WPA - the MJO activity regions defined to esimate the strength of the MC barrier effect on MJO propagation. The numbers on the top left are the sum of all pixels within individual activity boxes (in days). The numbers on the top right are the ratios of sums for two boxes, R_{MC} and R_{WP}, that quantify the MC barrier effect on MJO propagation.

useful for measuring the MC barrier effect, but in relation to R_{MC}, it quantifies how MJO activity changes after the MC (e.g., do MJOs continue to weaken, or re-intensify as they enter the WP). A breakdown of R_{MC} values and their meanings:

- $R_{MC} = 0$: MJO dissipates before any of its convection reaches the MCA region.
- $0 < R_{MC} < 1$: MJO weakens over the MC (WP).
- $R_{MC} = 1$: no change in MJO activity between IO and MC.
- $R_{MC} > 1$: MJO strengthens over the MC, no evident MC barrier effect.

5.4 MJO Precipitation

Based on climatological precipitation, the Indo-Pacific warm pool is one of the strongest convective regions in the world. It lies at the crossroads of multiple atmosphere and ocean phenomena that contribute to the large amounts of precipitation and its variability. These include ENSO and the associated ascending branch of the Walker Circulation, the inter-tropical convergence zone (ITCZ), the shifting between the Australian and Southeast Asian monsoon, the MJO, and strong diurnal circulations induced by land-sea contrast and terrain.

Fig. 5.3 shows the 20-year summary of total and MJO-related precipitation. The 20-year precipitation climatology (Fig. 5.3a) clearly shows enhanced precipitation over the islands of the MC, the ITCZ (north of the equator in the Pacific and south of it in the IO), and the South Pacific convergence zone (SPCZ), as well as monsoonal enhancement of precipitation in the Bay of Bengal. When only MJO-associated precipitation is considered (Fig. 5.3b), the climatological ITCZ features and enhanced land precipitation are no longer present. Instead, two precipitation maxima associated with the MJO: one in the eastern equatorial IO with an extension into the Bay of Bengal (this is seasonal), and a very strong signal in the WP which is collocated with the SPCZ. Over the MC, MJOs preferentially enhance precipitation over water rather than over land. In most of the MC, more than 10% of total precipitation within a 20 year period comes from MJO events, and in certain places, the portion of total precipitation that comes from MJO events exceeds 40% (Fig. 5.3c). Even in regions of highest MJO activity, an MJO event is present in a given location over the Indo-Pacific warm pool for just over 12% of the time, which highlights how intense MJO convection is compared to all other precipitation over the MC.

Fig. 5.3 illustrates that compared to the IO or WP, precipitation is a lot more spread out over the MC. This is partly due to the disruption of the MJO by islands of the MC, but is also a result of different propagation pathways that MJO events take through the MC in different seasons (more in Section 5.5.1).

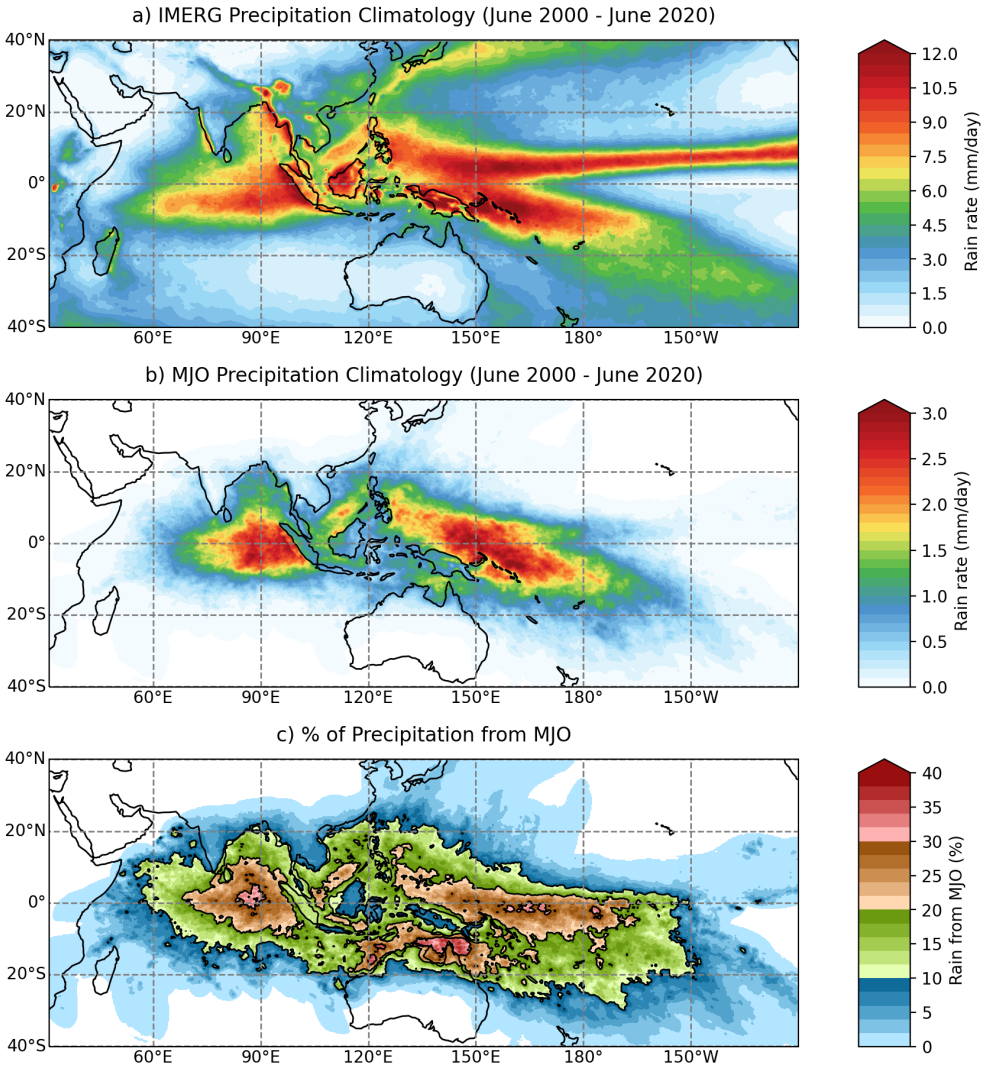

Figure 5.3: a) 20-year (June 2000 - June 2020) precipitation climatology from IMERG (mm day−1), b) average precipitation within MJO convective envelopes for the same time period (mm day−1, but with a reduced range), and c) the percentage of total precipitation that is produced within MJO events (%).

5.5 Variability of the MJO and its Eastward Propagation

LPT tracking over the 20-year period from June 2000 - June 2020 produces a total of 212 MJO events. To get an idea of where these MJOs are, and when they form, they are separated into four geographical regions, for which some statistics are shown in Fig. 5.4. The regions categorize the locations of the MJO centroid locations over the IO (30-100°E), MC (100-150°E), WP (150-210°E) and other (beyond 210°E).

113 of the events (53%) initiate over the IO (30-100°E), with 25 of those terminating before reaching the MC (Fig. 5.4a). The remaining MJOs propagate over the MC (100-150°E), where 56 new MJO events are initiated (26%), but 57 events dissipate, illustrating the MC barrier effect. 87 MJO events continue to propagate into the western Pacific, where 23 new events form (11%), but 94 events (45%) terminate. Unlike the MC barrier effect, the WP termination of MJO events is mostly due to the MJOs tracking into the SPCZ and slowly running out of fuel for precipitation. The MJO events that initiate outside of IO, MC, and WP tend to be located in the eastern Pacific, and the terminating events include the termination of those events, as well as the termination of some MJO events that manage to propagate really far east from WP.

5.5.1 Seasonal Variability

Fig. 5.4b shows the seasonal variability of MJO centroids, but now instead of counting individual events, we are counting the number of days for which the MJO centroid is in a given region - as MJO events can propagate through multiple regions.

The weakly shaded bars represent the amount of time an MJO centroid is in a given geographical region, with the number at the top indicating the portion of the 20-year period with an MJO. Though we only ever see a single MJO event at any one time, it is interesting that an MJO event exists somewhere in the global tropics for 45% of the time (within the 20-year data record), with the majority of that time in the IO, MC, and WP regions. Though the remainder of the world sees the initiation of 19 MJO events, those tend to be short-lived

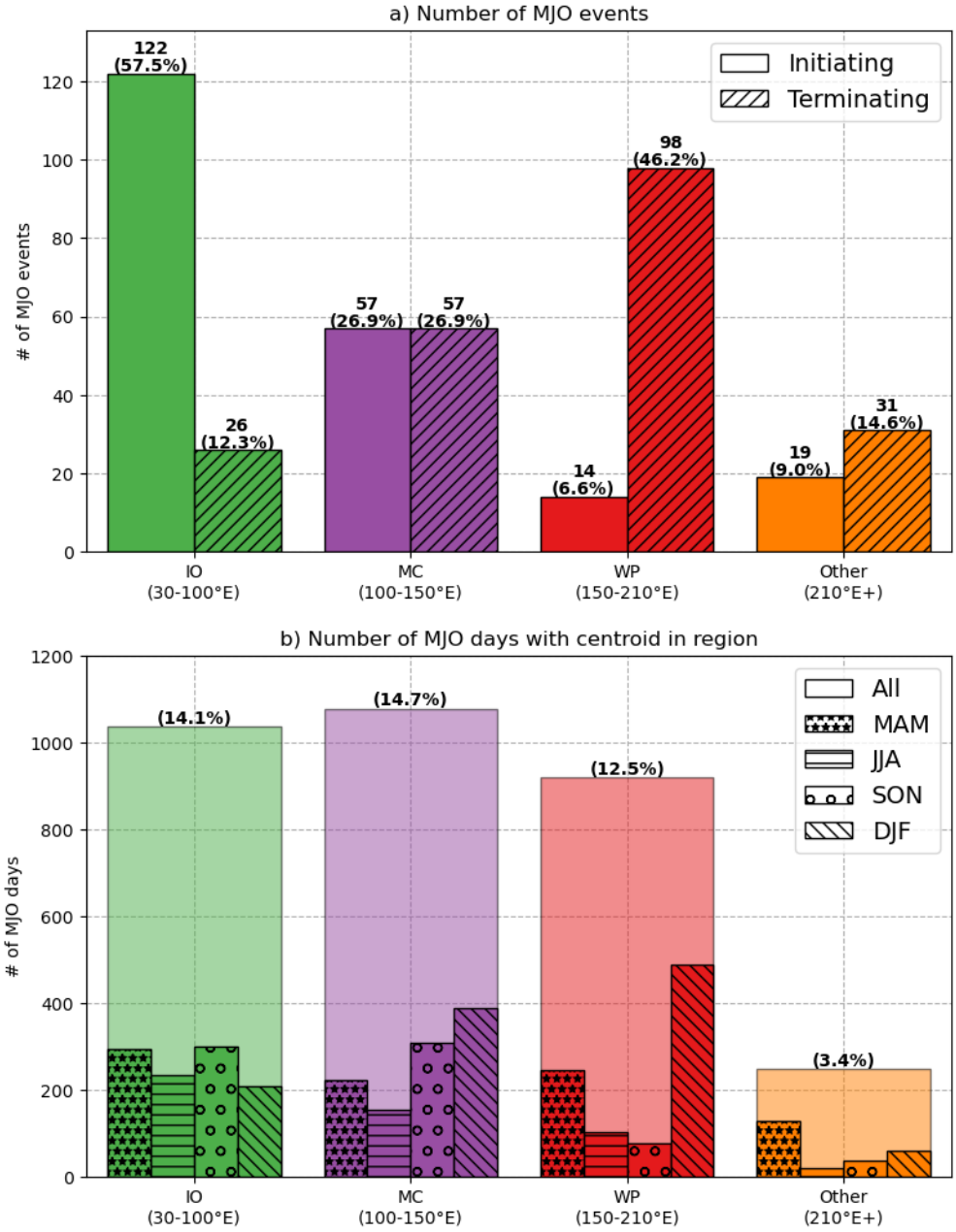

Figure 5.4: Distribution of MJO centroid locations among different regions. a) Number of MJO events that initiate (solid) or terminate (hatched) in a given geographical region (there are 212 MJO events, and each column is topped with the number of events in that category, and with what percentage of all MJO events that number represents. b) MJO-centroid frequency within a given geographic region separated into 3-month-long seasons.

and represent a small portion compared to both the IO-MC-WP, and the total time period.

Each of the geographical regions shows a distinct pattern of seasonal variability with respect to what time of year MJOs are present - those are denoted by differently-hatched bars in Fig. 5.4b. Over the IO, the number of MJO days doesn't seem to vary strongly with season, though there are slightly more during the monsoon transition seasons (September-November, SON, and March-May, MAM) than during boreal winter (December-February, DJF) or summer (June-August, JJA). Over the MC, the number of MJO days increases from June - February, and then rapidly drops between March and May, while most of the MJOs in the WP occur in boreal winter (DJF), and there are very few in the summer (JJA). East of 210°E, the number of MJO events gradually increases from June through May, with the largest number of MJO days between March and May. We do not consider those events from this point forward.

In addition to seasonal variability within each of these regions, there is also a strong latitudinal variability in MJO propagation across the MC. The maps of MJO frequency across the four seasons (MAM, JJA, SON, DJF) are shown in Fig. 5.5, top to bottom. with the left portion showing MJO density, and the right portion showing the median MJO propagation pathway for each of the seasons. MJO activity is lower June-November (Fig. 5.5a, b), and strongest December-February (Fig. 5.5c). Between December and May, the MJOs propagate through the MC along, and slightly south of the equator - this is what is thought of as the canonical MJO. Between June and November, the MJOs tend to bypass the MC to the north. In the summer (JJA) MJO's turn back toward the equator in the WP, while in the autumn (SON), the MJOs remain north of the equator. The representation of variability of MJO propagation across and around the MC is important for representation and prediction of MJO impacts, which depend on the location of the large-scale diabatic heating associated with MJO precipitation. In the summer, when the MJOs are propagating to the north, the strong source of heating is located solidly in the northern hemisphere, while it remains nearer the equator and transitions into the southern hemisphere in the winter.

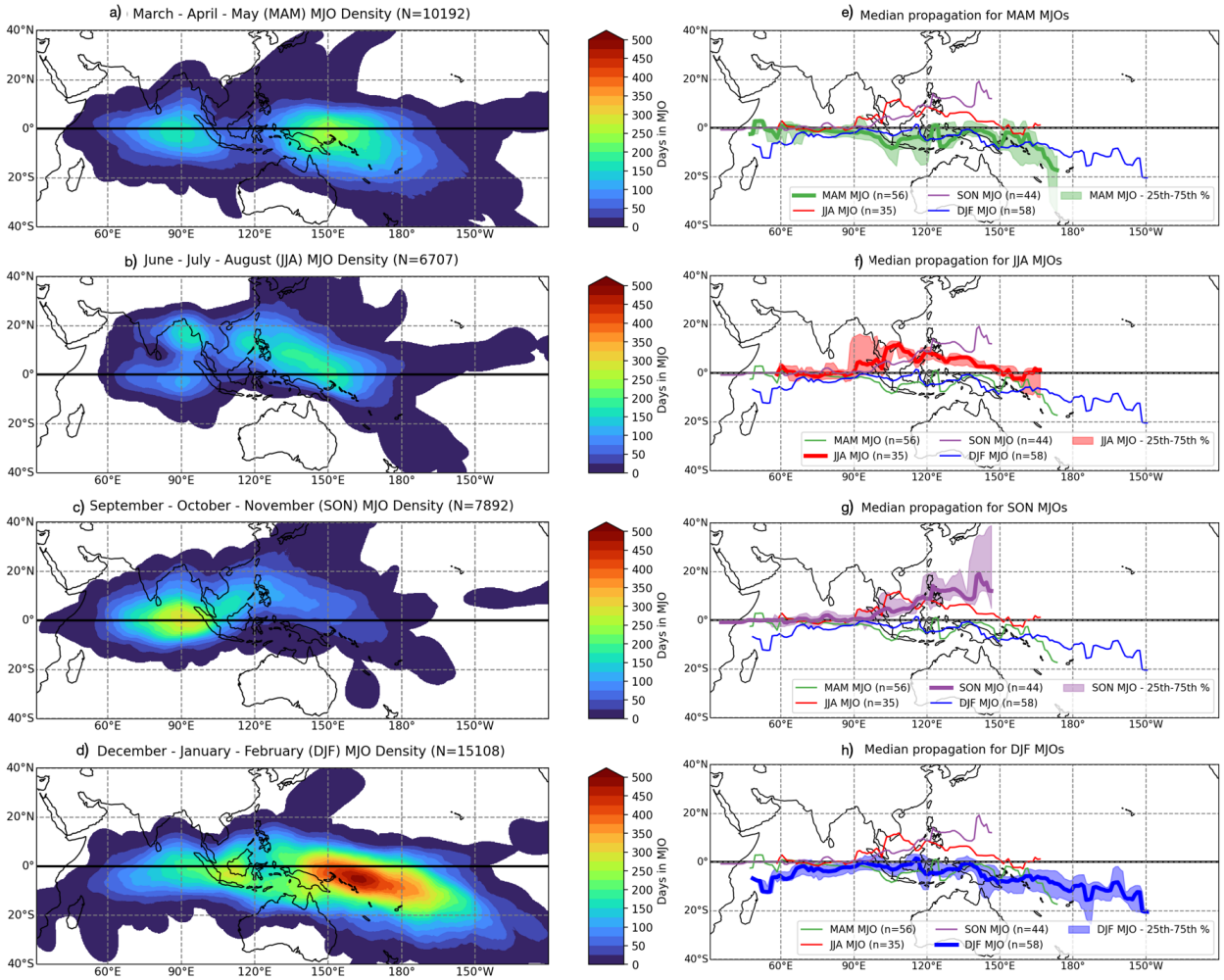

Figure 5.5: MJO frequency - the number of days for which a given location is inside the MJO within the 20-year period for different seasons (a-d) and their corresponding median propagation pathways (e-h). a) March - May (MAM) - transition between Australian and south-east Asian monsoon; b) June - August (JJA) - boreal summer, monsoon over south-east Asia; c) September - November (SON) - transition between south-east Asian and Australian monsoon; d) December - February (DJF) - boreal winter, monsoon over Australia and MC.

5.5.2 Interannual Variability - ENSO, IOD, and QBO

In addition to strong seasonal variability described in the previous section, we also examine the effects of interannual variability on MJO propagation. Fig. 5.1 shows time series for three indices of interannual variability that we explore due to their adjacency to the Indo-Pacific warm pool region. ENSO, and its IO counterpart, the IOD, regulate the sea surface temperatures in the Pacific and Indian Oceans, respectively. Through this regulation, they also modulate the position of the ascending branch of the Walker circulation, and can promote precipitation amplification or suppression over the Indo-Pacific warm pool - they can affect MJO propagation from the surface. The QBO is a stratospheric phenomenon that could affect the MJO from the top, and a number of studies have found a strong connection between the two, noting that the easterly phase of the QBO (QBO-E) favors stronger MJO activity (e.g., Klotzbach et al., 2019).

MJO frequency varies throughout the year, but MJO events do not seem to favor one particular phase of ENSO, IOD, or QBO. Rather, when we compare the frequency distribution of occurrence of any of the indices to the frequency distribution of the MJO for the same time period, MJO events are present throughout the entire spectrum of background conditions. However, the background states do affect where the MJO events form, and how they propagate eastward.

The MJO composites associated with the background states is shown in Figs. 5.6, 5.7, and 5.8 for ENSO, IOD, and QBO, respectively. All figures are laid out in the same manner, with MJO composites showing the positive (El Niño, +IOD, QBO-W), neutral (for ENSO), and negative (La Niña, -IOD, QBO-E) states in the top panels, followed by the spatial difference between the positive and negative states and the median tracks for the opposing states. All composites with MJO frequency are normalized to the highest value of each sample to reduce the difference due to the number of times within each sample. For an easier comparison of relative effects of each of the background states, the scale on the difference plots is identical for the three figures. Among the three indices, ENSO has the strongest effect on the nature

of MJO propagation, and the effect of QBO is the weakest. For a more quantitative view, Fig. 5.9 shows box-and-whisker plots of the MJO centroid starting and ending longitudes, duration, and average area for the three indices for the IO-starting MJO events.

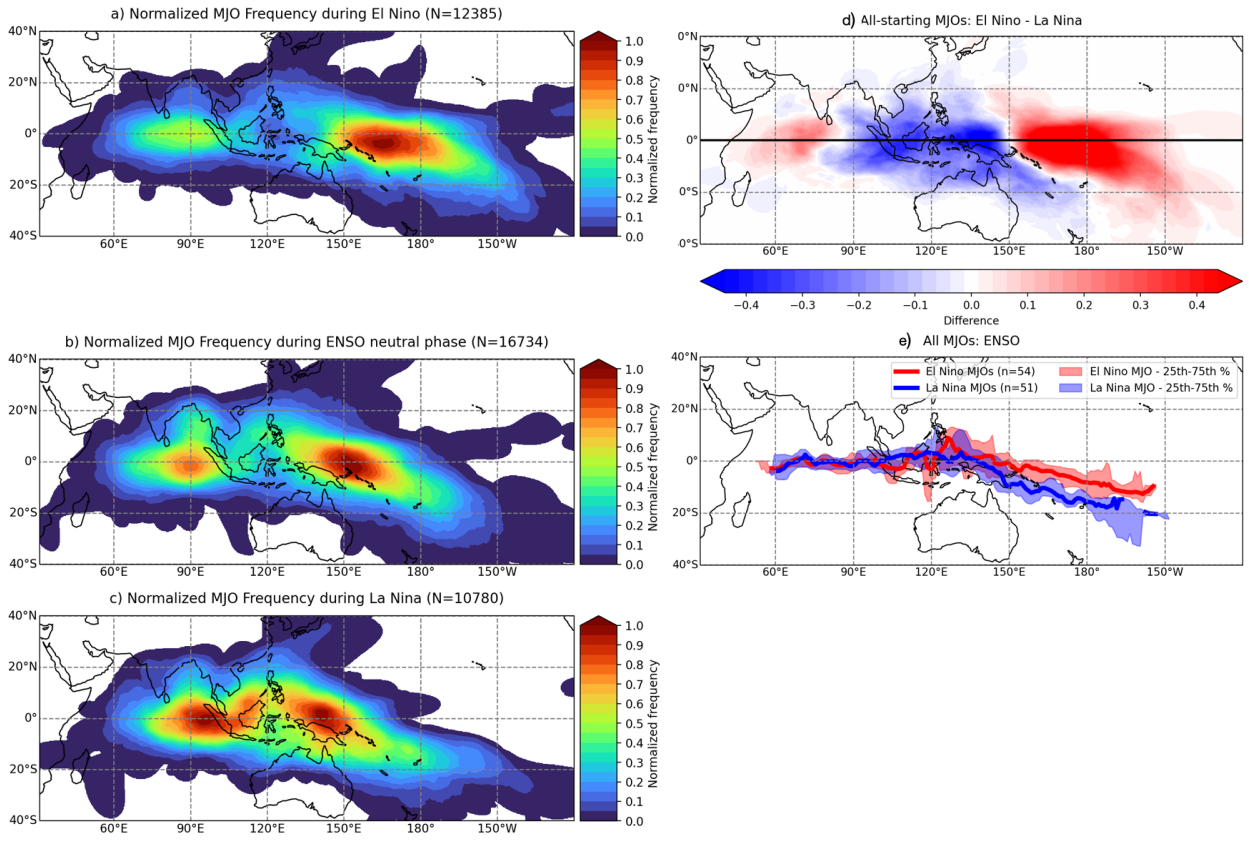

Figure 5.6: Normalized MJO frequency in ENSO phases: a) +ENSO (El Niño), b) ENSO-neutral, c) −ENSO (La Niña); the difference between El Niño and La Niña cmposites in d) frequency and e) median propagation pathways. Each composite is normalized by the higest MJO frequency in the sample, and the number of samples within each phase is listed in the title.

The background state of ENSO has a strong effect on MJO propagation, and narrates the longitudinal range of MJO activity (Fig. 5.6). During El Niño months, MJO activity is concentrated over the WP, with a smaller activity center in the equatorial IO (Fig. 5.6a). During La Niña months, MJO activity is evenly distributed over the IO, MC, and WP

regions (Fig. 5.6c). The maps show all MJO events, so the maximum over the WP is a combination of MJO events that start anywhere in the Indo-Pacific warm pool. But when only IO-starting MJO events are considered, we see that during La Niña, MJO events both initiate and terminate slightly to the east of MJO events during El Niño (Fig. 5.9a, b). And though La Niña MJO events tend to grow larger than El Niño MJOs, the latter last longer, which indicates that IO MJO events during El Niño propagate eastward at a slower rate (Fig. 5.9c, d). Additionally, the WP MJO activity maximum in Fig. 5.6a mostly comes from MC and WP-starting MJO events, as more than half of IO-starting MJO events dissipate before the centroid reaches the WP region.

The change in MJO characteristics due to the background ENSO phase can be explained by the eastward migration of the ascending branch of the Walker circulation. During La Niña, the ascending branch of the Walker circulation over the MC gets amplified, increasing the background upward motion. This helps promote precipitation in the region (the WP MJO activity maximum in Fig. 5.6c is just east of the MC). During El Niño, the warmer SSTs, the ascending branch of the Walker circulation, and the South Pacific Convergence Zone (SPCZ) all shift eastward, and so do the MJO propagation tracks and the maximum in MJO activity over the WP (Fig. 5.6a).

The influence of background state of IOD is of a lesser magnitude than that of ENSO, and the most prominent differences are confined to the IO. During +IOD, MJO activity is balanced between the IO and WP regions (Fig. 5.7a), while it is more prominent over the WP during −IOD (Fig. 5.7b). −IOD events are defined as warm SST anomalies in the south-eastern equatorial IO compared to the western IO, and we see that reflected in MJO activity - under −IOD, MJO activity is slightly enhanced over the southern MC, while it is stronger in +IOD everywhere else over the IO (Fig. 5.7c). There are also smaller differences north of the MC and in the WP south of the equator, where +IOD shows more MJO activity.

This spatial pattern is confirmed when we see IO-starting MJO events shifted eastward during −IOD (Fig. 5.9a). In terms of formation and termination, −IOD acts in a similar manner to a La Niña background state, as both concentrate warmer water closer to the MC,

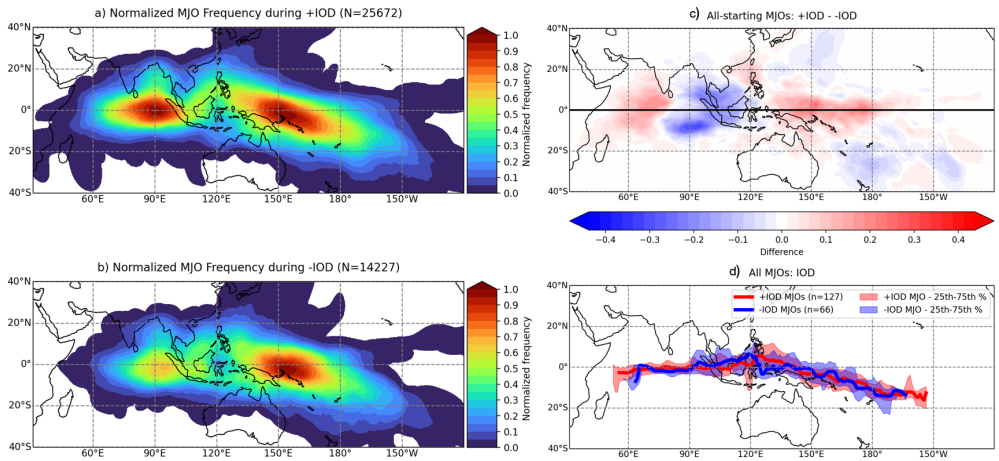

Figure 5.7: Normalized MJO frequency in IOD phases: a) +IOD (warm SST anomaly in eastern IO), b) −IOD (warm SST anomaly in western IO), and the difference between +IOD and -IOD cmposites in c) frequency and d) median propagation pathways. Each composite is normalized by the higest MJO frequency in the sample, and the number of samples within each phase is listed in the title.

just in different ocean basins. −IOD MJO events also tend to be slightly larger, and have a larger variability in duration than MJO events during +IOD. Aside −IOD MJOs starting slightly farther east on average, there is little difference in propagation pathways between the +IOD and −IOD MJO events.

The influence of background QBO state on MJO propagation is of a lesser magnitude still. Composited for all months of the year (Fig. 5.8c), QBO-W events are correlated with enhanced MJO activity in the northern equatorial IO and equatorial WP, but QBO-E MJOs prevail elsewhere.

To summarize key results from this section, background states that vary on seasonal and interannual time scales (e.g., the seasonal cycle, ENSO, IOD, and QBO) can have a significant impact on the MJO's eastward propagation. The seasonal cycle controls whether MJO events cross the MC along the equator in boreal winter and spring, or bypass it to the north in boreal summer and autumn (Fig. 5.5). The background ENSO and IOD states

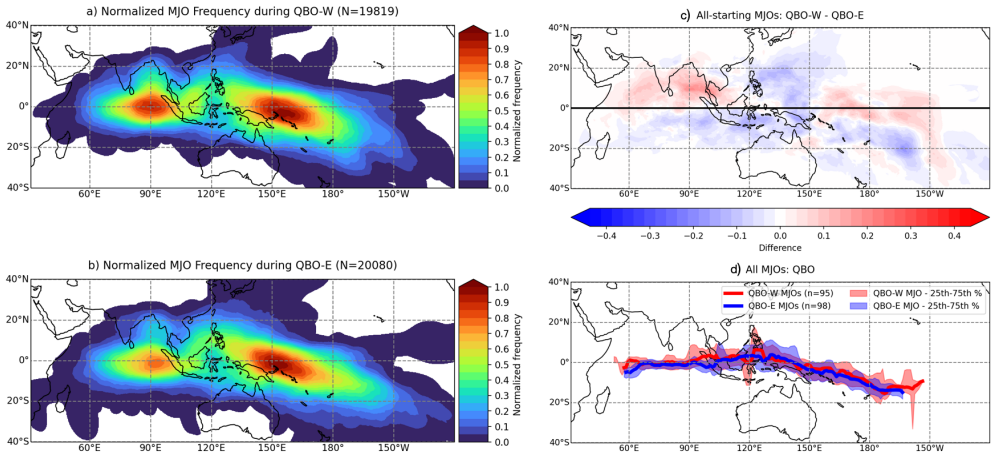

Figure 5.8: Normalized MJO frequency in QBO phases: a) QBO-W (westerlies in the stratosphere), b) QBO-E (easterlies in the stratosphere), and the difference between QBO-W and QBO-E composites in c) frequency and d) median propagation pathways. Each composite is normalized by the higest MJO frequency in the sample, and the number of samples within each phase is listed in the title.

can modify how much MJO events are confined to the vicinity of the MC - during La Niña (−IOD), MJO events tend toward initiation in the eastern IO and dissipation in the WP, but during El Niño (+IOD), they start farther westward and end farther eastward (Fig. 5.6). La Niña events also show more latitudinal variability over the MC. QBO, which is a measure of stratospheric variability, shows very little effect on MJO initiation and propagation pathways across the MC, but it can modulate MJO activity - this tends to be enhanced during QBO-E.

5.6 MC Barrier Effect and its Variability

In this section, we want to evaluate how the strength of the MC barrier effect changes seasonally, and with the change of background states due to ENSO, IOD, and QBO. Fig. 5.2 illustrates the method we use for the evaluation of the MC barrier effect strength using MJO activity over the IO and WP boxes to quantify the reduction in MJO activity in the MC. When all 112 MJO events that initiate over the IO are combined, the R_{MC} ratio is 0.52,

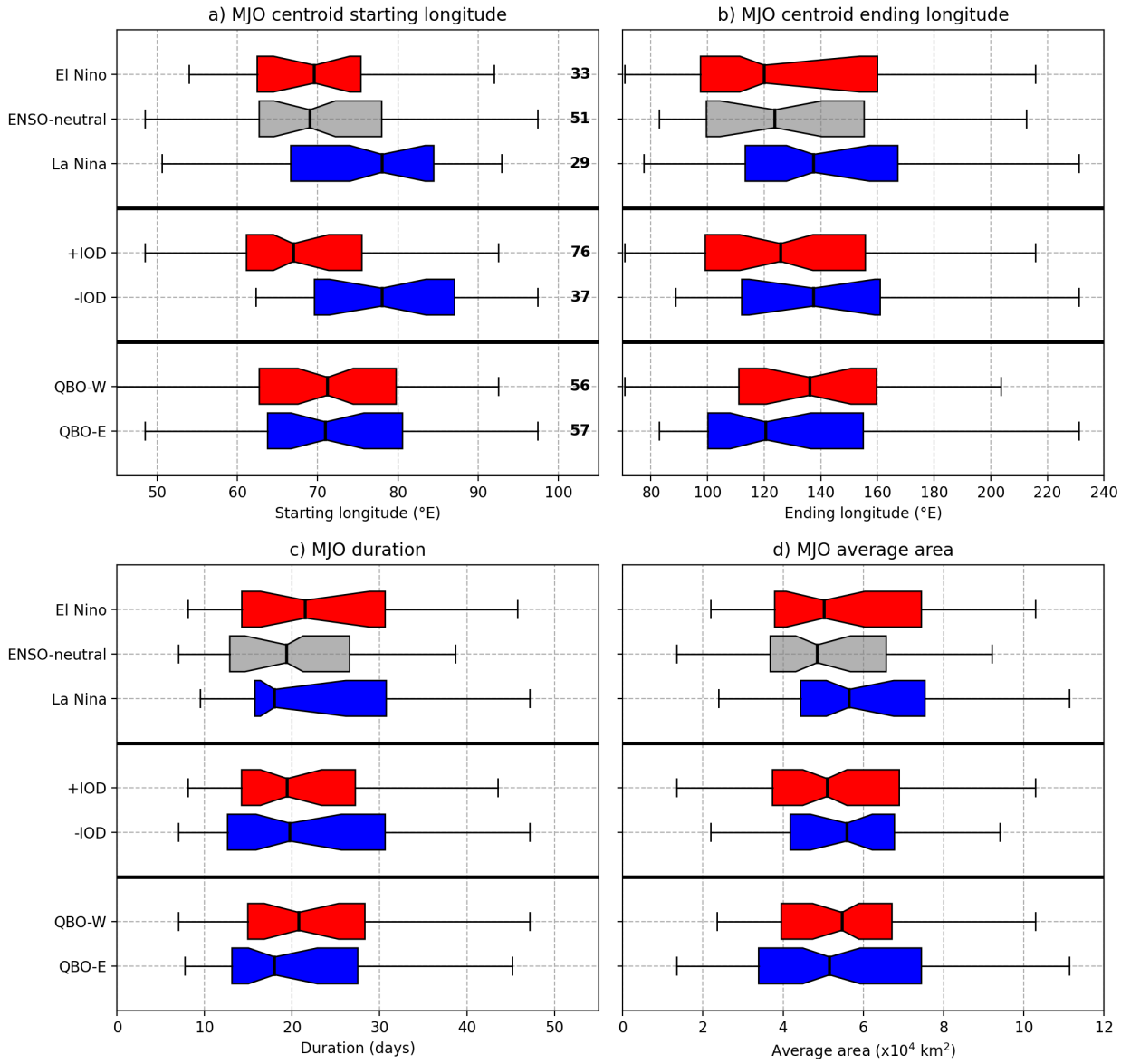

Figure 5.9: Box-and-whisker plots of a) MJO centroid starting longitude (°E), b) MJO centroid ending longitude (°E), c) MJO duration (days), and d) MJO average area (x10^4 km^2) for phases of ENSO, IOD, and QBO. These distributions only include the IO-starting MJO events. Red colors correspond to positive indices, blue to negative indices, and, in case of ENSO, grey corresponds to the neutral state. The numbers on the right side of a) indicate the number of events in each sample.

which means that, on average, the MC barrier effect reduces MJO activity over the MC by 48%. We use the same method to evaluate the MC barrier effect for each individual MJO event to quantify the event-to-event variability of the barrier effect, and we also apply it to different background states to see whether some states have a stronger barrier effect than others.

The strength of the MC barrier effect for individual MJO events varies significantly from one event to another. Table 5.1 shows the number (and percentage) of MJOs that dissipate, weaken, or strengthen over the MC, as well as their seasonal and interannual variability. Fig. 5.10 shows the sorted distribution of R_{MC} for each of the 112 MJO events that initiate in the IO and propagate into the MC, as well as the average area and total propagation speed for each individual MJO event. There is a linear correlation between R_{MC} and MJO area, as well as between R_{MC} and MJO propagation speed. Based on Fig. 5.10, larger and faster-propagating MJO events tend to be less affected by the MC barrier effect. Note that when calculating the total propagation speed for each MJO event, both the zonal and meridional propagations are considered; when only considering the zonal propagation speeds, the correlation with R_{MC} is much weaker. When comparing the strengthening MJO events (R_{MC} ¿ 1) and the dissipating MJO events ($R_{MC} = 0$), there are also some notable differences in where MJOs form.

MJO events that strengthen over the MC (blue in Fig. 5.11) tend to initiate closer to the MC and have much larger areas; this pattern is similar to MJO activity associated with a La Niña background state (Figs. 5.6c, 5.9). In fact, 11 of 24 strengthening events happen during La Niña and only 5 during El Niño (Table 5.1. There are also proportionally more strengthening MJO events during QBO-E than QBO-W. The 20 MJO events that completely dissipate before reaching the MC region (dark red in Fig. 5.11) tend to initiate farther west, have smaller overall areas, and have shorter durations than other MJO events. This pattern is similar to MJO activity associated with a +IOD background state (Figs. 5.7a, 5.9), and 16 out of 20 MJO events that dissipate before reaching the MC occur during +IOD.

Seasonally, the MC barrier effect is stronger in monsoon transition seasons (MAM, SON)

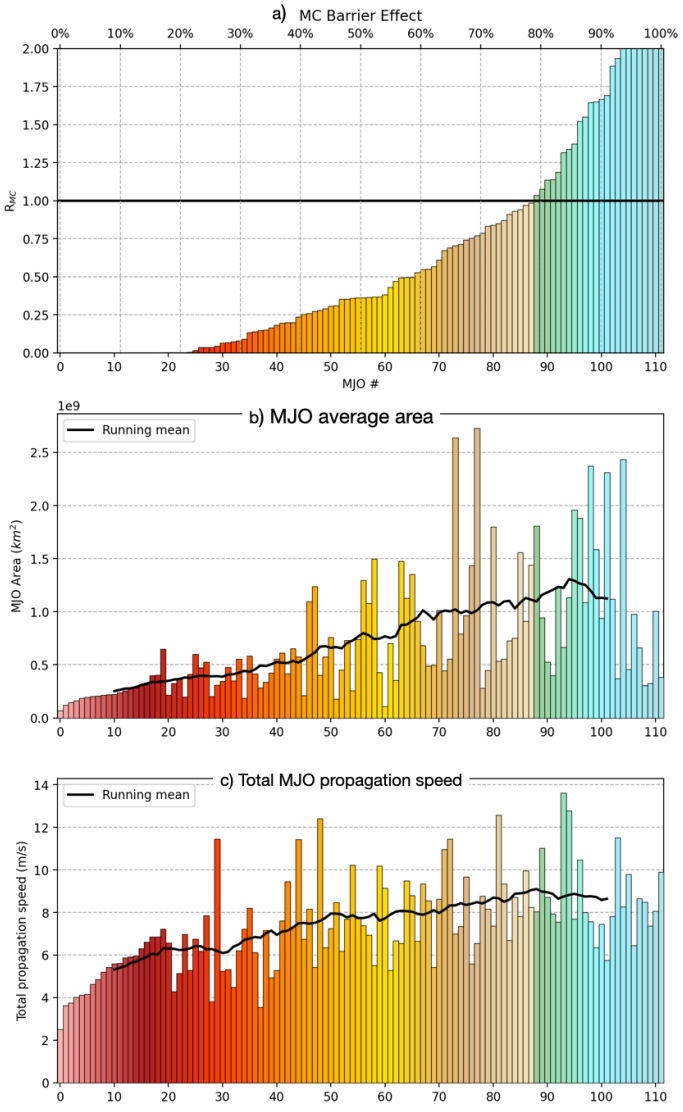

Figure 5.10: a) Sorted distribution of R_{MC} for individual MJO events, with shading on all panels corresponding to the value of R_{MC}. b) The average MJO area (km^2) for each MJO event. c) The average propagation speed for each individual MJO - this is the vector sum of zonal and meridional components of MJO propagation. Thick black lines in b) and c) show the smoothed running mean to highlight a trend. The lower the R_{MC} ratio is, the stronger the MC barrier effect is to MJO propagation. R_{MC} ratios > 1 indicate strengthening of MJO activity over the MC, and no barrier effect - those are highlighted in blue.

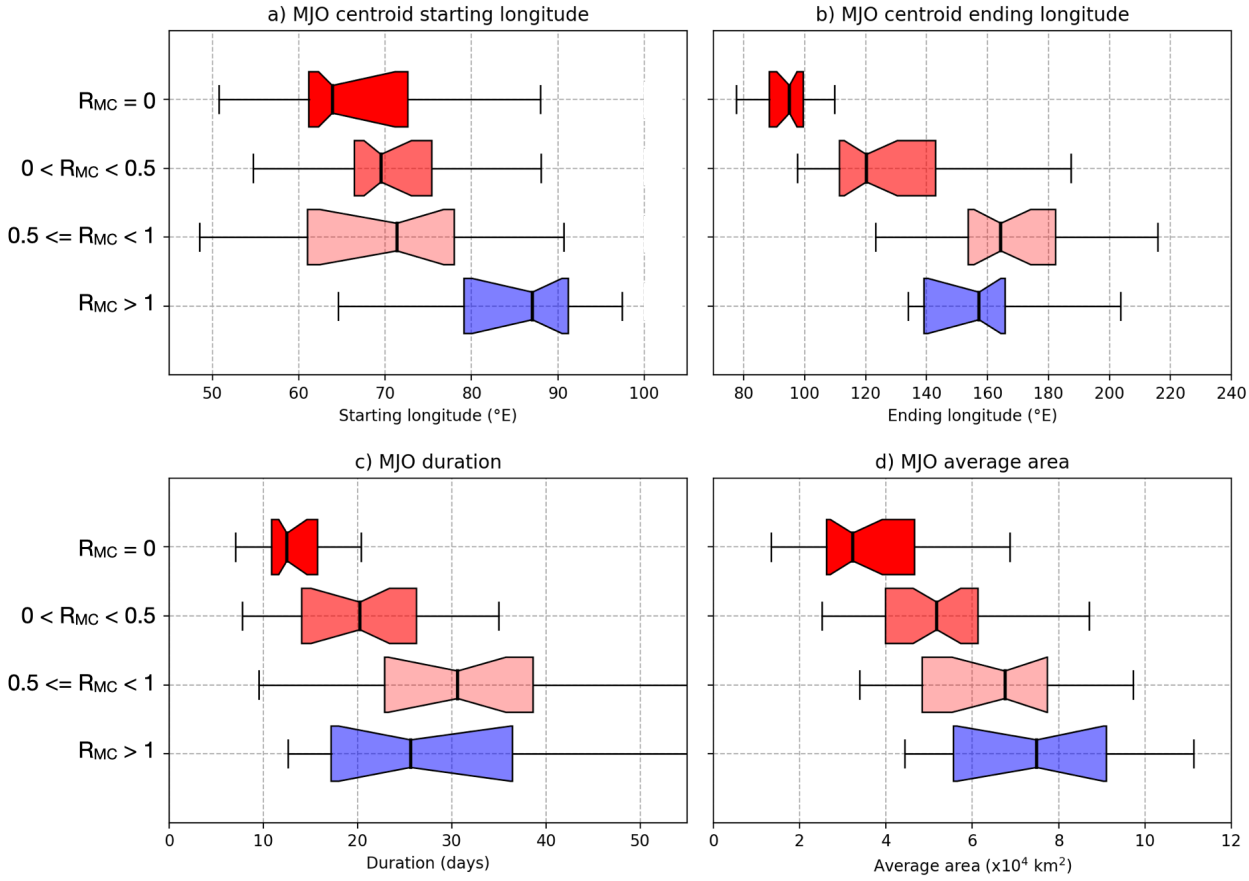

Figure 5.11: As in Fig. 5.9, box-and-whisker plots of a) MJO centroid starting longitude (°E), b) MJO centroid ending longitude (°E), c) MJO duration (days), and d) MJO average area (x10^4 km^2). Red color shading is proportional to the strength of the MC barrier effect, with dark red denoting MJO events that dissipate before reaching the MC box; blue is for MJO events that strengthen over the MC.

	$R_{MC} = 0$ event	$0 < R_{MC} < 0.5$ event	$0.5 \leq R_{MC} < 1$ event	$R_{MC} > 1$ event	Total
All	20	46	22	24	112
MAM	7	11	6	4	28
JJA	3	8	4	6	21
SON	8	17	5	5	35
DJF	2	10	7	9	28
El Niño	5	12	4	5	26
ENSO-neutral	12	21	9	8	50
La Niña	3	13	9	11	36
+IOD	16	37	15	18	86
−IOD	4	9	7	6	26
QBO-W	5	25	13	9	52
QBO-E	15	21	9	15	60

Table 5.1: Number of all IO-starting MJO events that dissipate, weaken, or strengthen over the MC, separated by season (MAM, JJA, SON, DJF) and background states of ENSO, IOD, and QBO. There are 112 IO-starting MJO events. Regions used for evaluating the MJO activity and the MC barrier effect are outlined in black in Fig. 5.2.

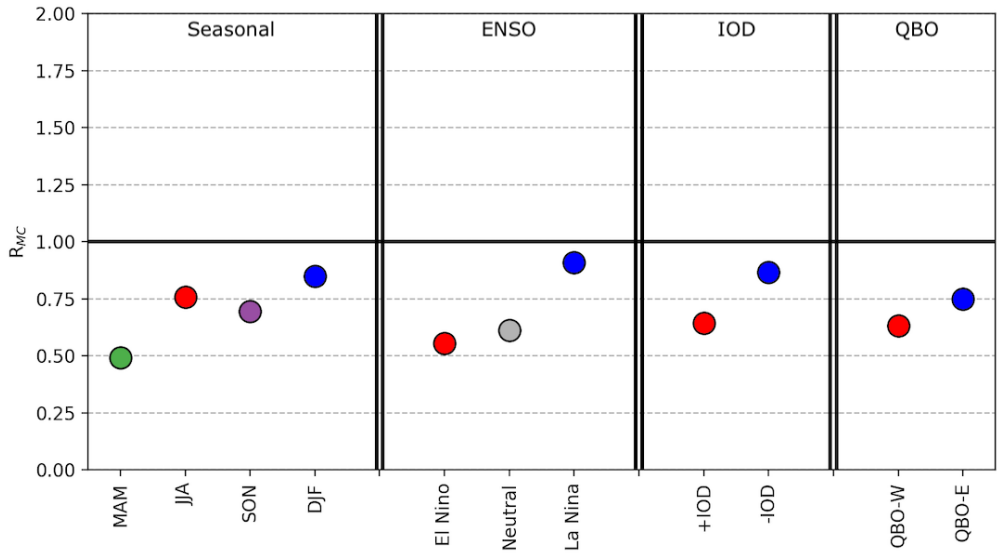

Figure 5.12: Variability of MC barrier effect strength by season (MAM, JJA, SON, DJF) and background states of ENSO, IOD, and QBO.

than in peak monsoon seasons (JJA, DJF), but there is a large discrepancy between MAM and SON. The strongest barrier effect occurs in boreal spring (MAM), when MJOs propagate through the MC along the equator (Fig. 5.5a, e), while the barrier effect is weaker in boreal autumn, when MJOs bypass the MC to the north (Fig. 5.5c, g). When considering the background states of interannual variability, the negative phases (La Niña, −IOD, QBO-E) coincide with a weaker MC barrier effect (Fig. 5.12b), and positive phases (El Niño, +IOD, QBO-W) coincide with a stronger MC barrier effect. As in MJO activity composites in Section 5.5.2, the modulation is most prominent with ENSO, and weakest with QBO.

5.7 Summary and Conclusions

In this study, we explore the variability of MJO's eastward propagation from the Indian Ocean to the Maritime Continent and the West Pacific, and the variability of the MC barrier effect to MJO propagation. 20 years of satellite-derived precipitation observations are used to identify 212 MJO events from June 2000 to June 2020 using the large-scale pre-

cipitation tracking algorithm (LPT; Kerns and Chen, 2016, 2020). Variability of the MJO centroids and convective envelopes, and their eastward propagation pathways across the MC is analyzed by compositing MJO convective envelopes at seasonal scales and across three indices of interannual variability that affect conditions near the MC: ENSO, IOD, and QBO. We establish a metric for the quantification of the MC barrier effect that allows us to evaluate the relative activity of the MJO over the IO, MC, and WP regions, and investigate how the MC barrier effect changes based on seasonal and interannual modes of variability.

The key results presented can be summarized as follows:

1. MJO propagation shows strong seasonality in the meridional variability of propagation. In the IO, MJOs tend to form near the equator, but propagation pathways separate over the MC and WP (Fig. 5.5). MJOs between December and May propagate along (and slightly south of) the equator, and between June and November, they bypass the MC to the north.

2. Interannual modes of SST variability (ENSO and IOD) can modulate the location of MJO initiation, while stratospheric forcing (QBO) affects MJO activity, but not its initiation. During La Niña (-IOD), MJOs tend to form farther east in the IO (closer to the MC) than during El Niño (+IOD).

3. MC barrier effect is weakest during peak monsoon seasons (JJA, DJF), and shows dependence on MJO properties such as the MJO's area and starting longitude. MJOs that start closer to the MC experience a weaker barrier effect, as do MJOs that are larger in size.

4. Large-scale seasonal and interannual variability modulates MJO propagation and the strength of the MC barrier effect. But there is still large variability within a season or given background state, indicating that the local effects of the MC (e.g., organization of land-locked convection) that play an important role.

LPT allows us to track the spatial extent of MJO precipitation with time, and examine the variability in MJO convective area, and its zonal and meridional variability - metrics which traditional MJO indices such as RMM cannot provide. Climatologically, MJO convection is concentrated in two distinct regions over the Indo-Pacific warm pool - one over the eastern equatorial IO, and a second one in the equatorial WP. The MC separates the two regions of peak MJO frequency, and the reduction in frequency over the MC can be attributed to two factors. First, the MC barrier effect, which is a result of the disruptive influence of land in the path of the MJO. Second, MJO events in the IO and WP are concentrated near the equator, but over the MC, MJO propagation exhibits significant seasonal variability. In boreal winter, when the monsoon is active over Australia, the MJOs propagate across the MC along the equator, but in boreal summer, MJOs are affected by the Southeast Asian monsoon and bypass the MC to the north before curving back toward the equator and track into the South Pacific convergence zone (Fig. 5.5)

The analyzed modes of interannual variability (ENSO, IOD, and QBO) were chosen because they directly affect the background atmospheric state over the Indo-Pacific warm pool. ENSO and IOD are defined by variability of equatorial sea surface temperature gradients in the Pacific and Indian Oceans, respectively. They affect the local conditions from the bottom through the modulation of sea surface temperatures, and by modification of atmospheric circulations associated with them, such as the Walker circulation. QBO is defined by zonal winds in the stratosphere and is strongest at the equator, so it would be affecting the background atmospheric state from above. When compositing MJO events across positive and negative phases of each of these indices, we find that ENSO provides the strongest modulation of MJO activity, and QBO the weakest.

The ENSO and IOD background states behave in a similar way, and they preferentially affect the longitudinal range of MJO activity. +IOD is associated with positive SST anomalies in the western IO, and during those periods, MJO events tend to initialize (and terminate) westward of MJOs during the −IOD phase, when the warm SST anomalies are located over the eastern IO (Figs. 5.7, 5.9). Through phases of ENSO, from El Niño to La Niña, the

MJO tracks shift eastward, with La Niña events initiating closer to the MC, and propagating farther into the WP. The forcing provided by QBO variability is present at the top of the troposphere, and does not modulate MJO initiation. However, once an MJO has developed, the QBO-E phase shows increased MJO activity compared to QBO-W, most likely due to enhancing deep convection associated with the MJO.

The strength of the MC barrier is calculated for each individual MJO event, and we find that out of 112 MJO events, 80% of MJOs weaken, with 40% weakening by more than 75%, and 20% dissipating completely. Using this metric for quantifying the strength of the MC barrier effect, we find that there are distinct differences between MJO events that dissipate before reaching the central MC, and ones that strengthen over the region and do not feel a barrier effect. Early-dissipating MJO events initiate farther west in the IO (median longitude is 63°E) and they remain significantly smaller in area compared to the strengthening MJO events that initiate farther east in the IO (median longitude is 87°E), Fig. 5.11. The early dissipating events are strongly correlated with +IOD events, and the strengthening events predominantly occur during La Niña conditions. The general results obtained from the MC barrier effect metric agree with previous studies on the topic, reproducing the strong barrier effect described in the spring (e.g., Li et al., 2020).

The novel parts of this study include the quantification of meridional variability of the MJO, which cannot usually be identified by traditional MJO indices such as the RMM. With the additional information provided by LPT, we show the strong latitudinal dependency of MJO propagation across seasons. Additionally, though our zonal propagation speeds agree with the average of 5 ms^{-1} determined by previous studies, this propagation shows little relationship to the strength of the MC barrier effect. But when the meridional component of MJO propagation are included, the average MJO propagation speed increases to 7.3 ms^{-1}, and faster-propagating MJO events experience less weakening over the MC (Fig. 5.10)

But the propagation of individual MJO events determines the local and global impacts of the MJO. Locally, MJO events produce extreme precipitation - they have been linked to severe flooding events over the MC, and my own work has shown that 50% of all trop-

ical cyclones that form over the IO spin off of a preceding MJO event (tracked through precipitation). Globally, the MJO's impacts are excited by the heating source associated with large-scale precipitation, which will have significantly different impacts depending on whether it is located near the equator (e.g., in boreal winter) or away from it (e.g., in boreal summer), whether it weakens over the MC (as most events do), and whether it can re-intensify over the WP (e.g., during El Niño), or not (e.g., during La Niña).

Chapter 6
SUMMARY AND CONCLUSIONS

The overarching goal of this dissertation was to better understand the physical processes affecting the eastward propagation of the MJO from the Indian Ocean to the Pacific Ocean across the Maritime Continent. We focused our analysis on the representation of MJO precipitation, as the precipitation is responsible for diabatic heating of the atmosphere that link the tropical MJO to its extratropical impacts.

This work studies MJO propagation through both local physical processes that take place within an MJO event, and through the modulation of the background atmospheric and oceanic state in relation to seasonal and interannual variability. In Chapters 2 - 4, we used a combination of observations and regional high-resolution atmosphere-ocean coupled modeling to expose important factors that, when represented accurately, can improve MJO prediction, as well as physical mechanisms behind them. In Chapter 5, we used 20 years of satellite-derived precipitation observations to identify MJO events and describe the variability of MJO propagation and quantify the strength and variability of the MC barrier effect from seasonal to interannual scales

In Chapter 1, we introduced four questions that motivated our work, and our attempt at answering them has been described in the following chapters:

Chapter 2: How are MJO initiation and eastward propagation affected by the representation of multi-scale convective systems?

Chapter 3: How is MJO eastward propagation affected by atmosphere-ocean coupling?

Chapter 4: How is MJO eastward propagation affected by the islands of the MC?

Chapter 5: What are the modes of variability of MJO eastward propagation across the MC?

The following sections present a short summary of key results found within each chapter.

6.1 Effects of Model Resolution and Moist Physics on Atmospheric Boundary Layer and MJO Precipitation

In Chapter 2, we discuss how different model resolutions, and the associated representation of moist physical processes can affect MJO initiation and eastward propagation over the IO. Atmosphere-ocean coupled model simulations (12-km grid spacing) with two different convective parameterizations (CP) were compared to each other and to their cloud-permitting counterparts with no convective parameterization in the innermost domain with 4-km grid spacing. Model simulations are evaluated against satellite-derived and field campaign observations of precipitation, surface winds, and aircraft-released dropsondes from the DYNAMO field campaign.

Key result: Cloud-permitting resolution is better able to represent the various scales on which precipitation occurs within the MJO (convective, mesoscale, and large-scale organization), and how convection interacts with the marine boundary layer.

- At low (12 km) grid resolution, the choice of CP is the determining factor for the simulation of MJO precipitation and eastward propagation. The Tiedtke CP produced an eastward propagating MJO while the Kain-Fritsch CP did not (Figures 2.3b, c).

- Using different CP in low-resolution simulations results in a vastly different atmospheric ABL structure that has a major impact on MJO dynamics (Figs. 2.7-2.9). Kain-Fritsch CP produced an overly saturated, cloudy boundary layer that is decoupled from the free troposphere, which is prohibitive to large-scale westerly winds from descending to the surface and the maintenance of large-scale convection (Fig. 2.7g, l). Tiedtke CP produced an over-mixed ABL with a weak surface wind and precipitation signal (Fig. 2.7h, m).

- With convection-permitting (4 km) resolution, explicit moist physics and no CP, model simulations improve the structure of convective systems and the structure of the ABL (Figs. 2.7i, j). This results in a more realistic vertical structure of winds and moisture in the troposphere (Fig. 2.9), as well as improved MJO precipitation, eastward propagation, and post-MJO suppression of precipitation (Fig. 2.2).

6.2 Impacts of Atmosphere-Ocean Coupling on the Upper Ocean and MJO Propagation

In Chapter 3, we analyze how the eastward propagation of the MJO over the IO changes due to atmosphere-ocean coupling and associated processes of air-sea interaction. Cloud-permitting (4-km grid spacing) model simulations in uncoupled (constant SST) and coupled (dynamically-evolving SST) configurations are compared against satellite-derived and field campaign observations of precipitation, surface winds, air-sea fluxes, and buoy observations from the DYNAMO field campaign.

Key result: Strong surface winds and intense precipitation associated with the MJO induce sea surface temperature and upper ocean cooling. Reduced air-sea fluxes create an environment unfavorable for sustaining intense precipitation, contributing to the MJO's eastward propagation.

- Coupled atmosphere-ocean model reproduces the MJO eastward propagation while large-scale precipitation in the uncoupled model remains anchored in the IO (Fig. 3.3).

- Upper-ocean cooling induced by the MJO is essential in reducing excessive and prolonged precipitation over the IO and aiding in MJO's eastward propagation (Fig. 3.2.

- Improved representation of air-sea flues reduces model biases in precipitation, surface winds, air-sea fluxes, as well as the bias in upper ocean temperature, all of which improve the MJO prediction (Fig. 3.8).

6.3 Land-Locked Convection as a Barrier to MJO Propagation across the Maritime Continent

In Chapter 4, we assess the sensitivity MJO propagation across the MC to the MC barrier effect induced by land-sea contrast and topography over the region. An atmosphere-ocean coupled model simulation at cloud-permitting resolution (4-km grid spacing) with realistic topography is compared to idealized simulations in which we flatten the MC topography and remove land-sea contrast by replacing MC islands with shallow ocean. The comparison among the simulations informs us on whether physical processes associated with the MC barrier effect on MJO propagation are dominated by topography or by land-sea contrast.

Key result: Over the MC, diurnal convection over land can merge into mesoscale convective systems (MCSs) which suppress convection over surrounding waters, over which the MJO prefers to propagate through the region. MCSs grow larger and more intense when MC topography is flattened, which enhances the MC barrier effect. Forced lifting along topographical features disrupts the growth of MCSs enough that the MC barrier effect is reduced when realistic terrain is represented.

- Land and land-sea contrast weaken the MJO and disrupt its propagation over the Maritime Continent (Fig. 4.6).

- Land-sea contrast of MC islands induces a strong diurnal cycle with strong land-locked convection in the afternoon (Figs. 4.8, 4.9).

- Mountains are less disruptive to MJO propagation than larger and stronger land-locked convective systems that form over land without them (Figs. 4.11, 4.12).

6.4 Seasonal and Interannual Variability of MJO Propagation and the Maritime Continent Barrier Effect

In Chapter 5, we step away from modeling and processes that affect MJO propagation on a local scale, and focus on how the background state of the tropical atmosphere and ocean over

the Indo-Pacific warm pool can modulate the large-scale characteristics of MJO propagation. MJO events are identified and tracked using the LPT algorithm for 20 years (June 2000 - June 2020) of satellite-derived precipitation observations. The variability in the eastward propagation of MJO convection/precipitation is described under influences of the seasonal cycle and background states of interannual variability related to ENSO, IOD, and QBO, with a focus on MJO initiation and meridional propagation. We develop a metric for the strength of the MC barrier effect that can quantify how MJO activity is affected by its passage from the IO, through the MC, and into to the WP, and examine the variability of the MC barrier effect under seasonal and interannual background states.

Key result: MJO precipitation experiences significant seasonal and interannual variability in both the zonal and meridional directions, and both seasonal and interannual climate variability affect the strength of the MC barrier effect to MJO propagation.

- The seasonal cycle is the strongest modulator of MJO activity and the meridional variability of MJO propagation. In boreal winter (DJF, Australian monsoon season), MJO activity is highest and MJO events propagate through the MC along the equator, with convective activity slightly biased to the Southern Hemisphere. In boreal summer (JJA, Southeast Asian monsoon season), MJO activity is strongly reduced compared to winter, and MJOs bypass the MC to the north before tilting back toward the equator (Fig. 5.5).

- The background states of ENSO and IOD modulate the SST patterns over the Pacific and Indian Oceans, and can shift low-level zonal wind convergence regions closer to the MC (during −IOD in IO, La Niña in WP) or farther away from it (during +IOD in IO, El Niño in WP). This can provide background low-level ascent in different locations relative to the MC, and affects the position and strength of the ascending branch of the Walker circulation; those factors modulate where MJO events tend to initiate and how far they can propagate (Figs. 5.6-5.9). The modulation of MJO propagation by QBO is less direct, shows large seasonal variability, and its mechanisms remain uncertain.

- From one MJO event to another, the MC barrier effect is highly variable: some events completely dissipate, most weaken, but a small number of show strengthening over the MC (Fig. 5.10). We show a dependency of the strength on the MC barrier effect on MJO area, starting longitude, and propagation speed, with larger and faster MJOs that initiate close to the MC experiencing a weaker barrier effect. Seasonally, the MC barrier effect is weakest during peak monsoon seasons (JJA and DJF) and is strongest during boreal spring, when average MJO activity is reduced by 50% or more over the MC (Fig. 5.12). The strongest interannual variability of the MC barrier effect is associated with different phases of ENSO, with the weakest effect during La Niã and the strongest effect during ENSO-neutral background conditions.

6.5 Future work

This dissertation focuses on the processes affecting the eastward propagation of MJO precipitation/convection through local physical processes associated with air-sea-land interaction, and through large-scale modulation of the background atmospheric and oceanic state on seasonal and interannual scales. The advantage of being able to identify the spatial location and temporal variability of MJO precipitation gives us a significant advantage in studying the impacts of the MJO compared to MJO indices that cannot determine the spatial location of MJO heating.

With an understanding of how the zonal and meridional propagation of MJO convection vary from event to event, and on different temporal scales, we can open new avenues for:

1. Analyzing how the background states over the MC during different seasons and phases of interannual variability combine to cause changes in the MC barrier effect.

2. Studying the MJO's downstream influences relative to the exact location (in both longitude and latitude) of MJO-induced diabatic heating, and whether those change based on MJO properties such as the size of its convective envelope, duration, propagation speed, and its initiation and termination.

BIBLIOGRAPHY

Abbs, D. J. and Physick, W. L. (1992). Sea-breeze observations and modelling: review. *Australian Meteorological Magazine*, 41:7–19.

Adames, A. F. and Wallace, J. M. (2014). Three-dimensional structure and evolution of the MJO and its relation to the mean flow. *Journal of the Atmospheric Sciences*, 71:2007 – 2026.

Ahn, M.-S., Kim, D., Kang, D., Lee, J., Sperber, K. R., Gleckler, P. J., Jiang, X., Ham, Y.-G., and Kim, H. (2020). MJO propagation across the Maritime Continent: are CMIP6 models better than CMIP5 models? *Geophysical Research Letters*, 47(11):e2020GL087250.

Amante, C. and Eakins, B. W. (2009). ETOPO1 1 arc-minute global relief model: procedures, data sources and analysis. Technical Report NGDC-24, National Geophsical Data Center, Boulder, CO, USA.

Anderson, S. P., Weller, R. A., and Lukas, R. B. (1996). Surface buoyancy forcing and the mixed layer of the western pacific warm pool: Observations and 1D model results. *Journal of Climate*, 9(12):3056 – 3085.

Atlas, R., Hoffman, R. N., Ardizzone, J., Leidner, S. M., Jusem, J. C., Smith, D. K., and Gombos, D. (2011). A cross-calibrated, multiplatform ocean surface wind velocity product for meteorological and oceanographic applications. *Bulletin of the American Meteorological Society*, 92:157–174.

Barnes, H. C., Zuluaga, M. D., and Houze Jr., R. A. (2015). Latent heating characteristics of the MJO computed from TRMM observations. *Journal of Geophysical Research: Atmospheres*, 120(4):1322–1334.

Barton, N., Metzger, J. E., Reynolds, C. A., Ruston, B., Rowley, C., Smedstad, O. M., Ridout, J. A., Wallcraft, A., Frolov, S., Hogan, P., Janiga, M. A., Shriver, J. F., McLay, J., Thoppil, P., Huang, A., Crawford, W., Whitcomb, T., Bishop, C. H., Zamudio, L., and Phelps, M. (2021). The navy's earth system prediction capability: A new global coupled atmosphere-ocean-sea ice prediction system designed for daily to subseasonal forecasting. *Earth and Space Science*, 8(4):e2020EA001199.

Beljaars, A. C. M. (1995). The parametrization of surface fluxes in large-scale models under free convection. *Quarterly Journal of the Royal Meteorological Society*, 121(522):255–270.

Benedict, J. J. and Randall, D. A. (2009). Structure of the Madden–Julian oscillation in the superparameterized CAM. *Journal of the Atmospheric Sciences*, 66(11):3277 – 3296.

Benedict, J. J. and Randall, D. A. (2011). Impacts of idealized air–sea coupling on Madden–Julian oscillation structure in the superparameterized CAM. *Journal of the Atmospheric Sciences*, 68(9):1990 – 2008.

Biasutti, M., Yuter, S. E., Burleyson, C. D., and Sobel, A. H. (2012). Very high resolution rainfall patterns measured by TRMM precipitation radar: Seasonal and diurnal cycles. *Climate Dynamics*, 39:239–258.

Birch, C. E., Webster, S., Peatman, S. C., Parker, D. J., Matthews, A. J., Li, Y., and Hassim, M. E. E. (2016). Scale interactions between the MJO and the Western Maritime Continent. *Journal of Climate*, 29(7):2471 – 2492.

Boyle, J. S., Klein, S. A., Lucas, D. D., Ma, H.-Y., Tannahill, J., and Xie, S. (2015). The parametric sensitivity of CAM5's MJO. *Journal of Geophysical Research: Atmospheres*, 120(4):1424–1444.

Burleyson, C. D., Hagos, S. M., Feng, Z., Kerns, B. W. J., and Kim, D. (2018). Large-scale environmental characteristics of MJOs that strengthen and weaken over the Maritime Continent. *Journal of Climate*, 31(14):5731–5748.

Cai, Q., Zhang, G. J., and Zhou, T. (2013). Impacts of shallow convection on MJO simulation: A moist static energy and moisture budget analysis. *Journal of Climate*, 26(8):2417 – 2431.

Chang, M.-Y., Li, T., Lin, P.-L., and Chang, T.-H. (2019). Forecasts of MJO events during DYNAMO with a coupled atmosphere-ocean model: Sensitivity to cumulus parameterization scheme. *Journal of Meteorological Research*, 33:1016 – 1030.

Chen, G., Ling, J., Zhang, R., Xiao, Z., and Li, C. (2022). The MJO from CMIP5 to CMIP6: Perspectives from tracking MJO precipitation. *Geophysical Research Letters*, 49(1):e2021GL095241.

Chen, S. S. and Curcic, M. (2016). Ocean surface waves in Hurricane Ike (2008) and Superstorm Sandy (2012): Coupled model predictions and observations. *Ocean Modelling*, 103:161–176.

Chen, S. S., Houze, R. A., and Mapes, B. E. (1996). Multiscale variability of deep convection in relation to large-scale circulation in TOGA COARE. *Journal of Atmospheric Sciences*, 53(10):1380 – 1409.

Chen, S. S. and Jr, R. A. H. (1997). Diurnal variation and life-cycle of deep convective systems over the tropical pacific warm pool. *Quarterly Journal of the Royal Meteorological Society*, 123(538):357–388.

Chen, S. S., Kerns, B. W., Guy, N., Jorgensen, D. P., Delanoë, J., Viltard, N., Zappa, C. J., Judt, F., Lee, C.-Y., and Savarin, A. (2016). Aircraft observations of dry air, the ITCZ, convective cloud systems, and cold pools in MJO during DYNAMO. *Bulletin of the American Meteorological Society*, 97(3):405 – 423.

Chen, S. S., Zhao, W., Donelan, M. A., and Tolman, H. L. (2013). Directional wind-wave coupling in fully coupled atmosphere-wave-ocean models: Results from CBLAST-Hurricane. *Journal of the Atmospheric Sciences*, 70(10):3198 – 3215.

Chin, T. M., Vazquez-Cuervo, J., and Armstrong, E. M. (2017). A multi-scale high-resolution analysis of global sea surface temperature. *Remote Sensing of Environment*, 200:154–169.

Ciesielski, P. E., Yu, H., Johnson, R. H., Yoneyama, K., Katsumata, M., Long, C. N., Wang, J., Loehrer, S. M., Young, K., Williams, S. F., Brown, W., Braun, J., and Hove, T. V. (2014). Quality-controlled upper-air sounding dataset for DYNAMO/CINDY/AMIE: Development and corrections. *Journal of Atmospheric and Oceanic Technology*, 31(4):741 – 764.

Cummings, J. A. (2005). Operational multivariate ocean data assimilation. *Quarterly Journal of the Royal Meteorological Society*, 131:3583–3604.

Cummings, J. A. and Smedstad, O. M. (2013). Variational data assimilation for the global ocean. In Park, S. K. and Xu, L., editors, *Data Assimilation for Atmospheric, Oceanic and Hydrologic Applications (Vol II)*, volume 2, chapter 13. Springer.

de Szoeke, S. P., Edson, J. B., Marion, J. R., Fairall, C. W., and Bariteau, L. (2015). The MJO and air–sea interaction in TOGA COARE and DYNAMO. *Journal of Climate*, 28(2):597 – 622.

DeMott, C. A., Klingaman, N. P., and Woolnough, S. (2015). Atmosphere-ocean coupled processes in the Madden-Julian oscillation. *Reviews of Geophysics*, 53(4):1099–1154.

DeMott, C. A., Stan, C., Randall, D. A., and Branson, M. D. (2014). Intraseasonal variability in coupled GCMs: The roles of ocean feedbacks and model physics. *Journal of Climate*, 27(13):4970 – 4995.

DeMott, C. A., Wolding, B. O., Maloney, E. D., and Randall, D. A. (2018). Atmospheric mechanisms for MJO decay over the Maritime Continent. *Journal of Geophysical Research: Atmospheres*, 123(10):5188–5204.

Drushka, K., Sprintall, J., and Gille, S. T. (2014). Subseasonal variations in salinity and barrier-layer thickness in the eastern equatorial Indian Ocean. *Journal of Geophysical Research: Oceans*, 119(2):805–823.

Drushka, K., Sprintall, J., Gille, S. T., and Wijffels, S. (2012). In situ observations of Madden–Julian oscillation mixed layer dynamics in the Indian and Western Pacific oceans. *Journal of Climate*, 25(7):2306 – 2328.

Fairall, C., Bradley, E. F., Hare, J. E., Grachev, A. A., and Edson, J. B. (2003). Bulk parameterization of air-sea fluxes: Updates and verification for the COARE algorithm. *Journal of Climate*, 16(4):571 – 591.

Feng, J., Li, T., and Zhu, W. (2015). Propagating and nonpropagating MJO events over Maritime Continent. *Journal of Climate*, 28(21):8430 – 8449.

Feng, M., Hacker, P., and Lukas, R. (1998). Upper ocean heat and salt balances in response to a westerly wind burst in the western equatorial pacific during TOGA COARE. *Journal of Geophysical Research: Oceans*, 103(C5):10289–10311.

Fu, X., Wang, W., Lee, J.-Y., Wang, B., Kikuchi, K., Xu, J., Li, J., and Weaver, S. (2015). Distinctive roles of air–sea coupling on different MJO events: A new perspective revealed from the DYNAMO/CINDY field campaign. *Monthly Weather Review*, 143(3):794 – 812.

Gao, Y., Hsu, P.-C., and Hsu, H.-H. (2016). Assessments of surface latent heat flux associated with the Madden-Julian oscillation in reanalyses. *Climate Dynamics*, 47:1755 – 1774.

Hagos, S. M., Zhang, C., Feng, Z., Burleyson, C. D., DeMott, C., Kerns, B., Benedict, J. J., and Martini, M. N. (2016). The impact of the diurnal cycle on the propagation of Madden-Julian oscillation convection across the Maritime Continent. *Journal of Advances in Modeling Earth Systems*, 8(4):1552–1564.

Halkides, D. J., Waliser, D. E., Lee, T., Menemenlis, D., and Guan, B. (2015). Quantifying the processes controlling intraseasonal mixed-layer temperature variability in the tropical Indian Ocean. *Journal of Geophysical Research: Oceans*, 120(2):692–715.

Hannah, W. M. and Maloney, E. D. (2011). The role of moisture–convection feedbacks in simulating the Madden–Julian oscillation. *Journal of Climate*, 24(11):2754 – 2770.

Hayden, L. and Liu, C. (2021). Differences in the diurnal variation of precipitation estimated by spaceborne radar, passive microwave radiometer, and IMERG. *Journal of Geophysical Research: Atmospheres*, 126(9).

Hendon, H. H. and Liebmann, B. (1994). Organization of convection within the Madden-Julian oscillation. *Journal of Geophysical Research: Atmospheres*, 99(D4):8073–8083.

Hendon, H. H. and Salby, M. L. (1994). The life cycle of the madden-julian oscillation. *Journal of the Atmospheric Sciences*, 51(15):2225 – 2237.

Hirons, L. C., Inness, P., Vitart, F., and Bechtold, P. (2013). Understanding advances in the simulation of intraseasonal variability in the ECMWF model. part i: The representation of the MJO. *Quarterly Journal of the Royal Meteorological Society*, 139(675):1417–1426.

Holloway, C. E., Woolnough, S. J., and Lister, G. M. S. (2012). Precipitation distributions for explicit versus parametrized convection in a large-domain high-resolution tropical case study. *Quarterly Journal of the Royal Meteorological Society*, 138(668):1692–1708.

Holloway, C. E., Woolnough, S. J., and Lister, G. M. S. (2013). The effects of explicit versus parameterized convection on the MJO in a large-domain high-resolution tropical case study. part i: Characterization of large-scale organization and propagation. *Journal of the Atmospheric Sciences*, 70(5):1342 – 1369.

Holloway, C. E., Woolnough, S. J., and Lister, G. M. S. (2015). The effects of explicit versus parameterized convection on the MJO in a large-domain high-resolution tropical

case study. part ii: Processes leading to differences in MJO development. *Journal of the Atmospheric Sciences*, 72(7):2719 – 2743.

Hong, S.-Y., Dudhia, J., and Chen, S.-H. (2004). A revised approach to ice microphysical processes for the bulk parameterization of clouds and precipitation. *Monthly Weather Review*, 132(1):103 – 120.

Hong, S.-Y., Noh, Y., and Dudhia, J. (2006). A new vertical diffusion package with an explicit treatment of entrainment processes. *Monthly Weather Review*, 134(9):2318 – 2341.

Huffman, G. J., Bolvin, D. T., Braithwaite, D., Hsu, K., Joyce, R., Kidd, C., Nelkin, E. J., Sooroshian, S., Tan, J., and Xie, P. (2019). NASA global precipitation measurement (GPM) integrated multi-satellite retrievals for GPM (IMERG). Technical Report ATBD v06, National Aeronautics and Space Administration, Greenbelt, MD, USA.

Huffman, G. J., Bolvin, D. T., Nelkin, E. J., Wolff, D. B., Adler, R. F., Gu, G., Hong, Y., Bowman, K. P., and Stocker, E. F. (2007). The TRMM multisatellite precipitation analysis (tmpa): Quasi-global, multi-year, combined-sensor precipitation estimates at fine scales. *JOURNAL of Hydrometeorology*, 8(1):38 – 55.

Hung, M.-P., Lin, J.-L., Wang, W., Kim, D., Shinoda, T., and Weaver, S. J. (2013). MJO and convectively coupled equatorial waves simulated by CMIP5 climate models. *Journal of Climate*, 26(17):6185 – 6214.

Inness, P. M. and Slingo, J. M. (2006). The interaction of the Madden–Julian Oscillation with the Maritime Continent in a GCM. *Quarterly Journal of the Royal Meteorological Society*, 132(618):1645–1667.

Jensen, T. G., Shinoda, T., Chen, S., and Flatau, M. (2015). Ocean response to CINDY/DYNAMO MJOs in air-sea coupled COAMPS. *JOURNAL of the Meteorological Society of Japan*, 93A:157 – 178.

Jia, X., Li, C., Ling, J., and Zhang, C. (2008). Impacts of a GCM's resolution on MJO simulation. *Advances in Atmospheric Sciences*, pages 139 – 156.

Jia, X., Li, C., Zhou, N., and Ling, J. (2010). The MJO in an AGCM with three different cumulus parameterization schemes. *Dynamics of Atmospheres and Oceans*, 49(2):141–163.

Jiménez, P. A., Dudhia, J., González-Rouco, J. F., Navarro, J., Montávez, J. P., and García-Bustamante, E. (2012). A revised scheme for the WRF surface layer formulation. *Monthly Weather Review*, 140(3):898 – 918.

Johnson, R. H. and Ciesielski, P. E. (2017). Multiscale variability of the atmospheric boundary layer during DYNAMO. *Journal of the Atmospheric Sciences*, 74(12):4003 – 4021.

Kain, J. S. (2004). The Kain–Fritsch convective parameterization: An update. *JOURNAL of Applied Meteorology*, 43(1):170 – 181.

Kain, J. S. and Fritsch, J. M. (1990). A one-dimensional entraining/detraining plume model and its application in convective parameterization. *Journal of Atmospheric Sciences*, 47(23):2784 – 2802.

Kerns, B. W. and Chen, S. S. (2014). ECMWF and GFS model forecast verification during DYNAMO: Multiscale variability in MJO initiation over the equatorial Indian Ocean. *Journal of Geophysical Research: Atmospheres*, 119(7):3736–3755.

Kerns, B. W. and Chen, S. S. (2016). Large-scale precipitation tracking and the MJO over the Maritime Continent and Indo-Pacific warm pool. *Journal of Geophysical Research: Atmospheres*, 121:8755–8776.

Kerns, B. W. and Chen, S. S. (2018). Evaluation of satellite surface winds in relation to weather regimes over the Indian Ocean using DYNAMO observations. *Journal of Geophysical Research: Atmospheres*, 123(16):8561–8580.

Kerns, B. W. and Chen, S. S. (2020). A 20-year climatology of Madden-Julian oscillation convection: Large-scale precipitation tracking from TRMM-GPM rainfall. *Journal of Geophysical Research: Atmospheres*, 124.

Kikuchi, K. and Wang, B. (2008). Diurnal precipitation regimes in the global tropics. *Journal of Climate*, 21(11):2680–2696.

Klingaman., N. P. and Woolnough, S. J. (2014). Using a case-study approach to improve the Madden–Julian oscillation in the Hadley Centre model. *Quarterly Journal of the Royal Meteorological Society*, 140(685):2491–2505.

Klotzbach, P., Abhik, S., Hendon, H. H., Bell, M., Lucas, C., Marshall, A. G., and Oliver, E. C. J. (2019). On the emerging relationship between the stratospheric Quasi-Biennial Oscillation and the Madden-Julian oscillation. *Scientific Reports*, 9(2981).

Lau, K.-M. and Sui, C.-H. (1997). Mechanisms of short-term sea surface temperature regulation: Observations during TOGA COARE. *Journal of Climate*, 10(3):465 – 472.

Le, P. V. V., Guilloteau, C., Mamalakis, A., and Foufoula-Georgiou, E. (2021). Underestimated MJO variability in CMIP6 models. *Geophysical Research Letters*, 48(12):e2020GL092244.

Lee, Y.-C. and Wang, Y.-C. (2021). Evaluating diurnal rainfall signal performance from CMIP5 to CMIP6. *Journal of Climate*, 34(18):7607 – 7623.

Li, K., Yu, W., Yang, Y., Feng, L., Liu, S., and Li, L. (2020). Spring barrier to the MJO eastward propagation. *Geophysical Research Letters*, 46:e2020GL087788.

Li, Y., Jourdain, N. C., Taschetto, A. S., Gupta, A. S., Argüeso, D., Masson, S., and Cai, W. (2017). Resolution dependence of the simulated precipitation and diurnal cycle over the Maritime Continent. *Climate Dynamics*, 48:4009–4028.

Li, Y., Wu, J., Luo, J.-J., and Yang, Y. M. (2022). Evaluating the eastward propagation of the MJO in CMIP5 and CMIP6 models based on a variety of diagnostics. *Journal of Climate*, 35(6):1719 – 1743.

Lin, J.-L., Kiladis, G. N., Mapes, B. E., Weickmann, K. M., Sperber, K. R., Lin, W., Wheeler, M. C., Schubert, S. D., Genio, A. D., Donner, L. J., Emori, S., Gueremy, J.-F., Hourdin, F., Rasch, P. J., Roeckner, E., and Scinocca, J. F. (2006). Tropical intraseasonal variability in 14 IPCC AR4 climate models. part i: Convective signals. *Journal of Climate*, 19(12):2665 – 2690.

Ling, J., Bauer, P., Bechtold, P., Beljaars, A., Forbes, R., Vitart, F., Ulate, M., and Zhang, C. (2014). Global versus local MJO forecast skill of the ECMWF model during DYNAMO. *Monthly Weather Review*, 142(6):2228 – 2247.

Ling, J., Zhang, C., Joyce, R., Xie, P.-P., and Chen, G. (2019a). Possible role of the diurnal cycle in land convection in the barrier effect on the MJO by the Maritime Continent. *Geophysical Research Letters*, 46(5):3001–3011.

Ling, J., Zhao, Y., and Chen, G. (2019b). Barrier effect on MJO propagation by the Maritime Continent in the MJO Task Force/GEWEX atmospheric system study models. *Journal of Climate*, 32(17):5529 – 5547.

Liu, Y., Tan, Z.-M., and Wu, Z. (2022). Enhanced feedback between shallow convection and low-level moisture convergence leads to improved simulation of MJO eastward propagation. *Journal of Climate*, 35(2):591 – 615.

Love, B. S., Matthews, A. J., and Lister, G. M. S. (2011). The diurnal cycle of precipitation over the Maritime Continent in a high-resolution atmospheric model. *Quarterly Journal of the Royal Meteorological Society*, 137(657):934–947.

Lu, J., Li, T., and Wang, L. (2019). Precipitation diurnal cycle over the Maritime Continent modulated by the MJO. *Climate Dynamics*, 53.

Lu, W. and Hsu, P.-C. (2017). Factors controlling the seasonality of the madden-julian oscillation. *Dynamics of Atmospheres and Oceans*, 78:106–120.

Lukas, R. and Lindstrom, E. (1991). The mixed layer of the western equatorial Pacific Ocean. *Journal of Geophysical Research: Oceans*, 96(S01):3343–3357.

Madden, R. A. and Julian, P. R. (1971). Detection of a 40–50 day oscillation in the zonal wind in the tropical Pacific. *Journal of Atmospheric Sciences*, 28(5):702 – 708.

Madden, R. A. and Julian, P. R. (1972). Description of global-scale circulation cells in the tropics with a 40–50 day period. *Journal of Atmospheric Sciences*, 29(6):1109 – 1123.

Mahrt, L. T. and Sun, J. (1995). The subgrid velocity scale in the bulk aerodynamic relationship for spatially averaged scalar fluxes. *Monthly Weather Review*, 123(10):3032 – 3041.

Mallard, M. S., Lackmann, G. M., Aiyyer, A., and Hill, K. (2013). Atlantic hurricanes and climate change. part i: Experimental design and isolation of thermodynamic effects. *Journal of Climate*, 26(13):4876 – 4893.

Maloney, E. D. and Hartmann, D. L. (1998). Frictional moisture convergence in a composite life cycle of the Madden–Julian oscillation. *Journal of Climate*, 11(9):2387 – 2403.

Maloney, E. D. and Hartmann, D. L. (2000a). Modulation of eastern North Pacific hurricanes by the Madden–Julian oscillation. *Journal of Climate*, 13(9):1451–1460.

Maloney, E. D. and Hartmann, D. L. (2000b). Modulation of hurricane activity in the Gulf of Mexico by the Madden-Julian oscillation. *Science*, 287(5460):2002–2004.

Maloney, E. D. and Kiehl, J. T. (2002). MJO-related SST variations over the tropical Eastern Pacific during Northern Hemisphere summer. *Journal of Climate*, 15(6):675 – 689.

Maloney, E. D. and Sobel, A. H. (2004). Surface fluxes and ocean coupling in the tropical intraseasonal oscillation. *Journal of Climate*, 17(22):4368 – 4386.

Marshall, A. G., Alves, O., and Hendon, H. H. (2008). An enhanced moisture convergence–evaporation feedback mechanism for MJO air–sea interaction. *Journal of the Atmospheric Sciences*, 65(3):970 – 986.

Martin, Z., Son, S.-W., Butler, A., Hendon, H., Kim, H., Sobel, A., Yoden, S., and Zhang, C. (2021). The influence of the quasi-biennial oscillation on the Madden-Julian oscillation. *Nature Reviews Earth & Environment*.

Matthews, A. J., Hoskins, B. J., and Masutani, M. (2004). The global response to tropical heating in the Madden–Julian oscillation during the northern winter. *Quarterly Journal of the Royal Meteorological Society*, 130(601):1991–2011.

Mazza, E. and Chen, S. S. (2022). Tropical cyclone rainfall climatology, extremes and flooding potential over the continental US. *Submitted to the Journal of Hydrometeorology*.

McPhaden, M. J. and Foltz, G. R. (2013). Intraseasonal variations in the surface layer heat balance of the central equatorial Indian Ocean: The importance of zonal advection and vertical mixing. *Geophysical Research Letters*, 40(11):2737–2741.

McPhaden, M. J., Meyers, G., Ando, K., Masumoto, Y., Murty, V. S. N., Ravichandran, M., Syamsudin, F., Vialard, J., Yu, L., and Yu, W. (2009). RAMA: The research moored array for African–Asian–Australian monsoon analysis and prediction. *Bulletin of the American Meteorological Society*, 90(4):459 – 480.

McPhaden, M. J., Zhang, X., Hendon, H. H., and Wheeler, M. C. (2006). Large scale dynamics and MJO forcing of ENSO variability. *Geophysical Research Letters*, 33(16).

Mechem, D. B., Chen, S. S., and Jr., R. A. H. (2006). Momentum transport processes in the stratiform regions of mesoscale convective systems over the western Pacific warm pool. *Quarterly Journal of the Royal Meteorological Society*, 132(616):709–736.

Mechem, D. B., Houze Jr, R. A., and Chen, S. S. (2002). Layer inflow into precipitating convection over the western tropical pacific. *Quarterly Journal of the Royal Meteorological Society*, 128(584):1997–2030.

Metzger, E. J., Smedstad, O. M., Thoppil, P. G., Hurlburt, H. E., Cummings, J. A., Wallcraft, A. J., Zamudio, L., Franklin, D. S., Posey, P. G., Phelps, M. W., Hogan, P. J., Bub, F. L., and DeHaan, C. J. (2014). US navy operational global ocean and arctic ice prediction systems. *Oceanography*, 27(3):32–43.

Miller, S. T. K., Keim, B. D., Talbot, R. W., and Mao, H. (2003). Sea breeze: Structure, forecasting, and impacts. *Reviews of Geophysics*, 41(3).

Miura, H., Satoh, M., and Katsumata, M. (2009). Spontaneous onset of a Madden-Julian oscillation event in a cloud-system-resolving simulation. *Geophysical Research Letters*, 36(13).

Miura, H., Satoh, M., Nasuno, T., Noda, A. T., and Oouchi, K. (2007). A Madden-Julian oscillation event realistically simulated by a global cloud-resolving model. *Science*, 318(5857):1763 – 1765.

Miyakawa, T., Satoh, M., Miura, H., Tomita, H., Yashiro, H., Noda, A. T., Yamada, Y., Kodama, C., Kimoto, M., and Yoneyama, K. (2014). Madden-Julian Oscillation prediction skill of a new-generation global model demonstrated using a supercomputer. *Nature Communications*, 5(3769).

Moron, V., Robertson, A. W., Qian, J.-H., and Ghil, M. (2015). Weather types across the Maritime Continent: from the diurnal cycle to interannual variations. *Frontiers in Environmental Science*, 2.

Moum, J. N., de Szoeke, S. P., Smyth, W. D., Edson, J. B., DeWitt, H. L., Moulin, A. J., Thompson, E. J., Zappa, C. J., Rutledge, S. A., Johnson, R. H., and Fairall, C. W.

(2014). Air–sea interactions from westerly wind bursts during the november 2011 MJO in the Indian Ocean. *Bulletin of the American Meteorological Society*, 95(8):1185 – 1199.

Moum, J. N., Pujiana, K., Lien, R.-C., and Smyth, W. D. (2016). Ocean feedback to pulses of the Madden-Julian oscillation in the equatorial Indian Ocean. *Nature Communications*, 7(13203).

Nakazawa, T. (1988). Tropical super clusters within intraseasonal variations over the Western Pacific. *Journal of the Meteorological Society of Japan. Ser. II*, 66(6):823–839.

Nasuno, T. (2013). Forecast skill of Madden-Julian oscillation events in a global nonhydrostatic model during the CINDY2011/DYNAMO observation period. *SOLA*, 9:69 – 73.

Neale, R. and Slingo, J. (2003). The Maritime Continent and its role in global climate: A GCM study. *Journal of Climate*, 16(5):834–848.

Nesbitt, S. W. and Zipser, E. J. (2003). The diurnal cycle of rainfall and convective intensity according to three years of TRMM measurements. *Journal of Climate*, 16(10):1456 – 1475.

NOAA National Geophysical Data Center (2009). ETOPO1 1 arc-minute global relief model.

Oh, J.-H., Kim, K.-Y., and Lim, G.-H. (2012). Impact of MJO on the diurnal cycle of rainfall over the western Maritime Continent in the austral summer. *Climate Dynamics*, 38(5):1167–1180.

Peatman, S. C., Matthews, A. J., and Stevens, D. P. (2014). Propagation of the Madden–Julian Oscillation through the Maritime Continent and scale interaction with the diurnal cycle of precipitation. *Quarterly Journal of the Royal Meteorological Society*, 140(680):814–825.

Pilon, R., Zhang, C., and Dudhia, J. (2016). Roles of deep and shallow convection and

microphysics in the MJO simulated by the model for prediction across scales. *Journal of Geophysical Research: Atmospheres*, 121(18):10,575–10,600.

Rauniyar, S. P. and Walsh, K. J. E. (2011). Scale interaction of the diurnal cycle of rainfall over the Maritime Continent and Australia: Influence of the MJO. *Journal of Climate*, 24(2):325 – 348.

Robert A. Houze, J., Chen, S. S., Kingsmill, D. E., Serra, Y., and Yuter, S. E. (2000). Convection over the pacific warm pool in relation to the atmospheric kelvin-rossby wave. *Journal of the Atmospheric Sciences*, 57(18):3058 – 3089.

Sakaeda, N., Kiladis, G., and Dias, J. (2017). The diurnal cycle of tropical cloudiness and rainfall associated with the Madden–Julian Oscillation. *Journal of Climate*.

Savarin, A. and Chen, S. S. (2022a). Pathways to better prediction of the MJO: 1. effects of model resolution and moist physics on atmospheric boundary layer and precipitation. *JOURNAL of Advances in Modeling Earth Systems*, 14(6):e2021MS002928.

Savarin, A. and Chen, S. S. (2022b). Pathways to better prediction of the MJO: 2. impacts of atmosphere-ocean coupling on the upper ocean and mjo propagation. *JOURNAL of Advances in Modeling Earth Systems*, 14(6):e2021MS002929.

Schiemann, R., Demory, M.-E., Mizielinski, M. S., Roberts, J. M., Shaffrey, L. C., Strachan, J., and Vidale, P. L. (2014). The sensitivity of the tropical circulation and Maritime Continent precipitation to climate model resolution. *Climate Dynamics*, 42:2455–2468.

Seiki, A. and Takayabu, Y. N. (2007). Westerly wind bursts and their relationship with intraseasonal variations and ENSO. part i: Statistics. *Monthly Weather Review*, 135(10):3325 – 3345.

Shinoda, T. and Hendon, H. H. (1998). Mixed layer modeling of intraseasonal variability in the tropical Western Pacific and Indian Oceans. *Journal of Climate*, 11(10):2668 – 2685.

Shinoda, T., Jensen, T. G., Flatau, M., and Chen, S. (2013). Surface wind and upper-ocean variability associated with the Madden-Julian oscillation simulated by the coupled ocean-atmosphere mesoscale prediction system (COAMPS). *Monthly Weather Review*, 141(7):1190–2307.

Shinoda, T., Pei, S., Wang, W., Fu, J. X., Lien, R.-C., Seo, H., and Soloviev, A. (2021). Climate process team: Improvement of ocean component of NOAA climate forecast system relevant to Madden-Julian oscillation simulations. *JOURNAL of Advances in Modeling Earth Systems*, 13(12):e2021MS002658.

Skamarock, W. C., Klemp, J. B., Dudhia, J., Gill, D. O., Barker, D. M., Duda, M., Huang, X.-Y., Wang, W., and Powers, J. G. (2008). A description of the advanced research WRF version 3. Technical Report NCAR/TN-475+STR, University Corporation for Atmospheric Research.

Slingo, J. M., Sperber, K. R., Ceron, J.-P., Dix, M., Dugas, B., Ebisuzaki, W., Fyfe, J., Gregory, D., Gueremy, J.-F., Hack, J., Harzallah, A., Inness, P., Kitoh, A., Lau, W. K.-M., McAvaney, B., Madden, R., Matthews, A., Palmer, T. N., Parkas, C.-K., Randall, D., and Renno, N. (1996). Intraseasonal oscillations in 15 atmospheric general circulation models: results from an AMIP diagnostic subproject. *Climate Dynamics*, 12:325 – 357.

Sobel, A. H., Maloney, E. D., Bellon, G., , and Frierson, D. M. (2010). Surface fluxes and tropical intraseasonal variability: a reassessment. *Journal of Advances in Modeling Earth Systems*, 2(1).

Song, F. and Zhang, G. J. (2018). Understanding and improving the scale dependence of trigger functions for convective parameterization using cloud-resolving model data. *Journal of Climate*, 31(18):7385 – 7399.

Sprintall, J. and Tomczak, M. (1992). Evidence of the barrier layer in the surface layer of the tropics. *Journal of Geophysical Research: Oceans*, 97(C5):7305–7316.

Stan, C., Khairoutdinov, M., DeMott, C. A., Krishnamurthy, V., Straus, D. M., Randall, D. A., III, J. L. K., and Shukla, J. (2010). An ocean-atmosphere climate simulation with an embedded cloud resolving model. *Geophysical Research Letters*, 37(1).

Stull, R. B. (1988). *An Introduction to Boundary Layer Meteorology*. Kluwer Academic Publishers.

Suhas, E. and Zhang, G. J. (2014). Evaluation of trigger functions for convective parameterization schemes using observations. *Journal of Climate*, 27(20):7647 – 7666.

Takayabu, Y. N. (1994). Large-scale cloud disturbances associated with equatorial waves. part 1: Spectral features of the cloud disturbances. *JOURNAL of the Meteorological Society of Japan. Ser. II*, 72(3):433–449.

Tam, C.-Y. and Lau, N.-C. (2005). Modulation of the Madden-Julian oscillation by ENSO: Inferences from observations and GCM simulations. *Journal of the Meteorological Society of Japan*, 83(5):727–743.

Tan, H., Ray, P., Barrett, B., Dudhia, J., Moncrieff, M., Zhang, L., and Zermeno-Diaz, D. (2022). Understanding the role of topography on the diurnal cycle of precipitation in the Maritime Continent during MJO propagation. *Climate Dynamics*, 58(11):3003–3019.

Tan, J., Huffman, G. J., Bolvin, D. T., and Nelkin, E. J. (2019). Diurnal cycle of IMERG V06 precipitation. *Geophysical Research Letters*, 46(22):13584–13592.

Taraphdar, S., Zhang, F., Leung, L. R., Chen, X., and Pauluis, O. M. (2018). MJO affects the monsoon onset timing over the Indian region. *Geophysical Research Letters*, 45(18):10011–10018.

Tian, B., Waliser, D. E., and Fetzer, E. J. (2006). Modulation of the diurnal cycle of tropical deep convective clouds by the MJO. *Geophysical Research Letters*, 33(20).

Tian, F., Hou, S., Yang, L., Hu, H., and Hou, A. (2018). How does the evaluation of the GPM IMERG rainfall product depend on gauge density and rainfall intensity? *Journal of Hydrometeorology*, 19(2):339 – 349.

Tiedtke, M. (1989). A comprehensive mass flux scheme for cumulus parameterization in large-scale models. *Monthly Weather Review*, 117(8):1779 – 1800.

Torn, R. D. and Davis, C. A. (2012). The influence of shallow convection on tropical cyclone track forecasts. *Monthly Weather Review*, 140(7):2188 – 2197.

Vecchi, G. A. and Bond, N. A. (2004). The Madden-Julian oscillation (MJO) and northern high latitude wintertime surface air temperatures. *Geophysical Research Letters*, 31(4).

Virts, K. S., Wallace, J. M., Hutchins, M. L., and Holzworth, R. H. (2013). Diurnal lightning variability over the Maritime Continent: Impact of low-level winds, cloudiness, and the MJO. *Journal of the Atmospheric Sciences*, 70(10):3128 – 3146.

Waliser, D. E., Lau, K. M., and Kim, J.-H. (1999). The influence of coupled sea surface temperatures on the Madden–Julian oscillation: A model perturbation experiment. *Journal of the Atmospheric Sciences*, 56(3):333 – 358.

Waliser, D. E., Lau, K. M., Stern, W., and Jones, C. (2003). Potential predictability of the Madden–Julian oscillation. *Bulletin of the American Meteorological Society*, 84(1):33 – 50.

Wang, S., Sobel, A. H., Lee, C.-Y., Ma, D., Chen, S. S., Curcic, M., and Pullen, J. (2021). Propagating mechanisms of the 2016 summer BSISO event: Air-sea coupling, vorticity, and moisture. *Journal of Geophysical Research: Atmospheres*, 126(2):e2020JD033284.

Wang, S., Sobel, A. H., Zhang, F., Sun, Y. Q., Yue, Y., and Zhou, L. (2015). Regional simulation of the October and November MJO events observed during the CINDY/DYNAMO field campaign at gray zone resolution. *Journal of Climate*, 28(6):2097 – 2119.

Watters, D., Battaglia, A., and Allan, R. P. (2021). The diurnal cycle of precipitation according to multiple decades of global satellite observations, three CMIP6 models, and the ECMWF reanalysis. *Journal of Climate*, 34(12):5063 – 5080.

Webster, P. J. and Lukas, R. (1992). TOGA COARE: The Coupled Ocean–Atmosphere Response Experiment. *Bulletin of the American Meteorological Society*, 73(9):1377 – 1416.

Wei, Y., Pu, Z., and Zhang, C. (2020). Diurnal cycle of precipitation over the Maritime Continent under modulation of MJO: Perspectives from cloud-permitting scale simulations. *Journal of Geophysical Research: Atmospheres*, 125(13).

Weller, R. A. and Anderson, S. P. (1996). Surface meteorology and air-sea fluxes in the Western Equatorial Pacific warm pool during the TOGA coupled ocean-atmosphere response experiment. *Journal of Climate*, 9(8):1959 – 1990.

Wheeler, M. and Kiladis, G. N. (1999). Convectively coupled equatorial waves: Analysis of clouds and temperature in the wavenumber–frequency domain. *Journal of the Atmospheric Sciences*, 56(3):374 – 399.

Wheeler, M. C. and Hendon, H. H. (2004). An all-season real-time multivariate MJO index: Development of an index for monitoring and prediction. *Monthly Weather Review*, 132(8):1917 – 1932.

Wilson, E. A., Gordon, A. L., and Kim, D. (2013). Observations of the Madden Julian oscillation during Indian Ocean Dipole events. *Journal of Geophysical Research: Atmospheres*, 118(6):2588–2599.

Wimmers, A. J. and Velden, C. S. (2011). Seamless advective blending of total precipitable water retrievals from polar-orbiting satellites. *JOURNAL of Applied Meteorology and Climatology*, 50(5):1024 – 1036.

Wu, C.-H. and Hsu, H.-H. (2009). Topographic influence on the MJO in the Maritime Continent. *Journal of Climate*, 22(20):5433–5448.

Yang, Y.-M. and Wang, B. (2019). Improving MJO simulation by enhancing the interaction between boundary layer convergence and lower tropospheric heating. *Climate Dynamics*, 52:4671 – 4693.

Yoneyama, K., Zhang, C., and Long, C. N. (2013). Tracking pulses of the Madden–Julian oscillation. *Bulletin of the American Meteorological Society*, 94(12):1871 – 1891.

Yu, L., Jin, X., and Weller, R. A. (2019). Multidecade global flux datasets from the objectively analyzed air-sea fluxes (OAFLUX) project: Latent and sensible heat fluxes, ocean evaporation, and related surface meteorological variables. Technical report, Woods Hole Oceanographic Institution.

Zhang, C. (2005). Madden-Julian oscillation. *Reviews of Geophysics*, 43(2).

Zhang, C. (2013). Madden–Julian oscillation: Bridging weather and climate. *Bulletin of the American Meteorological Society*, 94(12):1849 – 1870.

Zhang, C., Dong, M., Gualdi, S., Hendon, H. H., Maloney, E. D., Marshall, A., Sperber, K. R., and Wang, W. (2006). Simulations of the Madden-Julian oscillation in four pairs of coupled and uncoupled global models. *Climate Dynamics*, 27:573 – 592.

Zhang, C., f Adames, A., Khouider, B., wang, B., and Yang, D. (2020). Four theories of the madden-julian oscillation. *Reviews of Geophysics*, 58:e2019RG000685.

Zhang, C. and Ling, J. (2017). Barrier effect of the Indo-Pacific Maritime Continent on the MJO: Perspectives from tracking MJO precipitation. *Journal of Climate*, 30(9):3439 – 3459.

Zhang, C., Wang, Y., and Hamilton, K. (2011). Improved representation of boundary layer clouds over the southeast pacific in ARW-WRF using a modified Tiedtke cumulus parameterization scheme. *Monthly Weather Review*, 139(11):3489 – 3513.

Zhang, L. and Han, W. (2020). Barrier for the eastward propagation of Madden-Julian oscillation over the Maritime Continent: A possible new mechanism. *Geophysical Research Letters*, 47(21).

Zhao, C. and Li, T. (2018). Basin dependence of the MJO modulating tropical cyclone genesis. *Climate Dynamics*, 52:6081–6096.

Zheng, C. and Chang, E. K. M. (2019). The role of MJO propagation, lifetime, and intensity on modulating the temporal evolution of the MJO extratropical response. *Journal of Geophysical Research: Atmospheres*, 124(10):5352–5378.

Zhou, L., Neale, R. B., Jochum, M., and Murtugudde, R. (2012). Improved Madden–Julian oscillations with improved physics: The impact of modified convection parameterizations. *Journal of Climate*, 25(4):1116 – 1136.

Zhou, Y., Fang, J., and Wang, S. (2021a). Impact of islands on the MJO propagation across the Maritime Continent: a numerical modeling study of an MJO event. *Climate Dynamics*, 57(9).

Zhou, Y., Kim, H., and Waliser, D. E. (2021b). Atmospheric river lifecycle responses to the Madden-Julian oscillation. *Geophysical Research Letters*, 48(3):e2020GL090983.

Zhu, H., Hendon, H., and Jakob, C. (2009). Convection in a parameterized and superparameterized model and its role in the representation of the MJO. *Journal of the Atmospheric Sciences*, 66(9):2796 – 2811.

Zhu, J., Kumar, A., and Wang, W. (2020). Dependence of MJO predictability on convective parameterizations. *Journal of Climate*, 33(11):4739 – 4750.